

Large-eddy simulation of airborne wind energy farms

Thomas Haas¹, Jochem De Schutter², Moritz Diehl^{2,3}, and Johan Meyers¹

¹KU Leuven, Department of Mechanical Engineering, Celestijnenlaan 300, BE-3001 Leuven, Belgium

²University of Freiburg, Department of Microsystems Engineering, Georges-Köhler-Allee 102, DE-79110 Freiburg, Germany

³University of Freiburg, Department of Mathematics, Georges-Köhler-Allee 102, DE-79110 Freiburg, Germany

Correspondence: Thomas Haas (thomas.haas@kuleuven.be)

Abstract. The future utility-scale deployment of airborne wind energy technologies requires the development of large-scale multi-megawatt systems. This study aims at quantifying the interaction between the atmospheric boundary layer (ABL) and large-scale airborne wind energy systems operating in a farm. To that end, we present a virtual flight simulator combining large-eddy simulations to simulate turbulent flow conditions and optimal control techniques for flight-path generation and tracking. The two-way coupling between flow and system dynamics is achieved by implementing an actuator sector method that we pair to a model predictive controller. In this study, we consider ground-based power generation pumping-mode AWE systems (lift-mode AWES) and on-board power generation AWE systems (drag-mode AWES). The aircraft have wingspans of approximately 60 m and fly large loops of approximately 200 m-diameter centered at 200 m altitude. For the lift-mode AWES, we additionally investigate different reel-out strategies to reduce the interaction between the tethered wing and its own wake. Further, we investigate AWE parks consisting of 25 systems organized in 5 rows of 5 systems. For both lift- and drag-mode archetypes, we consider a moderate park layout with a power density of 10 MW km^{-2} achieved at a rated wind speed of 12 m s^{-1} . For the drag-mode AWES, an additional park with denser layout and power density of 28 MW km^{-2} is also considered. The model predictive controller achieves very satisfactory flight-path tracking despite the AWE systems operating in fully waked, turbulent flow conditions. Furthermore, we observe significant wake effects for the utility-scale AWE systems considered in the study. Wake-induced performance losses increase gradually through the downstream rows of systems and reach in the last row of the parks up to 17% for the lift-mode AWE park and up to 25% and 45% for the moderate and dense drag-mode AWE parks, respectively. For an operation period of 60 minutes at a below-rated reference wind speed of 10 m s^{-1} , the lift-mode AWE park generates about 84.4 MW of power, corresponding to 82.5 % of the power yield expected when AWE systems operate ideally and interaction with the ABL is negligible. For the drag-mode AWE parks, the moderate and dense layouts generate about 86.0 MW and 72.9 MW of power, respectively, corresponding to 89.2 % and 75.6 % of the ideal power yield.

1 Introduction

The contribution of airborne wind energy (AWE) technologies to utility-scale electricity generation calls for the deployment of large-scale AWE systems operating in parks. For conventional wind farms, downstream rows of wind turbines generate up to 40% less power than the front row of the farm (Barthelmie et al., 2010). This performance decrease is due to the

aggregated effect of upstream turbine wakes. Wind turbine wakes result from the interaction between wind turbines and the atmospheric boundary layer, and are characterized by a wind speed deficit and increased turbulence intensity (Stevens and Meneveau, 2017; Porte-Agel et al., 2020). For airborne wind energy systems, wake effects are generally considered small (Kruijff and Ruitkamp, 2018) or are often ignored (Echeverri et al., 2020) due to the large swept area and relatively small wing dimensions. Hence, recent studies investigating performance losses (Malz et al., 2018) or layout optimization (Roque et al., 2020) in airborne wind energy farms did not consider wake effects.

For individual systems, recent investigations of flow induction and wake effects were performed, mainly considering axisymmetric AWES configurations in uniform inflows using either analyses based on momentum theory (Leuthold et al., 2017; De Lellis et al., 2018), vortex theory (Leuthold et al., 2019; Gaunaa et al., 2020) or the entrainment hypothesis (Kaufman-Martin et al., 2021), or high-fidelity CFD simulations (Haas and Meyers, 2017; Kheiri et al., 2018). Further numerical investigations of large-scale airborne wind energy systems in the atmospheric boundary layer (ABL) (Haas et al., 2019b) have shown that the wake development downstream of the system is considerable, hence suggesting that wake effects of utility-scale airborne wind energy systems cannot be neglected when operating in parks.

To quantify the wake-induced performance losses in a park of airborne wind energy systems, we have developed a computational framework combining large-eddy simulations (LES) and optimal control techniques. This framework couples the dynamics of the atmospheric boundary layer with the dynamics of several airborne wind energy systems operating in a park. The last two decades have seen the establishment of large-eddy simulations as an emerging tool for the modelling of wind turbines and wind farms in the atmospheric boundary layer (Jimenez et al., 2007; Calaf et al., 2010), hence we apply this technique in the context of airborne wind energy parks. The inherent unsteadiness of the wind, the effects of wake flows and ABL turbulence make it challenging to foresee the behaviour and performance of individual AWE systems in the park. When modelling AWE systems, the wind environment is often approximated as a height-dependent power law or logarithmic distribution (Archer, 2013; Zanon et al., 2013b; Horn et al., 2013; Bauer et al., 2018). A limited number of studies have used more realistic virtual wind conditions from large-eddy simulations to assess the robustness of their control strategies (Sternberg et al., 2012; Rapp et al., 2019). However, none of the aforementioned studies have measured how the atmospheric boundary layer flow is altered by the operation of airborne wind energy systems.

Moreover in recent years, the airborne wind energy community has grown significantly and has seen the emergence of many developers of airborne wind energy systems. The designed systems may be as diverse in their operation mode as they are in the way they transform kinetic energy of the wind into usable mechanical work. A non-exhaustive list of AWE developers is presented in Cherubini et al. (2015). Arising from the seminal work of Loyd (1980), a majority of designs are based on the introduced lift- and drag-modes of operation, which rely on the high aerodynamic forces generated by the crosswind flight of a tethered aircraft. For the lift-mode technology, power is generated on-ground by a generator driven by the rotation of the tether winch, which is induced as the tether is reeled out. For the drag-mode technology, power is directly generated on-board by small turbines mounted onto the airframe. The working principles of both technologies are presented in detail by Diehl (2013). Although additional concepts such as kite networks (Read, 2018) and multi-kite systems (De Schutter et al., 2019) propose alternative upscaling strategies for the utility-scale generation, we focus in this study on single-aircraft AWE systems.

In particular, we consider large-scale multi-megawatt systems operating in both lift- and drag-modes and align our design with the proposed utility-scale system targets unveiled by the companies Ampyx Power (Kruijff and Ruitkamp, 2018) and Makani Power (Harham, 2012).

Hence, we address in this paper the operation of large-scale AWE systems in a virtual wind environment in order to investigate the interaction between AWE systems and the ABL and quantify the impact of individual system wakes on the overall AWE farm performance. The paper is organized as follows: The methodology section, Sect. 2, details the computational framework developed for this study. The section presents the generation and tracking of AWE system trajectories by means of optimal control techniques as well as the modelling of atmospheric flows and its coupling with the AWE system dynamics by means of large-eddy simulations. Section 3 highlights the specific features of the flight path of both the lift- and drag-mode AWE systems, provides the configuration of the simulation domain and settings of the actuator methods, and also presents the ABL flow conditions and AWE farm layout chosen for this study. Section 4 presents the principal outcomes of the AWE farm simulation, focussing on the tracking behaviour of the AWE systems, assessing the performance of AWE farms for both operation modes, and discussing the complex interaction between AWE systems and turbulent ABL in terms of main flow and turbulent quantities. Finally, Sect. 5 highlights the main insights gained in the present study and discusses future work.

2 Methodology

The interaction between AWE systems and the atmospheric boundary layer requires a reciprocal coupling of both the system and flow dynamics. We have therefore developed a computational framework combining large-eddy simulations and optimal control techniques. The framework consists of two distinct blocks: the virtual plant, simulating the operation of AWE systems in a turbulent wind field, and the controller, supervising the plant performance and guaranteeing its operation. Figure 1 presents an overview of the different building blocks of the framework. The virtual plant is the executing organ of the framework and consists of two interconnected modules handling the coupled simulation of the ABL flow (Sect. 2.1) and AWES dynamics (Sect. 2.2) within the LES framework. The controller block is the deciding organ of the framework and is built on two hierarchical modules, the supervision level, which defines the reference trajectories flown by each AWE system in the plant (Sect. 2.3), and the tracking level, which computes the steering actions of each individual AWE system (Sect. 2.4).

2.1 Virtual plant: wind flow dynamics

The procedure applied to simulate wind flow dynamics is shown in Fig. 1, part A. The dynamics of the ABL are computed by means of large-eddy simulation (LES) and the effects of AWE systems on the flow are modelled using actuator methods. The LES methodology is presented in Sect. 2.1.1 and the actuator methods are introduced in Sect. 2.1.2.

2.1.1 Atmospheric boundary layer simulation

In the last decades, LES has become a widely used tool to model conventional wind farms in the atmospheric boundary layer (Calaf et al., 2010; Munters et al., 2016; Allaerts and Meyers, 2017), such that we adopt the same approach to investigate

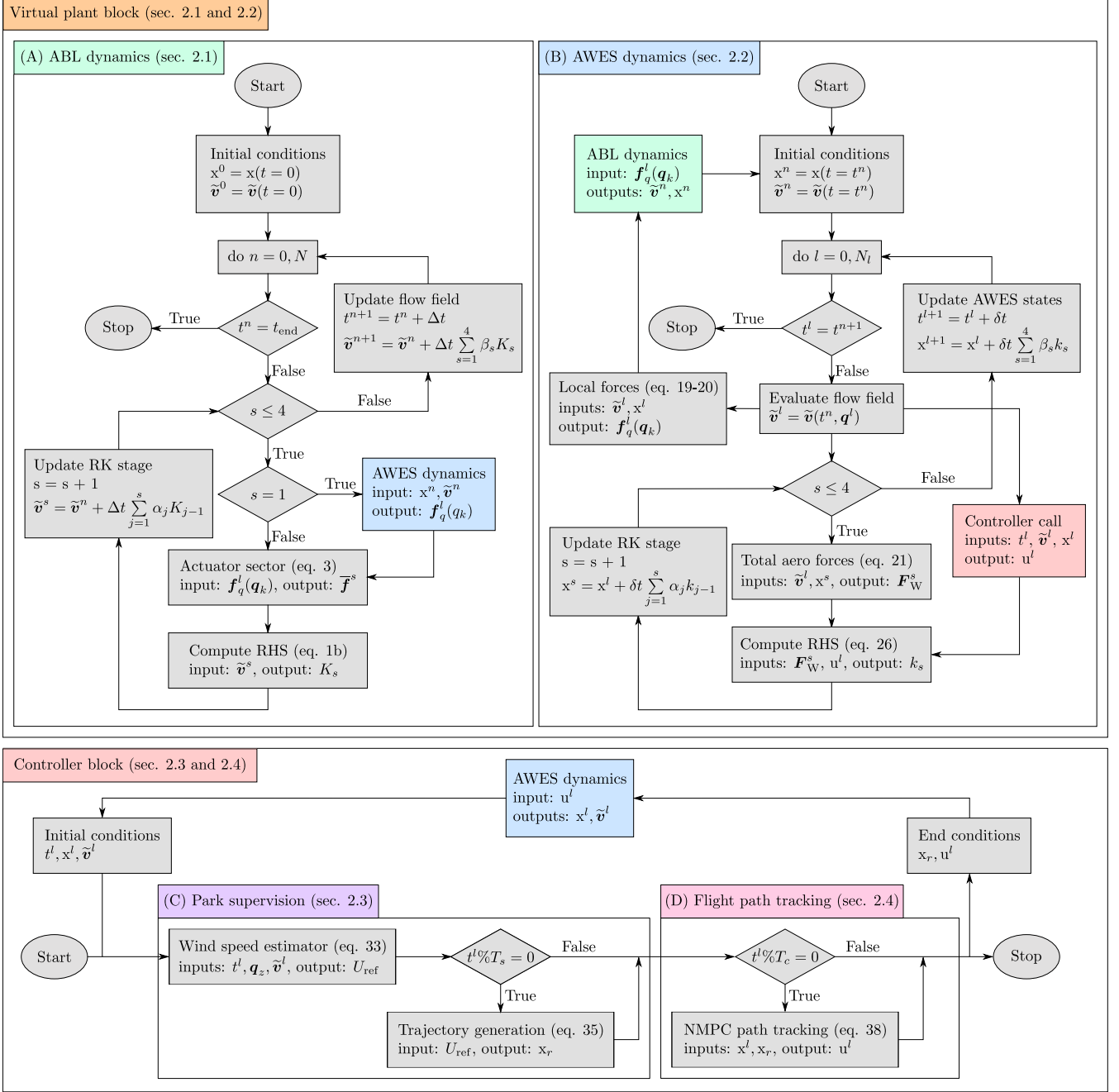


Figure 1. Diagram representing the combined LES-OCF framework used in this study for the simulation of AWE parks in the ABL. Each part of the diagram refers to a specific feature of the framework. The diagram indicates the connections between the individual features and refers to specific subsections and the associated equations for a complete overview and discussion in the methodology section, Sect. 2.

airborne wind energy parks. In LES methodology, large- and medium-scale flow structures are directly resolved with sufficient spatio-temporal resolution whereas the influence of smaller-scale, dissipative motion is modelled. The large, energy-containing structures, such as wind speed variations over regions spanning several hundreds of meters, play a predominant role in the energy extraction process of conventional and airborne wind energy systems alike. In LES computations, the transfer of energy across (a large part of) the inertial sub-range is further resolved, while the viscous dissipation of energy at the smallest scales is modelled using a subgrid-scale model.

In the current study, we neglect Coriolis and thermal effects, such that we only need to consider the turbulent surface layer of the ABL. In addition, the atmospheric flow through a wind farm is associated to a high Reynolds number such that we can omit the resolved effects of viscosity. Hence, the ABL can then be simplified to a pressure-driven boundary layer (PDBL) (Calaf et al., 2010). The PDBL is adequately modelled by the filtered incompressible Navier–Stokes equations for neutral flows, expressed by means of the continuity and momentum equations which are shown to read

$$\nabla \cdot \tilde{\mathbf{v}} = 0, \quad (1a)$$

$$\frac{\partial \tilde{\mathbf{v}}}{\partial t} = -(\tilde{\mathbf{v}} \cdot \nabla) \tilde{\mathbf{v}} - \nabla(p_\infty + \tilde{p}^*) - \nabla \cdot \boldsymbol{\tau}_{\text{sgs}} + \sum_{i=1}^{N_s} \bar{\mathbf{f}}_i. \quad (1b)$$

The three-dimensional velocity field can be decomposed into its resolved component $\tilde{\mathbf{v}}$, for which we solve Eq. (1), and its residual component \mathbf{v}' . The filtered velocity field is parametrized by its streamwise \tilde{v}_x , spanwise \tilde{v}_y and vertical \tilde{v}_z flow components, respectively. The continuity equation, Eq. (1a), enforces the solenoidal properties of the filtered velocity field. The momentum equation, Eq. (1b), contains the local acceleration of the flow on the left-hand side, while the right hand side contains the convective acceleration and further collects the force contributions acting on the flow. The flow itself is driven by a constant imposed pressure gradient $\nabla p_\infty = [\partial_x p_\infty / \rho, 0, 0]$. The filtering operation results in a residual-stress tensor $\boldsymbol{\tau}_{\text{sgs}} = \widetilde{\mathbf{v}\mathbf{v}} - \tilde{\mathbf{v}}\tilde{\mathbf{v}}$ emulating the dissipation of kinetic energy at the sub-grid scales. The isotropic part of the residual-stress tensor is incorporated into the filtered modified pressure $\tilde{p}^* = \tilde{p} / \rho - p_\infty / \rho + \text{tr}(\boldsymbol{\tau}) / 3$, while the deviatoric part of the residual-stress tensor $\boldsymbol{\tau}_{\text{sgs}}$ is modelled using a closure model. Here, we opt for an eddy-viscosity Smagorinsky model with an height-dependent Smagorinsky length scale (Mason and Thomson, 1992) which reinforces the log-law behaviour of the ABL near the surface. Furthermore, an impermeable wall stress boundary condition is imposed at the bottom surface (Calaf et al., 2010). Finally, the body force term $\bar{\mathbf{f}}_i$ emulates the effects of AWE systems on the flow, for each of the N_s units of the park, by means of actuator methods and its derivation is elaborated in Sect. 2.1.2.

Large-eddy simulation of AWE parks are performed with our in-house solver SP-Wind developed at KU Leuven. The governing equations are discretised using a Fourier pseudo-spectral method in the horizontal directions (x, y) and a fourth-order energy-conserving finite-difference scheme in the vertical direction z . These discretisation methods require periodic boundary conditions in the horizontal directions: we circumvent periodicity in the streamwise direction x by applying a fringe-region technique (Munters et al., 2016). This technique also allows one to provide unperturbed turbulent inflow conditions to the AWE park simulation by performing a concurrent-precursor periodic PDBL simulation in parallel to the main AWE park simulation. Time integration is performed using a classical four-stage fourth-order Runge–Kutta scheme.

Actuator methods have proven their abilities to accurately reproduce wake characteristics of conventional wind turbines, such as the actuator line method (Sorensen and Shen, 2002; Troldborg et al., 2010; Martinez-Tossas et al., 2018) and the actuator sector method (ASM) (Storey et al., 2015). The dynamics of AWE systems and ABL flow span over a large range of spatial and temporal scales: while the AWES wing experiences local wind speed fluctuations within a few meters along the wingspan, the ABL domain covers several kilometres. In addition, the flight dynamics of AWE systems are extremely fast and require a temporal resolution down to 10ms whereas the large-scale flow structures evolve one to two orders of magnitude slower. Therefore, we opt for an actuator sector method that can both capture the local variations of aerodynamic quantities along the wingspans of individual AWE systems and accurately operate across a larger range of temporal scales. Similar to the actuator line method (ALM), the ASM projects the force distribution along the system wingspan onto the simulation grid of the LES, with an additional temporal smoothing that allows one to consider larger time horizon than just one instantaneous position of the AWE system. The resulting projected force distribution hence depends on the main parameters of the LES, ie. the grid resolution of the flow domain, parametrized by the cell size $\Delta_x, \Delta_y, \Delta_z$, and the simulation time step denoted by Δt , the time step of the AWE system dynamics denoted by δt , and a set of tuning parameters. While the methodology is outlined hereafter, Appendix A addresses the choice of LES settings and tuning parameters.

For the current AWE farm simulations presented later on, the cell size is $\Delta_x = 10\text{m}$ in the axial direction and the LES time step is set to $\Delta t = 0.250\text{s}$. In order to achieve a stable simulation of AWE system dynamics, which are much faster and require a smaller time step, its value is set to $\delta t = 0.010\text{s}$. Accordingly, the kinematics of the AWE system (see Sect. 2.2.3) are evaluated 25 times per LES time step. The LES flow field is however only updated after each time step Δt , hence AWE systems operate, for the duration of an entire LES time step, in a *frozen* flow field $\tilde{\mathbf{v}}^n \equiv \tilde{\mathbf{v}}(t = t^n)$ evaluated at the beginning of the time step.

From the perspective of the AWE system, the time horizon between the instants t^n and $t^{n+1} = t^n + \Delta t$ provides a static snapshot of the flow field and is further discretized into a collection of 25 sub-steps $t^l = t^n + l\delta t \in [t^n, t^{n+1}]$. At every sub-step t^l , the local aerodynamic forces (per unit segment length) $\mathbf{f}_q^l(s_k)$ are computed along the aircraft wingspan given its instantaneous position q^l in the frozen flow field. The procedure to compute $\mathbf{f}_q^l(s_k)$ is outlined in detail in Sect. 2.2.2. Subsequently, the local aerodynamic forces of each segment are smoothed out over the LES grid cells in the vicinity of the wing using a Gaussian convolution filter $G(\mathbf{x}) = \left(6/(\pi\Delta_f^2)\right)^{3/2} \exp\left(-6\|\mathbf{x}\|^2/\Delta_f^2\right)$ (Pope, 2000). The variance $\sigma^2 = \Delta_f^2/12$ of the Gaussian distribution, where the width of filter kernel is set to $\Delta_f = 2\Delta_x$ (Troldborg et al., 2010), is chosen to be similar to the second moment of the box filter. The instantaneous, spatially filtered forces, integrated over the complete normalised wingspan $s \in [-1/2, +1/2]$, read

$$\widehat{\mathbf{f}}^l(\mathbf{x}) = \int_{-1/2}^{+1/2} G(\mathbf{x} - \mathbf{q}(s)) \mathbf{f}_q^l(s) ds. \quad (2)$$

When flying crosswind manoeuvres at high speed, the AWE system may fly through several LES cells within one simulation time step Δt . For conventional wind turbines, blade tips sweeping several mesh cells in one time step result in a discontinuous

flow solution in the near wake (Storey et al., 2015). In order to avoid this discontinuity, the individual contributions of the spatially distributed forces $\widehat{\mathbf{f}}^l$ can subsequently be weighted in time using an exponential filter (Vitsas and Meyers, 2016) given a certain time horizon, hence sweeping over a sector of the LES domain. The time-averaged force distribution is given by

$$\overline{\mathbf{f}}^l = (1 - \gamma)\overline{\mathbf{f}}^{l-1} + \gamma\widehat{\mathbf{f}}^l. \quad (3)$$

The filter parameter γ is defined as $\gamma = \delta t / (\tau_f + \delta t)$ with the filter constant $\tau_f = 2\Delta t_{LES}$. The force distribution $\overline{\mathbf{f}}$ is then added to the momentum equation, Eq. (1b). The size of the sector, ie. the amount of sub-steps sampled, depends on the stage of the Runge-Kutta time integration scheme. At the first stage, only the force distribution evaluated at t^n is added to the previous sector. At the second and third stage, the force distributions between t^n and $t^n + \Delta t/2$ are further considered. While for the fourth and last stage, the new sector consists of the entire range of sub-steps between t^n and t^{n+1} . Ultimately, the added force distribution accurately captures the fast and local dynamics of each individual AWE system and emulates their collective effects onto the boundary layer flow.

170 2.2 Virtual plant: AWE system dynamics

The simulation strategy applied to AWE systems is shown in Fig. 1, part B. To describe and simulate the dynamics of AWE systems, there exist numerous models of varying complexity. These models range from fast quasi-steady models (Schelbergen and Schmehl, 2020), to simple 3DOF point-mass models (Zanon et al., 2013a), to complex 6DOF rigid-body models (Malz et al., 2019). The point-mass model allows the modelling of large-scale AWE systems while it does not require an extensive knowledge of the aircraft dimension and inertia, nor aerodynamic parameter identification, as is the case for the rigid-body model (Licitra et al., 2017). The point-mass model is therefore highly scalable. The model is also highly versatile and allows one to easily adapt generic wing designs to both ground-based and on-board generation AWE systems. In addition, the point-mass model has fewer states and control variables compared to the rigid-body model, resulting in a less computationally intensive model. Finally the point-mass model is tailored for the optimal control applications tackled in this work such as power-optimal trajectory generation and flight path tracking. Therefore, considering its simplicity and flexibility, we opt for the 3DOF point-mass model and present it in detail in Sect. 2.2.1.

Nevertheless, the 3DOF point-mass model also exhibits several limitations, mainly related to the lack of an explicit definition of the rotational dynamics of the system. Therefore, we derive the orientation and angular velocity of the system from state-based approximations. The approximation of orientation and angular velocity are further used to supplement the original point-mass model with a discrete lifting-line model that takes into account local wind speed fluctuations for a more accurate representation of the AWE systems in the turbulent wind field. The procedure, which enables to compute the instantaneous, local force distribution $\mathbf{f}_q^l(s)$ required in Eq. (2), is presented in Sect. 2.2.2.

Further, the equations of motion of AWE systems are derived from Lagrangian mechanics according to the procedure introduced by Gros and Diehl (2013) and outlined in Sect. 2.2.3.

190 2.2.1 Point-mass model

The architecture of AWE systems can be divided into three main key components: the ground station, the tether and the airborne device. In this work, we assume that the ground station has no influence on the atmospheric flow and can therefore be neglected. In addition, we neglect tether dynamics such as tether sag and represent the tether as a rigid rod of varying length (Malz et al., 2019), which is solely subject to aerodynamic drag. At last, we limit our investigation to rigid-wing aircraft. Given the large
 195 level of approximation of the model, we simply assume that the wing planform is elliptical and without twist, which further allows us to simplify the aerodynamic properties of the finite wing (Anderson, 2010).

Hence, the tethered wing is modelled as a 3DOF point-mass based on a representation of the system in non-minimal coordinates as proposed by Zanon et al. (2013). The system state vector $\mathbf{x} = (\mathbf{q}, \dot{\mathbf{q}}, C_L, \Psi, \kappa, l, \dot{l}, \ddot{l})^\top$ is composed of position \mathbf{q} and velocity $\dot{\mathbf{q}}$ of the wing, the instantaneous aerodynamic quantities such as lift coefficient of the finite wing C_L , roll angle Ψ and
 200 on-board turbine thrust coefficient κ as well as the tether variables l , \dot{l} and \ddot{l} , representing the length, speed and acceleration of the tether respectively. In absence of explicit control surfaces such as ailerons, elevators and rudders, we assume that the aerodynamic variables and the tether reel-out speed are directly and instantaneously controlled, hence we introduce the control vector $\mathbf{u} = (\dot{C}_L, \dot{\Psi}, \dot{\kappa}, \ddot{l})^\top$ which consists of the time derivatives of lift coefficient, roll angle and thrust coefficient, and the tether jerk.

205 The 3DOF point-mass model only considers the translational motion of the AWE system, while the rotational motion is neglected. Hence, the aircraft attitude, commonly defined by the basis frame of the rigid body, is not known. Instead, we define the reference frame in which the external aerodynamic forces \mathbf{F}_q acting on the system are expressed. First, we introduce the unit vector $\mathbf{e}_q = \mathbf{q}/\|\mathbf{q}\|$ and the apparent wind speed \mathbf{v}_a measured at the point mass. The apparent wind speed is defined as

$$\mathbf{v}_a = \mathbf{v}_w - \dot{\mathbf{q}}, \quad (4)$$

210 where \mathbf{v}_w is the three-dimensional wind speed vector, computed from the neighbouring LES cells surrounding the point-mass position \mathbf{q} using trilinear interpolation. Subsequently we define the basis vector $\mathbf{e}_v = \mathbf{v}_a/\|\mathbf{v}_a\|$, pointing along the apparent wind speed. Next, we introduce the perpendicular axis $\mathbf{e}_\perp = \mathbf{e}_q \times \mathbf{e}_v$ and the upward-pointing axis which is orthogonal to the plane spanned by $\{\mathbf{e}_v, \mathbf{e}_\perp\}$ and reads $\mathbf{e}_u = \mathbf{e}_v \times \mathbf{e}_\perp$. We apply a roll rotation of the perpendicular and normal axes about the axis $\mathbf{e}_v \equiv \mathbf{e}_D$ by an angle corresponding to the state variable Ψ , which results in the transversal and lift axes

$$215 \mathbf{e}_T = \sin(\Psi)\mathbf{e}_u + \cos(\Psi)\mathbf{e}_\perp \quad (5a)$$

$$\mathbf{e}_L = \cos(\Psi)\mathbf{e}_u - \sin(\Psi)\mathbf{e}_\perp, \quad (5b)$$

hence completing the basis of the frame of reference of the point mass $\mathbf{B}_{pm} = \{\mathbf{e}_D, \mathbf{e}_T, \mathbf{e}_L\}$. Furthermore, the basis vectors of \mathbf{B}_{pm} are the columns of the rotation matrix $\mathbf{R}_{pm} = [\mathbf{e}_D, \mathbf{e}_T, \mathbf{e}_L]$.

Next, we can compute the aerodynamic forces acting on the point mass. These forces can be computed from the model states
 220 and the wind conditions, either solely measured at the point-mass position or along the complete wing span by using a more complex model, the lifting line model, introduced in the upcoming section, Sect. 2.2.2.

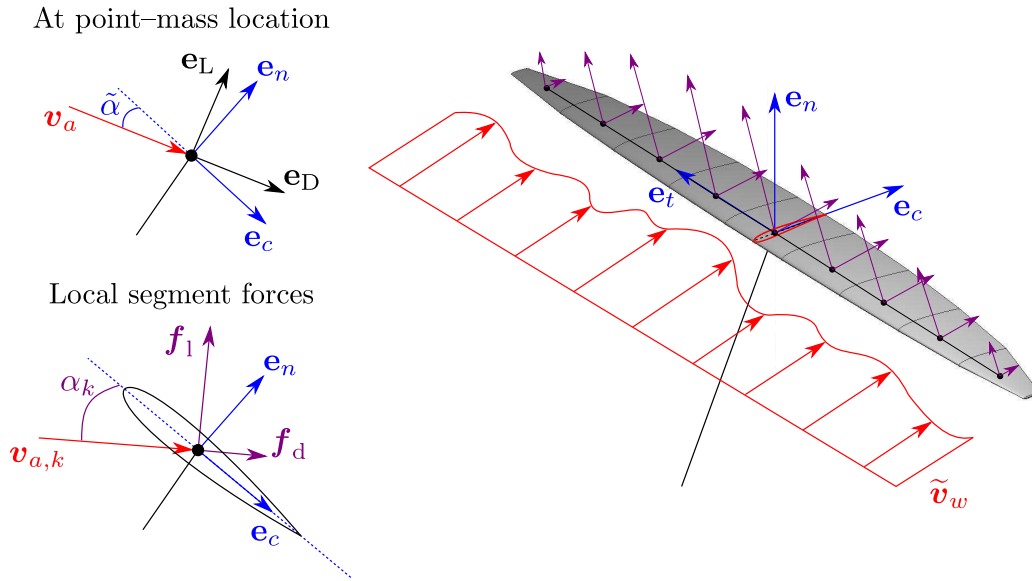


Figure 2. Sketch of the configuration used in the lifting-line model, showing the orientation of the AWE wing $\mathbf{B} = \{\mathbf{e}_c, \mathbf{e}_t, \mathbf{e}_n\}$ with respect to the incoming wind field $\tilde{\mathbf{v}}_w$ and the aerodynamic forces \mathbf{f}_l and \mathbf{f}_d acting on the wing sections for a given apparent wind speed $\mathbf{v}_{a,k}$.

2.2.2 Lifting-line model

The point-mass model provides the state and control variables that describe the flight path of the AWE system. The AWE system however operates in a turbulent boundary layer characterised by local fluctuations of the wind speed magnitude and direction, which given the large-scale of the system's wing, considerably influence the force distribution along the wingspan. Therefore, we supplement the original 3DOF point-mass model with the lifting-line model, which allows us to consider local fluctuations of (aero)dynamic quantities along the wingspan without adding complexity to the dynamics modelling and control of the aircraft. Hence, the wing is modelled as an aligned collection of discrete wing sections of width δs , for which we compute the aerodynamic forces based on the local wind condition.

The orientation of the wing is derived from a series of state-based assumptions building on the point-mass basis \mathbf{B}_{pm} introduced above and resulting in a new orientation basis $\mathbf{B} = \{\mathbf{e}_c, \mathbf{e}_t, \mathbf{e}_n\}$. First, we introduce the model-equivalent angle of attack $\tilde{\alpha}$ which we derive from the aerodynamic state C_L and can be computed as $\tilde{\alpha} = \alpha_{L=0} + C_L/a - C_L/(\pi AR)$ for elliptical wings (Anderson, 2010). This model-equivalent angle of attack defines the a priori unknown orientation of the aircraft chord line $\mathbf{e}_c = \cos(\tilde{\alpha})\mathbf{e}_D - \sin(\tilde{\alpha})\mathbf{e}_L$. The transverse axis of the body-fixed frame \mathbf{e}_t is aligned with the transverse axis of the point-mass frame \mathbf{e}_T and the normal axis of the body-fixed frame is given as the cross product $\mathbf{e}_n = \mathbf{e}_c \times \mathbf{e}_t$.

The rotation matrix \mathbf{R} associated to the body-fixed basis \mathbf{B} can be formulated in terms of Euler angles (Zanon, 2015) and can further be expressed as an extrinsic sequence of three consecutive rotations about the axes of the inertial frame

$$\mathbf{R} = \mathbf{R}_z(\psi)\mathbf{R}_y(\theta)\mathbf{R}_x(\phi), \quad (6)$$

with the Euler angles $\Theta = (\psi, \theta, \phi)$, respectively representing yaw, pitch and roll angles, and the associated rotations

$$240 \quad \mathbf{R}_x(\phi) = \begin{bmatrix} 1 & 0 & 0 \\ 0 & \cos(\phi) & -\sin(\phi) \\ 0 & \sin(\phi) & \cos(\phi) \end{bmatrix}, \quad \mathbf{R}_y(\theta) = \begin{bmatrix} \cos(\theta) & 0 & \sin(\theta) \\ 0 & 1 & 0 \\ -\sin(\theta) & 0 & \cos(\theta) \end{bmatrix}, \quad \mathbf{R}_z(\psi) = \begin{bmatrix} \cos(\psi) & -\sin(\psi) & 0 \\ \sin(\psi) & \cos(\psi) & 0 \\ 0 & 0 & 1 \end{bmatrix}. \quad (7)$$

The Euler angles are extracted from the entries r_{ij} of the orientation matrix \mathbf{R} (Licitra et al., 2019):

$$\phi = \arctan(r_{23}, r_{33}), \quad \phi \in (-\pi, \pi), \quad (8)$$

$$\theta = -\arcsin(r_{13}), \quad \theta \in (-\pi/2, \pi/2), \quad (9)$$

$$\psi = \arctan(r_{12}, r_{11}), \quad \psi \in (-\pi, \pi). \quad (10)$$

245 The angular velocity $\boldsymbol{\omega}$ of the aircraft can be derived from the Euler angle dynamics $\dot{\Theta}$. Accordingly, we first approximate $\dot{\Theta}$ by a discrete backward difference

$$\dot{\Theta} = (\Theta^m - \Theta^{m-1}) / (t^m - t^{m-1}), \quad (11)$$

and finally compute the angular velocity as

$$\boldsymbol{\omega} = \mathbf{A}^{-1} \dot{\Theta}, \quad (12)$$

250 where, for the given sequence of rotations (Alemi Ardakani and Bridges, 2010), the mapping function inverse reads

$$\mathbf{A}^{-1} = \begin{bmatrix} 1 & 0 & \sin(\theta) \\ 0 & \cos(\phi) & \cos(\theta)\sin(\phi) \\ 0 & -\sin(\phi) & \cos(\theta)\cos(\phi) \end{bmatrix}. \quad (13)$$

The approximations of the angular velocity $\boldsymbol{\omega}$ and the body-fixed basis frame \mathbf{R} can then further be used to define the position and speed of discretized wing elements of the AWE system.

From the state-based approximations of attitude and angular velocity of the aircraft, we can now evaluate the position and speed of each wing section k , defined at the section center, expressed in the inertial frame of reference as

$$\mathbf{q}_k = \mathbf{q} + \mathbf{R} \cdot (0, s_k, 0)^\top, \quad (14)$$

$$\dot{\mathbf{q}}_k = \dot{\mathbf{q}} + \mathbf{R} \cdot (\boldsymbol{\omega} \times (0, s_k, 0)^\top), \quad (15)$$

where s_k is the distance from the point mass to the segment center given in the body-fixed frame. In this study, each AWES wing is discretized using 61 actuator segments. The spatial discretization of the wing in the lifting-line model allows to account for the local fluctuations of the unsteady, three-dimensional wind speed. The local wind speed vector $\mathbf{v}_{w,k}$ is hence interpolated at the locations \mathbf{q}_k from the wind speed $\tilde{\mathbf{v}}$ measured at the surrounding LES cells. We define the local apparent wind speed $\mathbf{v}_{a,k} = \mathbf{v}_{w,k} - \dot{\mathbf{q}}_k$ and compute the effective angle of attack α_k seen by the airfoil of the wing section as

$$\alpha_k = \arctan \left(\frac{\mathbf{v}_{a,k}^\top \mathbf{e}_n}{\mathbf{v}_{a,k}^\top \mathbf{e}_c} \right). \quad (16)$$

The local lift and drag coefficient $c_l(\alpha_k)$ and $c_d(\alpha_k)$ of each wing section are determined from aerodynamic polars obtained from 2D airfoil analysis mentioned in Sect. 3.1.

The air density at each wing section is computed from the standard atmosphere density model (Archer, 2013) and reads

$$\rho_k = \frac{p_0}{RT_0} \left(\frac{T_0 - \Gamma q_{z,k}}{T_0} \right)^{\left(\frac{g}{\Gamma R} - 1 \right)}, \quad (17)$$

where $p_0 = 1013.25 \text{ hPa}$ and $T_0 = 288.15 \text{ K}$ are the reference pressure and temperature measured at sea level, $g = 9.81 \text{ m s}^{-2}$ is the gravity constant, $\Gamma = 6.5 \cdot 10^{-3} \text{ K/m}$ is the average lapse rate in the atmosphere and $R = 287.058 \text{ J/(kg K)}$ is the specific gas constant of dry air.

The chord length of each wing section, \tilde{c}_k is computed from the elliptical planform distribution of the wing according to

$$\tilde{c}_k = \frac{4b}{\pi AR} \sqrt{1 - \left(\frac{2s_k}{b} \right)^2}, \quad (18)$$

where b is the wingspan and AR the aspect ratio of the AWES wing. The values of b and AR are further discussed in Sect. 3.1. Finally, we can compute the local aerodynamic forces per unit segment length acting on each segment section. The instantaneous contributions of aerodynamic lift and drag forces read

$$\mathbf{f}_l(\mathbf{q}_k) = \frac{1}{2} \rho_k \tilde{c}_k c_l(\alpha_k) \|\mathbf{v}_{a,k}\| \mathbf{v}_{a,k} \times \mathbf{e}_t, \quad (19a)$$

$$\mathbf{f}_d(\mathbf{q}_k) = \frac{1}{2} \rho_k \tilde{c}_k c_d(\alpha_k) \|\mathbf{v}_{a,k}\| \mathbf{v}_{a,k}. \quad (19b)$$

Similarly, for drag-mode AWE systems, the additional drag of on-board turbines is distributed over n_g actuator segments, covering the central third of the wingspan. We assume that the individual on-board turbines all operate at the same value of the generator thrust coefficient κ , such that the local generator drag reads

$$\mathbf{f}_g(\mathbf{q}_{g,k}) = \frac{\kappa}{n_g} \|\mathbf{v}_{a,k}\| \mathbf{v}_{a,k} \quad (20)$$

for specific segments $k \in (1, n_g)$ or is zero otherwise. The instantaneous, local section force per unit segment length $\mathbf{f}_q^l(\mathbf{q}_k)$ at the time instant t^l contains the sum of local lift forces, drag forces and, if applicable, on-board turbine forces. This total force reads $\mathbf{f}_q^l(\mathbf{q}_k) = \mathbf{f}_l(\mathbf{q}_k) + \mathbf{f}_d(\mathbf{q}_k) + \mathbf{f}_g(\mathbf{q}_k)$ and can further be broadcast to Eq. (2) to be later added to the LES flow equations, Eq. (1b), or integrated over the complete wingspan to define the instantaneous, total aerodynamic forces acting on the wing

$$\mathbf{F}_W^l = \int_{-b/2}^{+b/2} \mathbf{f}_q^l(s) ds. \quad (21)$$

2.2.3 AWE system dynamics

In the current procedure, the system configuration is described by its set of generalized coordinates \mathbf{q} and its motion is restricted by the constraint $c(\mathbf{q}) = 0$, to which we associate the Lagrange multiplier λ . For the tethered single-wing AWE system

configuration considered in this study, the point-mass is constrained to the manifold described by

$$c(\mathbf{q}) = \frac{1}{2} (\mathbf{q}^T \mathbf{q} - l^2). \quad (22)$$

In order to obtain an index-1 DAE that can be integrated with Newton-based numerical methods, an index reduction is performed by differentiating the constraint (22) twice (Gros and Diehl, 2013). Baumgarte stabilization combined with periodicity
 295 constraints in the optimal control problem then ensures that the consistency conditions $c(\mathbf{q}) = 0$ and $\dot{c}(\mathbf{q}, \dot{\mathbf{q}}) = 0$ are satisfied during the entire power cycle (Gros and Zanon, 2017). The motion of the AWE systems is then defined by the set of equations

$$m\ddot{\mathbf{q}} + \lambda\mathbf{q} = \mathbf{F}_q - \bar{m}g\mathbf{1}_z, \quad (23a)$$

$$\ddot{c} + 2p\dot{c} + p^2c = 0. \quad (23b)$$

In Eq. (23a), $m = (m_W + \frac{1}{3}m_T)$ and $\bar{m} = (m_W + \frac{1}{2}m_T)$ define the effective inertial mass and the effective gravitational
 300 mass (Houska, 2007) with m_W and m_T representing the mass of wing and tether, and \mathbf{F}_q the aerodynamic forces acting on the system. In Eq. (23b), $p = 10$ is a tuning parameter of the Baumgarte stabilization scheme.

The total aerodynamic force acting on the system \mathbf{F}_q consists of the sum of wing forces \mathbf{F}_W from Eq. (21) and tether drag forces \mathbf{F}_T . The total tether drag (Argatov and Silvennoinen, 2013) is given by

$$\mathbf{F}_T = \frac{1}{8}\rho(d_T \cdot l) C_{\text{cyl}} \|\mathbf{v}_a\|^2 \mathbf{e}_D, \quad (24)$$

305 with the tether diameter d_T and the drag coefficient of a cylinder $C_{\text{cyl}} = 1.0$ at high Reynolds numbers.

The acceleration $\ddot{\mathbf{q}}$ and control inputs \mathbf{u} are obtained by respectively solving the DAE system (23) and the path tracking problem (36) detailed in Sect. 2.4. Finally, the kinematics of the AWE systems read

$$\frac{d}{dt}(\mathbf{q}, \dot{\mathbf{q}}, C_L, \Psi, \kappa, l, \dot{l}, \ddot{l})^\top = (\dot{\mathbf{q}}, \ddot{\mathbf{q}}, \dot{C}_L, \dot{\Psi}, \dot{\kappa}, \dot{l}, \ddot{l})^\top. \quad (25)$$

The kinematics of the systems (25) are further integrated in time using an internal four-stage fourth-order Runge–Kutta scheme
 310 with a sub-step size δt as previously mentioned in Sect. 2.1.2.

Unfortunately, directly feeding the lifting line forces \mathbf{F}_W (21) into the AWE system dynamics (23) in combination with the NMPC controller, presented later in Sect. 2.4, is not possible: The mismatch between the aerodynamic forces generated by the lifting line and the aerodynamic model of the point-mass assumed by the controller does not lead to a stable system in our implementation. Therefore, in order to reduce the model mismatch between plant and controller, we compute the total wing
 315 force at the point-mass position using the aerodynamic states as $\mathbf{F}_W = \mathbf{F}_L + \mathbf{F}_D + \mathbf{F}_G$, where the individual contributions of wing lift, wing drag and on-board turbine drag are given by

$$\mathbf{F}_L = \frac{1}{2}\rho(b^2/AR) C_L \|\mathbf{v}_a\|^2 \mathbf{e}_L, \quad (26a)$$

$$\mathbf{F}_D = \frac{1}{2}\rho(b^2/AR) C_D \|\mathbf{v}_a\|^2 \mathbf{e}_D, \quad (26b)$$

$$\mathbf{F}_G = \kappa \|\mathbf{v}_a\|^2 \mathbf{e}_D. \quad (26c)$$

320 This approach, while it still takes into account the unsteadiness of the LES wind field when computing the apparent wind speed \mathbf{v}_a at the point-mass location from Eq. (4), results in a satisfactory tracking performance of the controller.

2.3 Controller: park supervision

The procedure defining the supervision level of the AWE park is shown in Fig. 1, part C. The supervision level contains two modules: the wind speed estimator, presented in Sect. 2.3.1, and optimal trajectory generator, presented in Sect. 2.3.2. For each AWE system, the wind speed estimator samples the local wind conditions monitored at the wing and derives an approximation of the associated vertical wind profile. These wind profiles are further communicated to the trajectory generator and used to generate periodic power-optimal reference trajectories flown by each system individually.

2.3.1 Wind speed estimator

The controller does not have knowledge of the unsteady, three-dimensional wind field from the LES and hence assumes that the wind field is given by a one-dimensional, height-dependent profile $\mathbf{v}_w = (U(\mathbf{q}_z), 0, 0)$, where the streamwise wind speed component $U(\mathbf{q}_z)$ is given by the logarithmic distribution

$$U(\mathbf{q}_z) = U_{\text{ref}} \ln(\mathbf{q}_z/z_0) / \ln(z_{\text{ref}}/z_0). \quad (27)$$

The logarithmic distribution is parametrized by a reference speed U_{ref} given at an altitude z_{ref} and by a surface roughness length z_0 . Further, we consider offshore conditions such that the surface roughness height is $z_0 = 0.0002$ m (Troen and Lundtang Petersen, 1989) and we will use the altitude $z_{\text{ref}} = 100.0$ m as reference height at which the reference wind speed U_{ref} is measured.

When extracting power from the wind, conventional and airborne wind energy systems alike exert a thrust force on the incoming flow field (Jenkins et al., 2001). This process results not only in a velocity decrease downstream of the system, the wake, but also in a velocity decrease upstream of the system, the induction region. Upstream flow induction reduces the available power that wind energy systems can harvest. From one-dimensional momentum theory, it was shown for conventional wind turbines modelled as actuator disks that the velocity decrease across the actuator can be defined as

$$U_D = (1 - a) U_\infty, \quad (28a)$$

$$U_W = (1 - 2a) U_\infty, \quad (28b)$$

where the unperturbed inflow wind speed is denoted as U_∞ , while U_D and U_W respectively represent the wind speed at the actuator disk and in the wake. The axial induction factor a quantifies the strength of the induction phenomenon. The values of axial induction factors reported in AWE literature (Leuthold et al., 2017; Haas and Meyers, 2017; Kheiri et al., 2018) are lower than the known Betz limit $a = 1/3$ of conventional wind turbines (Jenkins et al., 2001), suggesting that axial induction is less significant for airborne wind energy systems although it cannot be fully neglected. In the current approach, the LES-based wind velocity sampled by the wind speed estimator already contains the effects of axial induction. Hence, optimal trajectories are later generated for reference wind speeds U_{ref} , computed by the wind speed estimator, and equivalent to the actuator-based wind speed U_D instead of the inflow wind speed U_∞ .

For each AWE system, the wind speed estimator monitors the system altitude and LES-based wind velocity measured at the point mass. In practice, the value of the wind speed can be derived from the measured airspeed using on-board instrumentation.

From the monitored time series, we approximate the vertical wind speed profile by estimating the related reference wind speed U_{ref} by means of a running-time average. For lift-mode AWE systems, the wind speed and altitude are sampled during one full periodic cycle consisting of four power-generation loops and one retraction phase. For drag-mode AWE systems, the data series are collected during five single-loop power cycles. The range of flight altitude $z \equiv q_z$ collected during the sample period T_s defines the sample space variable $Z = [z_{\text{min}}, z_{\text{max}}]$ with $H = z_{\text{max}} - z_{\text{min}}$. Over the interval H , the mean wind speed measured at the point-mass for the duration of the sampling period T_s is given by

$$360 \quad \langle \tilde{v}_x \rangle = \frac{1}{T_s} \int_t^{t+T_s} \tilde{v}_x(t) dt. \quad (29)$$

The mean wind speed, integrated from the logarithmic profile over the same interval h , is a linear function of the actuator speed and is given by

$$\langle U \rangle_H = \frac{1}{H} \int_{z_{\text{min}}}^{z_{\text{max}}} U(z) dz = U_D \lambda_H, \text{ with } \lambda_H = \frac{1}{H} \int_{z_{\text{min}}}^{z_{\text{max}}} \frac{\log(z/z_0)}{\log(z_{\text{ref}}/z_0)} dz. \quad (30)$$

Hence we can derive the reference value of the logarithmic wind profile that best approximates the wind conditions monitored by each AWE system during the sample period T_s as

$$U_{\text{ref}} \equiv U_D = \langle \tilde{v}_x \rangle / \lambda_H. \quad (31)$$

We further use this value to generate the associated reference trajectories as we show in Sect. 2.3.2.

2.3.2 Generation of reference trajectories

In this study we generate a set of reference flight trajectories by using optimal control techniques. Optimal control techniques allow us to optimize the flight of the AWE system for different objectives while respecting a large number of constraints during operation. First, we can generate power-optimal reference trajectories optimized for various flow conditions, as shown hereafter. Second, optimal control also allow us to perform path tracking of the reference trajectories in the turbulent LES flow field, as shown in Sect. 2.4.

The Lagrangian based modelling procedure applied to a tethered point-mass proposed Sect. 2.2.1 results in an implicit index-1 differential algebraic equation (DAE) given by (23) and (25). This representation can be summarized by

$$F(\dot{\mathbf{x}}(t), \mathbf{x}(t), \mathbf{u}(t), z(t), \theta, p) = 0, \quad (32)$$

In addition to the state and control vectors \mathbf{x} and \mathbf{u} , and the algebraic variables $z = (\lambda)$ previously defined, we introduce an additional optimization parameter θ and a set of constant parameters p , which allow us to apply the optimization problem for a number of AWE designs and wind conditions. The optimization parameter $\theta = d_T$ is the tether diameter and is optimized to sustain maximal tension $T_{T, \text{max}}$ during operation. The set of constant parameters $p = (m_W, b, AR, U_{\text{ref}}, z_{\text{ref}}, z_0)^\top$ contains the dimensions of the aircraft, its wing mass m_W , wingspan b and aspect ratio AR , as well as the reference wind speed and altitude U_{ref} and z_{ref} , and the roughness length z_0 parametrizing the wind conditions.

During operation, the AWE systems have to satisfy a set of constraints $h(\dot{\mathbf{x}}(t), \mathbf{x}(t), \mathbf{u}(t), z(t), \theta, p) \leq 0$ that ensure a hardware-friendly operation and the manoeuvrability of the aircraft. Hence, for the dynamics (32) and constraints h , we can
 385 formulate a periodic optimal control problem (POCP) with a free time period T_p as:

$$\min_{\mathbf{x}(t), \mathbf{u}(t), z(t), \theta, T_p} - \frac{1}{T_p} \int_0^{T_p} P(t) dt \quad (33a)$$

$$\text{s.t. } F(\dot{\mathbf{x}}(t), \mathbf{x}(t), \mathbf{u}(t), z(t), \theta, p) = 0, \quad (33b)$$

$$h(\dot{\mathbf{x}}(t), \mathbf{x}(t), \mathbf{u}(t), z(t), \theta, p) \leq 0, \quad (33c)$$

$$\mathbf{x}(0) - \mathbf{x}(T_p) = 0 \quad (33d)$$

390 The cost function is defined as the average mechanical power output of the system generated over a full cycle of period T_p . The instantaneous power generated by lift- and drag-mode AWE systems respectively read

$$P_L(t) = T_T(t) \dot{l}(t), \quad (34)$$

$$P_D(t) = \eta_r \mathbf{F}_G(t) |\mathbf{v}_a(t)|. \quad (35)$$

For lift-mode AWE systems, power is generated by unwinding the tether from the winch at a speed \dot{l} under the high tether
 395 tension $T_T = \lambda l$ generated by the aerodynamic forces acting on the wing. The power-generation phase consists of four loops and is followed by the retraction phase to wind the tether back up on the winch. For drag-mode AWE systems, power is extracted from the wind by on-board generators. These generators are modelled as actuator disks such that the power is equivalent to the turbine thrust force $\mathbf{F}_G = \kappa \|\mathbf{v}_a\|^2$ multiplied by the wind speed measured at the disk $\eta_r \|\mathbf{v}_a\|$. Here, $\eta_r = 0.8$ is the rotor efficiency and characterizes the ability of the on-board turbines to extract power from the surrounding flow, ie. the axial
 400 induction associated to the actuator disk assumption. In line with (Echeverri et al., 2020), where η_r is defined as "*rotor efficiency from thrust power to shaft power*", Eq. (35) defines the mechanical power that drag-mode AWE systems can extract from the wind.

The trajectory and performance of AWE systems depend on the path constraints and variable bounds specified in the periodic
 405 optimal control problem 33c. Tables 1 and 2 summarize the chosen constraints and bounds specified for trajectory optimization. The path constraints and variable bounds used in this work are compiled from the available literature (Gros and Diehl, 2013; Licitra et al., 2016; Zanon et al., 2013b; Kruijff and Ruitkamp, 2018) and are adapted to large-scale AWE systems. These choices are motivated hereafter: We set an operational upper limit to the tether length $l_{\max} = 1000$ m. We also limit the operation range of the winch by setting bounds to the tether speed \dot{l} and acceleration \ddot{l} . In addition, the aerodynamic lift coefficient of the wing C_L is restricted to the range $[0.0, C_{L,\text{opt}}]$, where $C_{L,\text{opt}} = 1.142$. The lower bound ensures that the
 410 tether tension remains positive at all time while the upper bound limits local stall along the wing. The value of the upper bound $C_{L,\text{opt}}$ stems from Figure 5 and its choice is further discussed in Sect. 3.1. The roll angle Ψ is bounded in order to ensure safe operation, ie. avoid collision between the tether and the airframe, and also take into account the reduced manoeuvrability of the large-scale aircraft. Next, the maximal tether tension and the maximal acceleration are limited to ensure the integrity of

Table 1. Bound constraints applied to state variables \mathbf{x} used in optimal control problem (33). The maximal lateral extent of the flight path and the maximal tether length are respectively set to $y_{\max} = 250$ m and $l_{\max} = 1000$ m to limit the footprint of the trajectories. The optimal value of the lift coefficient is $C_{L,\text{opt}} = 1.142$.

Quantity	q_x	q_y	q_z	C_L	Ψ	κ	l	\dot{l}	\ddot{l}
Units	m	m	m	-	deg	kg m^{-1}	m	m s^{-1}	m s^{-2}
Min	0.0	$-(y_{\max} - 1.5b)$	$1.5b$	0.0	-45.0	-20.0	0.0	-20.0	-10.0
Max	l_{\max}	$+(y_{\max} - 1.5b)$	+inf	$C_{L,\text{opt}}$	+45.0	+20.0	l_{\max}	+20.0	+10.0

Table 2. Bound constraints applied to control variables \mathbf{u} and other variables used in optimal control problem (33). The maximal tether tension depends on the wing design and is discussed in Sect. 3.

Quantity	\dot{C}_L	$\dot{\Psi}$	$\dot{\kappa}$	\ddot{l}	T_T	\ddot{q}
Units	s^{-1}	deg s^{-1}	kg (ms)^{-1}	m s^{-3}	kN	g
Min	-0.25	-5.0	-20.0	-100.0	0.0	0.0
Max	+0.25	+5.0	+20.0	+100.0	$T_{T,\text{max}}$	+8.0

the aircraft. The former also ensures that maximum tether stress is not exceeded by considering a safety factor $f_s = 3$ and a
415 tether yield strength $\sigma_{\max} = 3.09$ GPa. Further, we constrain the operation range of the control variables $\mathbf{u} = (\dot{C}_L, \dot{\Psi}, \dot{\kappa}, \ddot{l})^\top$
in order to avoid aggressive pitch and yaw manoeuvres which are not suited to large-scale aircraft. The bounds on \mathbf{u} are derived
using a heuristic approach in order to avoid unrealistic values of the approximated angular velocity. The spatial footprint of the
trajectories is limited by means of spatial constraints limiting the axial, lateral and vertical extents of the trajectories in order
to achieve system packing densities of $2/L^2$, as later discussed in Sect. 3.3.

420 In practice, the reference trajectories are optimized off-line for a specific range of wind speeds. We aim to operate the
AWE systems in below-rated from regime, the so-called region II (Leuthold et al., 2018), where the harvested power increases
with the wind speed, hence we generate a library of optimal trajectories (OTL) for a range of actuator-based wind speeds
 $U_D \in [5.0, 12.0]$ with an increment $\Delta U_D = 0.25$ m/s. Figure 3 shows the different trajectories computed for the range of wind
425 speeds. At the end of the sampling period T_s , the controller verifies whether the reference wind speed from Eq. (31) has
changed, and if so, chooses the closest value in the range $[5.0, 12.0]$ and commands the AWE system to track the new trajectory
defined by the reference states \mathbf{x}_r . The wind speed dependency of the trajectories is presented in Appendix B, Fig. B1 to B4.

2.4 Controller: flight path tracking

430 The procedure defining flight path tracking is shown in Fig. 1, part D. In the LES-generated virtual wind environment, the
operation conditions of the AWE systems differ substantially from the model assumptions in Eq. (27). The complex dynamics

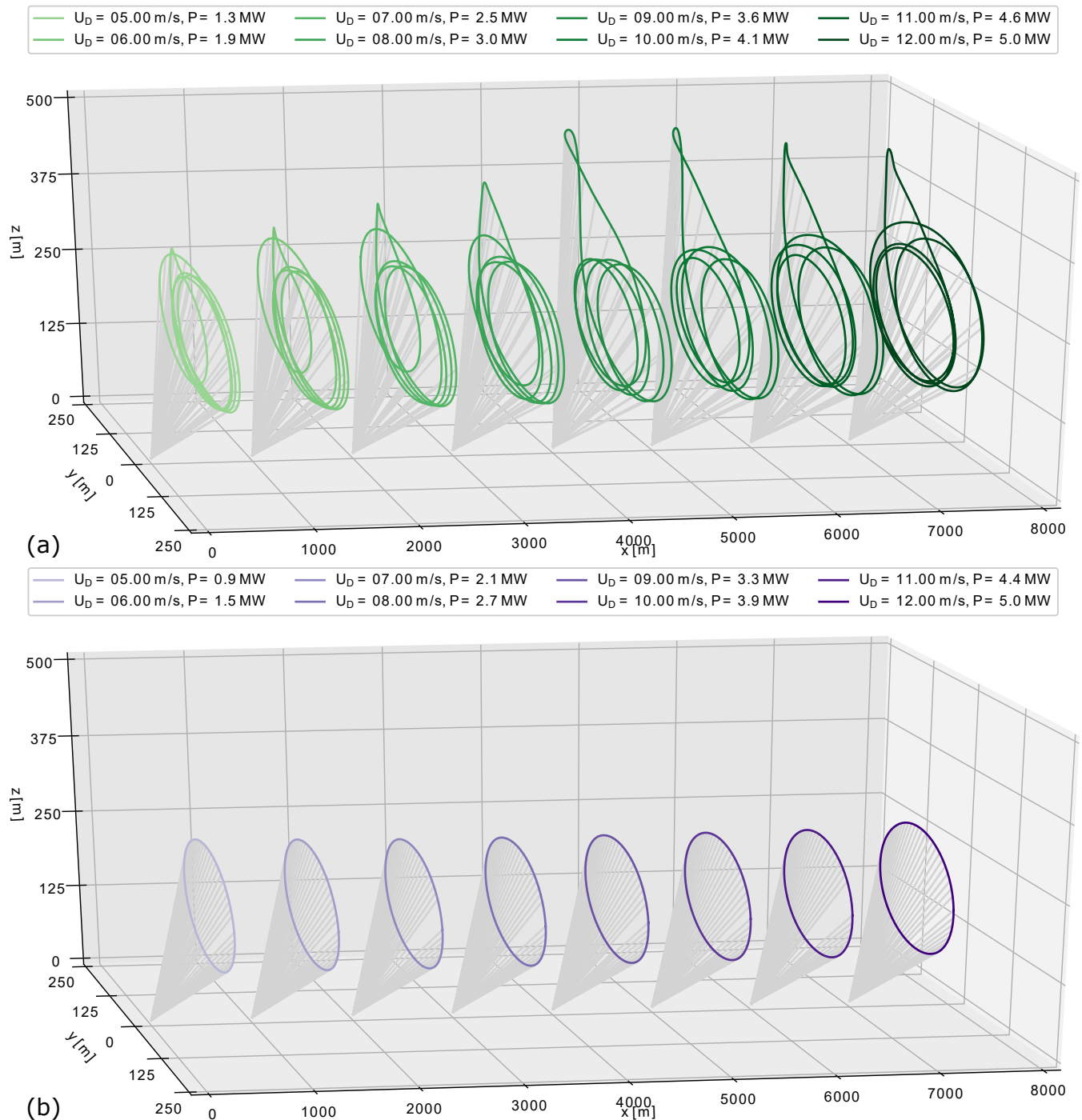


Figure 3. Power-optimal trajectories of (a) lift- and (b) drag-mode AWE systems optimized for the range of wind speed $U_D \in [5.0, 12.0]$ by solving the optimal control problem (33) under consideration of the variable constraints given in Table 1 and Table 2. The maximal streamwise extent of each trajectory does not exceed 1000 m, but for the sake of visualization the positions of successive ground stations were shifted by 1000 m.

make the motion of the AWE system highly sensitive to fluctuations. Therefore a control algorithm is required to lead the system onto its pre-computed optimized reference trajectory. Accordingly we apply non-linear model predictive control (NMPC) (Gros et al., 2013). For a moving time horizon, the NMPC repeatedly computes the optimal control inputs that reduce the error
435 between the current states \mathbf{x} and the states \mathbf{x}_r of the reference flight path taken from the OTL. Therefore, we can formulate for the prediction horizon T_c a new optimal control problem (36)

$$\min_{\mathbf{x}(t), \mathbf{u}(t), z(t)} \int_0^{T_c} (\|\mathbf{x}(t) - \mathbf{x}_r(t)\|_{Q_C}^2 + \|\mathbf{u}(t) - \mathbf{u}_r(t)\|_{R_C}^2) dt \quad (36a)$$

$$\text{s.t. } F(\dot{\mathbf{x}}(t), \mathbf{x}(t), \mathbf{u}(t), z(t), \theta, p) = 0, \quad (36b)$$

$$h(\dot{\mathbf{x}}(t), \mathbf{x}(t), \mathbf{u}(t), z(t), \theta, p) \leq 0, \quad (36c)$$

$$440 \quad \mathbf{x}_0 = \hat{\mathbf{x}}_0, \quad (36d)$$

$$\mathbf{x}(T_c) = \mathbf{x}_r(T_c), \quad (36e)$$

The cost function (36a) is formulated as a least-square objective, defining the tracking error between the current states $\mathbf{x}(t)$ and the given reference $\mathbf{x}_r(t)$, with a penalization on the deviation from both the reference states and controls. Just like for the generation of periodic optimal trajectories, the constraints (36b) and (36c) enforce the system dynamics and path constraints,
445 while the initial condition (36d) ensures that the initial states match the current estimate $\hat{\mathbf{x}}_0$. An additional terminal condition (36e) ensures the system finds back the reference at the end of the prediction horizon. Some of the path constraints in Eq. (36c), in particular the aerodynamic states and the control variables, are relaxed compared to the POCP bounds in tables 1 and 2. This allows the controller to handle wind disturbances and plant-controller model mismatch with a wider range of steering strategies. Table 3 summarizes the NMPC constraints and bounds adapted for trajectory tracking. The maximal allowed lift
450 coefficient $C_{L,\max} \approx 1.37$ corresponds to the upper bound of the validity range of the linear lift slope of the elliptical wing. Similarly to $C_{L,\text{opt}}$ for the trajectory generation, the value of the upper bound $C_{L,\max}$ stems from Figure 5 and its choice is discussed in Sect. 3.1. In addition, the maximal allowed tether tension and acceleration are relaxed by respectively 10% and 20%.

To solve the optimal control problems, we use the `awebbox` toolbox (awebbox, 2021). In the toolbox, both trajectory gener-
455 ation and flight path tracking OCPs are discretised using the direct collocation approach based on a Radau scheme with order 4 polynomial. The resulting nonlinear program is formulated using the symbolic framework CasADi (Andersson et al., 2018) and solved with the interior-point solver IPOPT (Wächter, 2002) using the linear solver MA57 (HSL, 2011). More information about the implementation can be found in (De Schutter et al., 2019).

Table 3. Relaxed variable bounds used in non-linear model predictive control (36). The maximal value of the lift coefficient is $C_{L,\max} \approx 1.37$.

Quantity	C_L	\dot{C}_L	Ψ	$\dot{\Psi}$	κ	$\dot{\kappa}$	i	\dot{i}	\ddot{i}
Units	-	s^{-1}	deg	deg s^{-1}	kg m^{-1}	kg (ms)^{-1}	ms^{-1}	ms^{-2}	ms^{-3}
Min	0.0	-0.5	-54.0	-10.0	-24.0	-24.0	-20.0	-15.0	-150.0
Max	$C_{L,\max}$	+0.5	+54.0	+10.0	+24.0	+24.0	+24.0	+15.0	+150.0

460 3 Simulation setup

The different AWES park configurations investigated in the current work are presented hereafter. First, we detail the design choices behind the large-scale lift- and drag-mode AWE systems in Sect. 3.1. Next we discuss the mode-specific operation of both the lift- and drag-mode AWE systems, in particular the effects of wind speed on the system performance, in Sect. 3.2. Finally, we specify the computational settings of the performed LES of the atmospheric boundary layer and present the
465 different AWES park layouts used in this study in Sect. 3.3.

3.1 Design of large-scale AWES

For given wind conditions and space constraints, wind farm developers design their parks such as to optimize several design metrics. Traditionally, these metrics include the annual energy production (AEP) and the levelized cost of energy (LCOE) (Dykes, 2020). In order to minimize the LCOE, wind farms of conventional wind turbines in the range 10–15 MW target
470 power densities of approximately 5 MW km^{-2} (Bulder et al., 2018). For the large-scale deployment of their technologies, AWE manufacturers have engaged in the development of utility-scale multi-megawatt AWE systems for offshore operation generating up to 5 MW of power (Kruijff and Ruiterkamp, 2018; Harham, 2012). Also, the AWE manufacturer Ampyx Power aims at achieving farm level power densities in the range of 10–25 MW km^{-2} with their commercial systems (Kruijff and Ruiterkamp, 2018). Accordingly, when designing parks of AWE systems, one has to define first the type of AWE systems used
475 to harvest power and second the layout of the farm that will ensure a safe operation while maximizing the power density.

Hence, we propose a generic design for lift- and drag-mode AWE systems that is easily scalable and allows one to model the operation of AWE systems in various wind conditions. The wingspan b of the wing is chosen as the driving design parameter to describe the dimensions of the different systems while the wing aspect ratio is fixed to $AR = 12$, similar to the AWE systems developed by Ampyx Power. Design considerations such as manufacturability or structural analysis of the wing lie outside of
480 the scope of the study. Therefore, a wing with elliptical planform is chosen here for simplicity. Elliptical wings exhibit advantageous aerodynamic properties given that their planforms generate low induced drag. Nevertheless, their stall characteristics are unfavourable: Elliptical wings generate a constant downwash along the wingspan. Therefore, in the absence of geometric twist and for a uniform airfoil distribution, the induced angle of attack is constant along the wingspan. As a consequence, the effective angle of attack of each wing section is equal, which might cause the entire wing to stall simultaneously. Elliptical

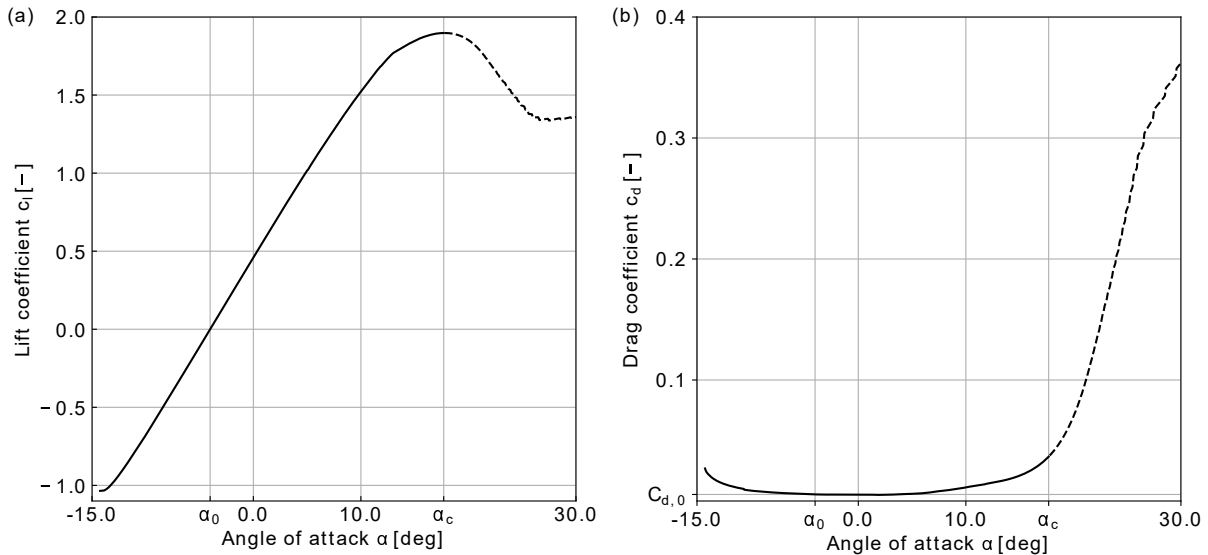


Figure 4. Aerodynamic polars of the SD 7032 airfoil generated at a chord-based Reynolds number $Re_c = 10^7$ with XFLR5: (a) Lift coefficient polar and (b) drag coefficient polar. The dashed lines show the coefficient values past the critical angle of attack $\alpha_c \approx 17.7$ deg. The zero-lift angle of attack of the airfoil is $\alpha_{L=0} \approx -4.0$ deg while the profile drag coefficient is $C_{d,0} = 0.0054$.

485 wings provide an analytical formulation of the aerodynamic lift and drag coefficients of the wing (Anderson, 2010)

$$C_L = a(\alpha_g - \alpha_{L=0}), \text{ and } C_D = C_{d,0} + \frac{C_L^2}{\pi AR}, \quad (37)$$

where α_g is the geometric angle of attack of the wing. In addition, $\alpha_{L=0}$ and $C_{d,0}$ respectively represent the zero-lift angle of attack and profile drag coefficient of the airfoil. The lift slope a of the finite wing is given by $a = a_0 / (1 - a_0 / (\pi AR))$ with $a_0 = 2\pi$ the airfoil lift slope from inviscid flow theory. The discussed properties of the elliptical wing and the aerodynamic coefficients given in Eq. (37) are valid for steady-state, level flight, nevertheless they will be used as surrogate model for the wing of the AWE system: This model is used to approximate the wing orientation in the lifting-line model introduced in Sect. 2.2.2 and to derive the state bounds of C_L in the AWES model of the controller in Sect. 2.3 and Sect. 2.4. Unsteady aerodynamic effects, which are not considered here but might play a significant role for AWE systems, need to be addressed in the future.

In order to achieve a high lift-to-drag ratio, we opt for airfoil sections of type SD 7032, also used by the manufacturer 495 TwingTec (Gohl and Luchsinger, 2013). The lift and drag polars of the airfoil are computed from an XFOIL direct analysis using the open-source software XFLR5 (XFLR5, 2021) at a chord-based Reynolds number $Re_c = 10^7$ and shown in Fig. 4. From the airfoil analysis, we can retrieve the values of the zero-lift angle of attack $\alpha_{L=0} = -4.0174$ deg, of the critical angle of attack $\alpha_c = 17.7$ deg and of profile drag coefficient $C_{d,0} = 0.0054$. Past the critical angle of attack α_c , the airfoil is subject to stall, characterized by a drop of the lift coefficient and a sharp increase of the drag coefficient.

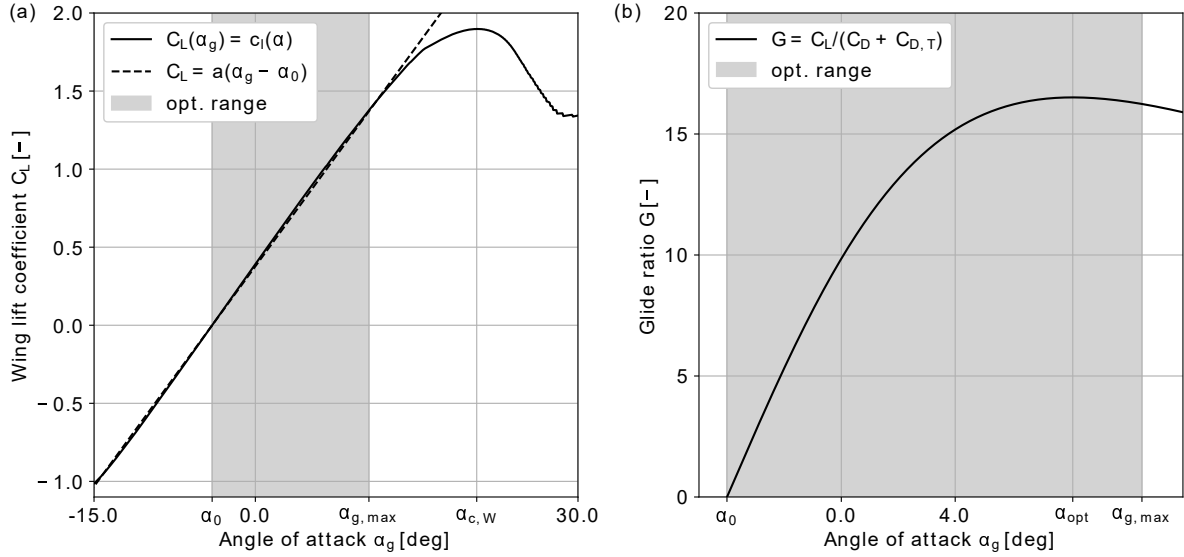


Figure 5. Aerodynamic quantities of the finite wing with aspect ratio $AR = 12$: (a) Wing lift coefficient and (b) glide ratio. The shaded area shows the optimization range of the optimal control problems (33) and (36) in between the zero-lift angle of attack of the airfoil $\alpha_{L=0} \approx -4.0$ deg and the maximal value $\alpha_{g,max} \approx 10.6$ deg of the validity range of linear approximation (37). The critical angle of attack of the wing is $\alpha_{c,W} \approx 20.6$ deg and the angle of attack corresponding to the maximal value of the glide ratio is $\alpha_{opt} \approx 8.1$ deg.

500 The lift and drag predictions of XFOIL are only valid just beyond α_c (XFOIL, 2021). In addition, the distribution of angles of attack in the lifting-line model can vary substantially along the wingspan, due to the spatial fluctuations of the LES-based wind velocity and the speed difference between the two tips of the aircraft. Therefore, the operation of AWE system is to be optimized such that not only the adverse effects of stall are avoided but also ensure an accurate prediction of the aerodynamic behaviour of local wing sections of the lifting line. To do so, we restrict the values of the states variable C_L , and equivalently
505 the values of the model-equivalent angle of attack $\tilde{\alpha}$, to a range well below stall, as explained hereafter.

The linear approximation of the wing lift coefficient given in Eq. (37) is only valid for the range of angles of attack up to $\alpha_{g,max} \approx 10.6$ deg, well below the critical angle of attack of the wing $\alpha_{c,W} \approx 20.6$ deg, as shown in Fig. 5(a). Therefore, the upper bound of C_L is set to a value $C_{L,opt} \in [0.0, C_L(\alpha_{g,max}) \equiv C_{L,max}]$ that maximizes the glide ratio G of the tethered wing system: The glide ratio $G = C_L / (C_D + C_{D,T})$ is defined as the ratio of aerodynamic lift forces to the combined contribution of wing and tether to the overall drag forces (Diehl, 2013). The contribution of the tether is given as
510 $C_{D,T} = C_{cyl}(l_{max}d_T)AR / (4b^2)$ with the drag coefficient of a cylinder at high Reynolds number $C_{cyl} = 1.0$. For the targeted wingspan of 60m and an expected tether diameter of 3.5×10^{-3} m, the maximal glide ratio $G \approx 16.5$ is achieved at a geometric angle of attack of $\alpha_g \approx 8.1$, and results in $C_{L,opt} = 1.142$, as shown in Fig. 5(b). Consequently, the upper bound of the wing lift coefficient is $C_{L,opt} = 1.142$ in the POCP (33) and $C_{L,max} = 1.37$ in the NMPC (36). A discussion of the angle of attack
515 and load distributions of the trajectories optimized with (33) and using this approach is presented in appendix A2.

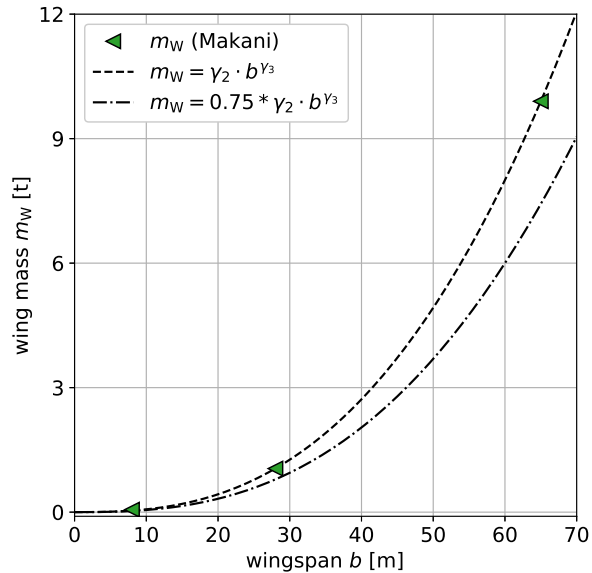


Figure 6. Scaling of the wing mass with the wingspan of the aircraft based on manufacturer data from Makani Power (Harham, 2012). The dashed line shows the power law fitted from data with $\gamma_2 \approx 0.1478$ and $\gamma_3 \approx 2.662$ used for drag-mode AWE systems while the dashed-dotted line shows the power law with a 25% reduction of the mass as used for lift-mode AWE systems.

The remaining necessary dimensions of the AWE systems are derived from a semi-empirical study based on available manufacturer data, where we derive the wing mass and tension limits from the wingspan b . We set an upper bound to the tether tension and assume that it scales linearly with the surface area of the wing. Further we assume that the targeted AWE system with a 60 m wing with aspect ratio 12 can sustain up to approximately 850kN of pulling force from the tether. Further, the wing mass is estimated by fitting a power law onto data from the manufacturer Makani Power taken from (Harham, 2012) as shown in Fig. 6. Hence wingspan-based relations for the maximal tether tension and the wing mass read

$$T_{T,\max} = \gamma_1 \frac{b^2}{AR}, \quad (38)$$

$$m_W = \gamma_2 \cdot b^{\gamma_3}, \quad (39)$$

with the parameters $\gamma_1 \approx 2840.24$, $\gamma_2 \approx 0.1478$, $\gamma_3 \approx 2.662$. Note that for lift-mode AWE systems, the wing mass is reduced by 25% in order to account for the absence of on-board turbines. Finally, the tether material is assumed to be Dyneema for both types of AWE systems. This material is commonly used by AWE manufacturers and has a density $\rho_T = 970.0 \text{ kg/m}^3$.

3.2 Operation of large-scale AWE systems

We apply the optimization procedure outlined in Sect. 2.3.2 to optimize the dimensions and flight path of three different AWE systems targeted at offshore operation and capable of generating 5MW of rated power for a design wind speed $U_D =$

Table 4. Wing and tether characteristics of the reference trajectories optimized for lift- and drag-mode AWE systems at rated wind speed $U_D = 12 \text{ m s}^{-1}$ under consideration of offshore conditions.

Quantity	P	b	S	AR	m_W	l_T	$T_{T,\max}$	d_T	T_p
Units	MW	m	m^2	–	kg	m	kN	mm	s
Lift-mode (1)	5.0	61.0	310.1	12.0	6270.0	514.6 – 887.3	880.7	33.0	64.1
Lift-mode (2)	5.0	63.5	336.0	12.0	6977.5	530.0 – 889.6	954.4	34.3	66.5
Drag-mode	5.0	57.0	270.8	12.0	6979.1	646.4	769.0	30.8	9.7

530 12.0 m s^{-1} . We design and optimize one drag-mode AWE system and two different lift-mode AWE systems, of which we discuss the operation characteristics in Sect. 3.2.1. Table 4 summarizes the main dimensions of wing and tether of the three considered AWE systems. For lift-mode AWE systems, preliminary work on single AWE systems has highlighted the effect of reel-out speed on the instantaneous flow conditions experienced by the system. Therefore, we use two different reel-out strategies for the operation of lift-mode AWE systems, which we discuss in Sect. 3.2.2. The details of the single AWE system analysis are given in appendix A. The first strategy uses the hypothetical physical limitations of the winch, where we assume 535 that the maximal reel-out speed is $\dot{l}_{\max} = 20.0 \text{ m s}^{-1}$ as given in Table 1. However, given that the optimization procedure does not take the generation of the system wake into account, the wing can potentially interact locally with its own wake during the reel-out phase as discussed in Sect. 3.2.2. Therefore, the second strategy limits the maximal reel-out speed to the expected advection speed of the wake U_W as estimated in Eq. (28). While the value of the induction factor a is a priori unknown, we opt 540 for the conservative guess $a = 0.25$ based on an empirical choice, such that the maximal reel-out speed of the tether becomes wind speed-dependent and is shown to read

$$\dot{l}_{\max} = \frac{(1 - 2a)}{(1 - a)} U_D. \quad (40)$$

Given that the individual AWE systems in the farm operate in different wind conditions, we also generate their trajectories for a large range of wind speeds below rated wind speed. Hence, each system can adapt its flight path and power performance 545 to the temporarily experienced wind field as introduced in Sect. 2.3. The effects of varying wind speed on the AWE system trajectories are discussed in Sect. 3.2.3.

3.2.1 Operation at rated wind speed

At rated wind speed, the drag-mode AWE system and the two lift-mode AWE systems all generate 5 MW of power. However, 550 their flight path and power generation profile differ substantially as shown in Fig. 7. A complete description of all system states, controls and additional metrics is given in appendix B, and their main features are summarized here.

The drag-mode AWE system operates at a constant tether length $l \approx 650 \text{ m}$ and follows an near-circular flight path of diameter $D \approx 200 \text{ m}$ at a mean elevation of about 17 degrees. The duration of a single-loop periodic cycle equals approximately

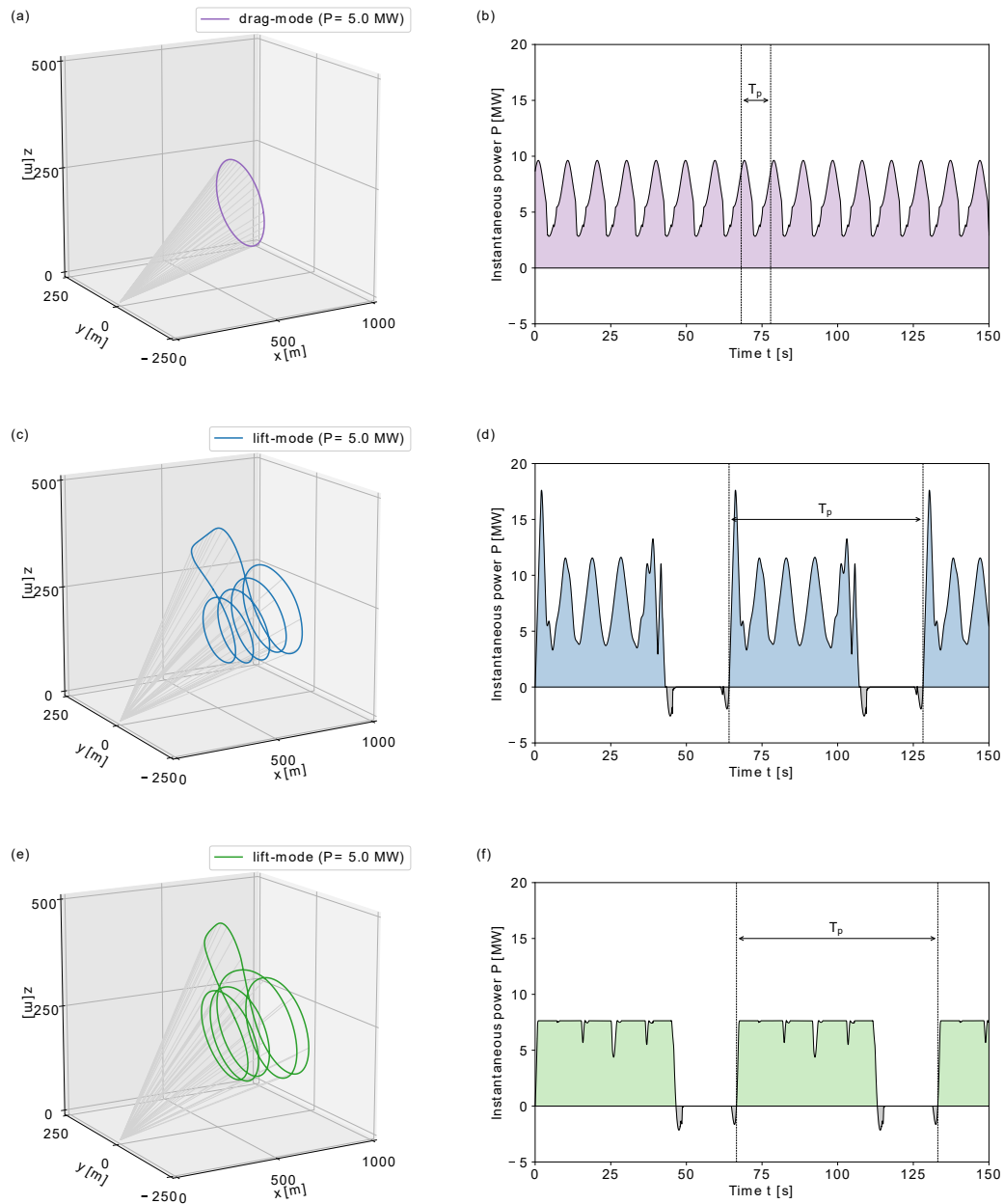


Figure 7. Flight path and instantaneous power of 5 MW reference lift- and drag-mode AWE systems optimized for given rated wind speed $U_D = 12 \text{ m s}^{-1}$ under consideration of offshore conditions. (a–b) Drag-mode AWE system, (c–d) lift-mode AWE system (1) with original bounds and (e–f) lift-mode AWE system (2) with induction-based limitation of reel-out speed.

10s. The system operates at maximal tether tension maintaining a high flight speed between 60 m/s and 80 m/s throughout the
555 cycle. The on-board turbines of the system continuously generate power while reaching peak generation during the downward
flight when the maximal flight speed is achieved.

For the two lift-mode AWE systems, one periodic cycle consists of four power-generating loops and a retraction phase.
The duration of the periodic cycle ranges between approximately 64 s and 66 s, while the reel-out phase accounts for about
70% of the cycle. During the reel-out phase, the tether length varies approximately between 500 m and 900 m, while the loop
560 diameters ranges between 200 m and 250 m and the mean elevation angle is approximately 19 degrees. Mechanical power is
generated by reeling out the tether at high speed under maximal tether tension. The retraction phase consists of a steep upward
flight at maximal tether length to transition out of the last power generation loop, followed by the reel-in phase of the tether at
high altitude and is completed by a dive manoeuvre to transition into to the new power-generation phase. During the retraction
phase, the tension on the tether is minimal and a fraction of the generated power is used to reel-in the tether. With the first reel-
565 out strategy, the reel-out speed fluctuates during each individual loop, reaching its peak during the downward flight, resulting
in large variations of instantaneous power generation. The flight speed of the systems remains nearly constant during the
duration of the production phase, fluctuating between approximately 60 ms^{-1} and 70 ms^{-1} . With the second strategy, the reel-
out speed of the tether is capped by the induction-based constraint such that the tether is reeled out at a nearly constant speed.
Accordingly, the generated power remains nearly constant during the generation phase. Given the reel-out speed limitation, part
570 of the kinetic energy of the system is used to accelerate the system during the downward flight resulting in large fluctuations
of the flight speed in the range 60 ms^{-1} to 90 ms^{-1} .

3.2.2 Characteristics of lift-mode operation

In order to assess the different reel-out strategies, we investigate in details the operation of individual lift-mode AWE systems.
For this analysis, the systems operate in a high-resolution logarithmic inflow with reference wind speed $U_D = 10.0\text{ m/s}$ without
575 ambient turbulence and their trajectories are optimized for the same wind conditions. We further assume that the wind condi-
tions remain constant over time and the systems are "*perfectly steered*", suggesting that the systems can perfectly follow their
reference flight path with the reference controls, hence making the controller part of the framework obsolete for this analysis.
The detailed analysis is given in appendix A, which also includes a grid convergence study and an evaluation of the different
actuator methods introduced in Sect. 2.1.2.

580 Figure 8 shows the structure of the wake flow for both lift-mode AWE systems at the end of the reel-out phase. During
the power-generation phase, the wing is subject to high lift forces such that tip vortices emanate from the wing tips and are
transported downstream by the background flow. These wing tip vortices generated during the individual loops start to interact
with each other in the wake and eventually merge into a more significant single structure, which eventually breaks down further
downstream due to the effect of mixing. In particular, the figure shows the effect of the reel-out strategy on the generation of
585 tip vortices: With the first reel-out strategy, the individual tips vortices of each loop cannot be precisely identified, suggesting
that the induced tip vortices are advected downstream by the background flow at a speed similar to the reel-out speed of the
tether. Consequently, the wing interacts with its own wake during the reel-out phase. With the second strategy, the induction-

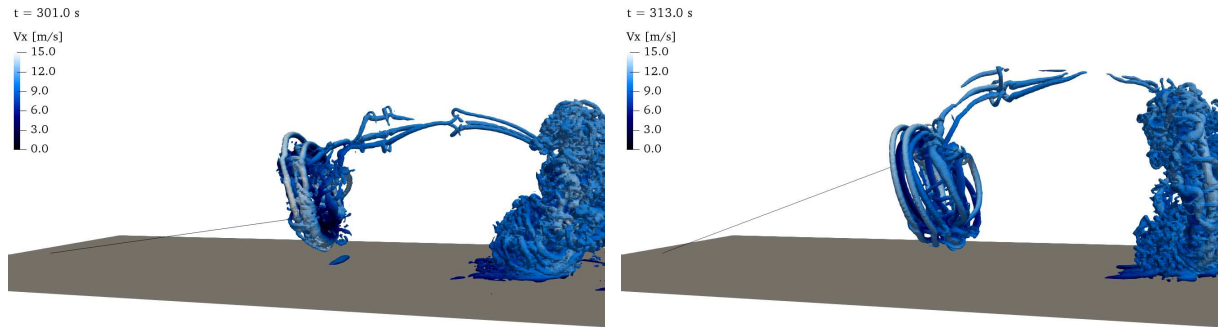


Figure 8. Instantaneous lateral snapshots of the wake field of reference lift-mode AWE systems operating in an unperturbed logarithmic inflow at a wind speed $U_D = 10 \text{ m s}^{-1}$. Isovolumes of positive Q-criterion, colored by streamwise velocity \tilde{v}_x for (left) lift-mode AWE system with original bounds at $t = 301 \text{ s}$ and (right) lift-mode AWE system with induction-based limitation of reel-out speed at $t = 313 \text{ s}$.

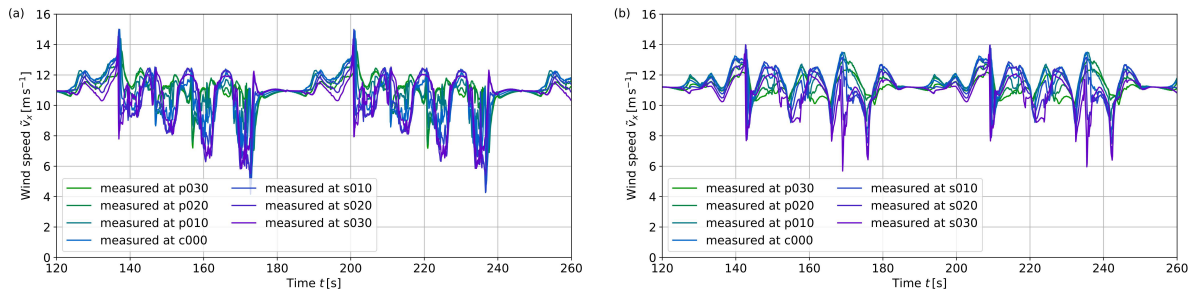


Figure 9. Instantaneous values of streamwise velocity \tilde{v}_x measured at several locations along the wingspan for (a) lift-mode AWE system with original bounds and (b) lift-mode AWE system with induction-based limitation of reel-out speed. The prefixes "p" and "s" stand for the port and starboard sides of the wing, while the prefix "c" stands for the center, ie. the point-mass. Furthermore, the numbers stand for the segment positions on each side of the wing, from 0 at the center to 30 at the wing tip.

based limitations of the reel-out speed reduces the interaction between the tip vortices at each loop, resulting in more distinct structures. The interaction can however not be completely prevented, such that the individual structure eventually merge later
590 downstream.

The effects of the reel-out strategy on wing-wake interaction can also be observed on the local flow conditions measured by the wing. Figure 9 shows the instantaneous streamwise wind speed component \tilde{v}_x monitored at seven equidistant locations along the wingspan. For comparison, not that without interaction between the AWE system and the wind environment, wing sections would experience wind speeds in the range 9.7–10.9 m/s. For the first reel-out strategy (see Fig. 9(a)), we observe
595 large fluctuations of the instantaneous wind speed: Sharp drops of the streamwise velocity components are measured during the lower part of the four power-generation loops. These drops are particularly important for the entire starboard side (sections $c000$ to $s030$) suggesting that a large portion of the wing suddenly encounters a region of low wind speed that we can identify as the wake. Furthermore, the intensity of the velocity drop increases after every loop as the system reels out further down-

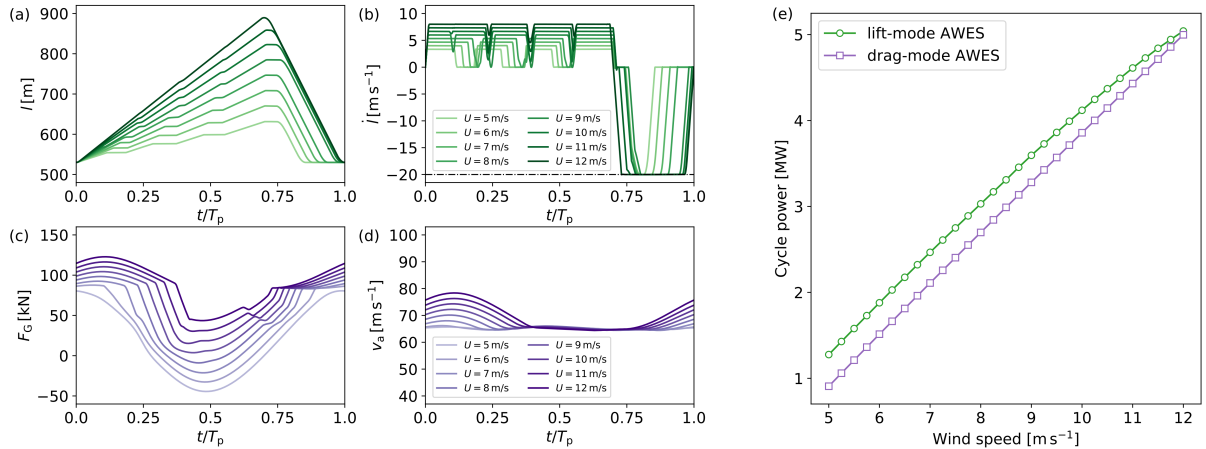


Figure 10. Selected trajectory features (a–d) and power curves (e) of lift- and drag-mode AWE systems in region II. For lift-mode AWE systems, the wind-speed dependency of tether length and reel-out speed are shown in sub-figures (a) and (b). For drag-mode AWE systems, the wind-speed dependency of generator thrust and apparent wind speed magnitude are shown in sub-figures (c) and (d).

stream, indicating that the individual wakes of each loop are combined into a single wake. With the second reel-out strategy (see Fig. 9(b)), the patterns are less distinct and the magnitude of the fluctuations less significant, hence indicating that the interaction between wing and wake is limited. We still observe that the outer starboard part of the wing (sections $s020$ and $s030$) experiences sharp fluctuations suggesting that the starboard wing tip flies through some wake region. However, these fluctuations are very local and temporary, while for the first reel-out strategy most of the wing is interacting with the wake.

Given the limited interaction between the wing and the wake when using the second reel-out strategy, ie. with a induction-based upper limit of the reel-out speed, we will perform the lift-mode AWES farm simulation with the second design of lift-mode AWE system.

3.2.3 Operation of large-scale AWES in below-rated regime

When operating in a park, AWE systems are subject to large-scale wind speed variations and wakes of upstream systems. As a result, the operation of each individual system evolves as it experiences different wind conditions. Hence, we discuss here the effect of varying wind speed on the trajectories of drag- and lift-mode AWE systems. The power curves and selected metrics for the expected range of wind speeds $5.0 \text{ ms}^{-1} \leq U_D \leq 12.0 \text{ ms}^{-1}$ are shown in Fig. 10, while the wind-speed dependency of the flight path is shown in Fig. 3. A complete description of the effects of varying wind conditions on all system states, controls and additional metrics are given in appendix B

For the expected range of wind speeds, the generated power ranges from approximately 1 MW to 5 MW for both operation modes. For lift-mode AWE systems, decreasing wind speeds mainly affect the reel-out patterns. At low wind speeds, the system only reels-out, and hence generates power, during the downward part of the loops. In comparison, the upward flight

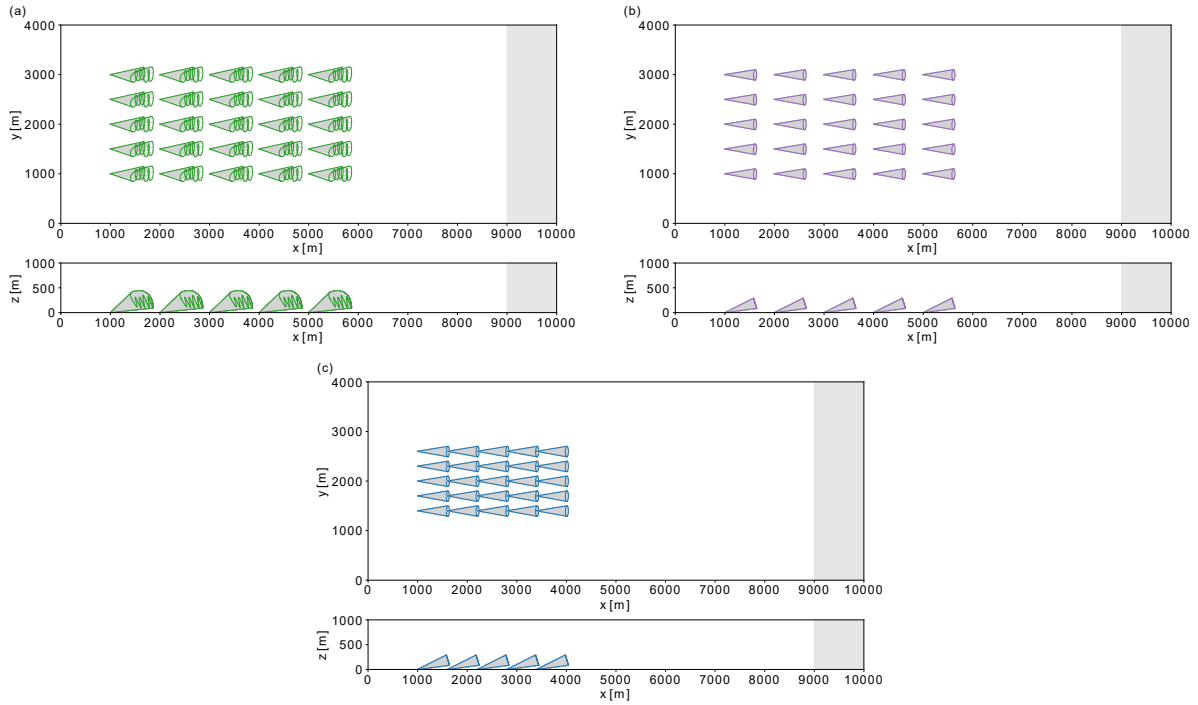


Figure 11. Visualizations of top and side views of AWE park layouts in the main LES domain. (a) lift-mode AWE park with layout 1 (L1), (b) drag-mode AWE park with layout 1 (D1) and (c) drag-mode AWE park with layout 2 (D2). The gray area represents the fringe region required for inflow recycling from the precursor simulation.

is performed at constant tether length under fluctuating tether tension. Consequently, the increase in tether length during the reel-out phase is much more limited and hence the flight path more compact.

For the drag-mode AWE system, the shape of the single-loop flight path barely changes for varying wind speeds. However, the most noticeable difference is the contribution of the on-board turbines at low wind speeds. During the upward flight, the on-board turbines switch to propeller-mode in order to overcome gravity and keep a constant flight speed and tether tension, and hence consume some power.

3.3 LES setup and AWES park layout

The turbulent ABL is modelled according to the procedure introduced in Sect. 2.1. In order to capture all the relevant spatio-temporal scales of the turbulent ABL in the precursor simulations and the wake effects in the AWE park simulations, the flow domain spans over several kilometres and is resolved with high spatial resolution. The dimensions of the simulations domain are $L_x \times L_y \times L_z = 10.0 \times 4.0 \times 1.0 \text{ km}^3$. The domain is discretized into cells of size $\Delta_x \times \Delta_y \times \Delta_z = 10.0 \times 10.0 \times 5.0 \text{ m}^3$, resulting in a grid resolution $N_x \times N_y \times N_z = 1000 \times 400 \times 200$ of up to 80 millions cells for both main and precursor domains.

The mean inflow velocity of main and precursor domains is $U_{\text{ref}} = 10.0 \text{ m/s}$ at 100 m altitude. Note that temporally resolved
630 subsets of the generated precursor simulations are available for download from the Zenodo platform (Haas and Meyers, 2019).

For the utility-scale deployment of their technology, Ampyx Power envisions park power densities in the range of $10 - 25 \text{ MW km}^{-2}$ while targeting a system packing of about $2/L^2$, where L is the maximal tether length (Kruijff and Ruitkamp, 2018). Accordingly, we investigate three different AWE parks configurations with the same packing density, where each park is composed of 25 systems ordered in 5 rows and 5 columns with an equidistant spacing between each system, ie. L in the
635 streamwise directions and $L/2$ in the spanwise direction. The top and side views of the three different AWE park layouts are shown in Fig. 11.

The first AWE park operates with lift-mode AWE systems and the reference layout length is set to $L = 1000 \text{ m}$. This park layout is the densest possible layout to be operated with the designed lift-mode AWE system, such that the allocated areas do not overlap, and will further be referenced as L1 (Lift-mode park 1). The second AWE park operates with drag-mode AWE
640 systems and the same layout as L1 and is referenced as D1 (Drag-mode park 1). These two AWE parks can achieve farm power densities up to 10.0 MW km^{-2} when all systems operate at rated wind speed. The third AWE park also operates with drag-mode AWE systems but with a reference layout length $L = 600 \text{ m}$. This AWE park, referenced as D2 (Drag-mode park 2), corresponds to the densest possible layout for the designed drag-mode AWE system and can achieve a farm power density up to 27.8 MW km^{-2} in rated wind conditions. Note that the flight path constraints in Table 1 ensure a safe operation in accordance
645 with the area allocated to each system in all park configurations. At the initial simulation time, the states of the AWE systems in the parks are initialized to the states values of the pre-computed reference trajectories for $U_D = 10.0 \text{ m/s}$.

The simulations are performed on the high performance computing infrastructure of the Flemish Supercomputer Center (VSC). The computational cost of one LES time step typically largely exceeds the computational cost of one NMPC evaluation. Hence the required computational resources depend heavily on the grid resolution, which also limit the simulation horizon.
650 However, given that AWES dynamics are faster than ABL flow dynamics, the control actions of each AWES are evaluated several times per LES time step. In total, 54000 evaluations per AWES are performed during the simulation horizon of 4500 s. Consequently, the total execution time of the LES time step may depend on the execution time of individual NMPC evaluations. The performance of NMPC evaluations depends on several parameters, such as the length of the prediction horizon or the number of model variables. For drag-mode AWESs on the one hand, the execution time of NMPC evaluations is almost
655 negligible, accounting on average for less than 5% of the execution time of an LES time step. For lift-mode AWESs on the other hand, the execution time of NMPC evaluations can vary substantially. While about 95% of the evaluations are performed in less than 1.0s, similar to drag-mode AWESs, the remaining 5% of the evaluations require about 15–30.0s. This performance drop is generally observed when AWESs operate in heavily-constrained regions of the variable space or transition between considerably different reference flight paths. As a result, the drag-mode AWE park simulations require about 1200 node-hours
660 (or 52 node-days) while the lift-mode AWE park simulation requires about 1600 node-hours (or 67 node-days) on the Tier-2 hardware of VSC.

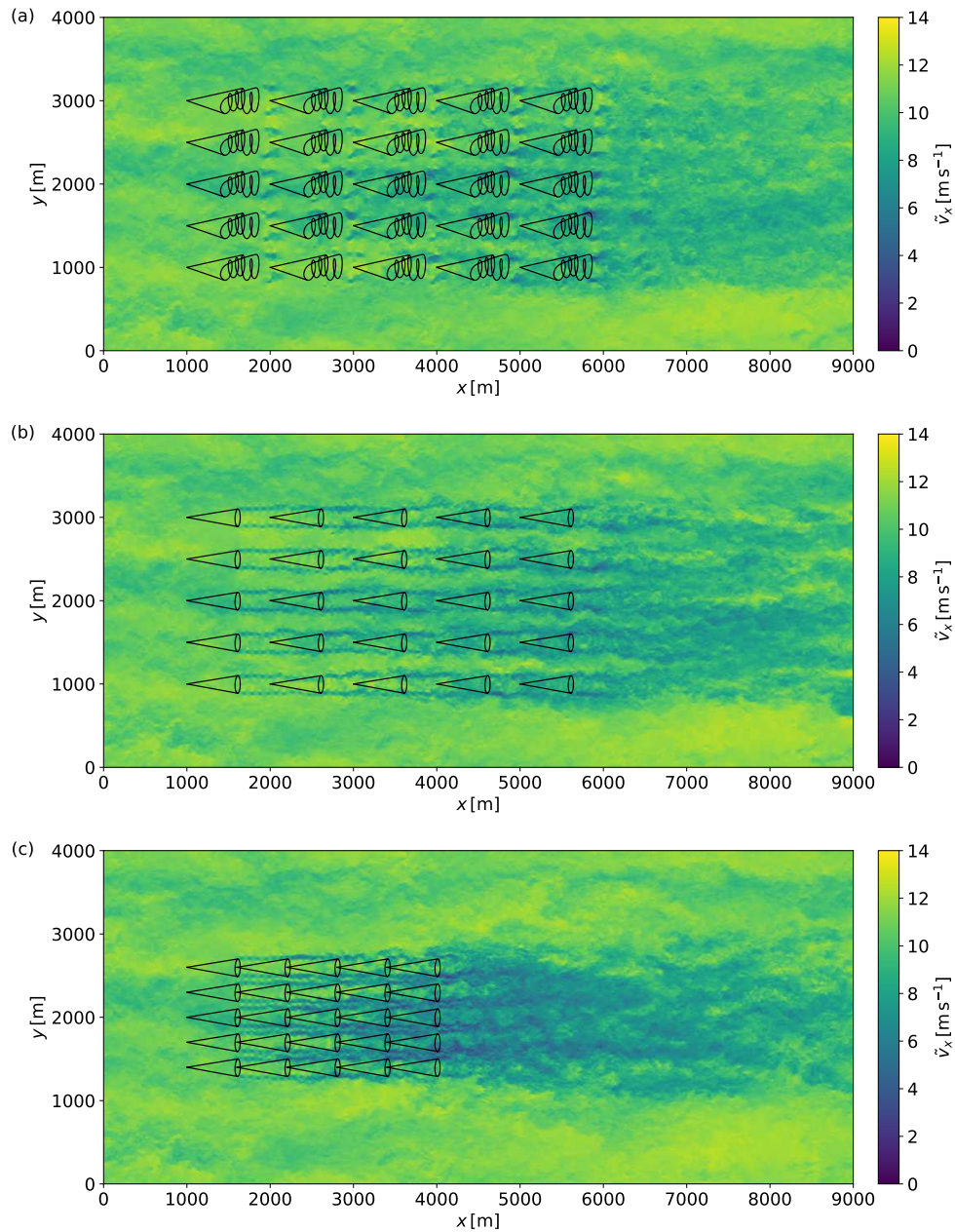


Figure 12. Instantaneous snapshot of streamwise wind velocity \tilde{v}_x through the horizontal xy -plane at a height $z = 200$ m for the AWE parks L1 (a), D1 (b) and D2 (c) at the end of the spin-up phase. The black lines depict the park layout by showing the horizontal footprint of the AWE system trajectories.

4 AWE farm simulation and results

In the following section, we present the main outcomes of the simulations of AWE parks in the turbulent boundary layer. Figure 12 shows instantaneous snapshots of the streamwise wind velocity \tilde{v}_x for the three park configurations investigated in this study. The figure illustrates the complexity of the flow, highlighting large-scale wind speed variations and large wake structures trailing behind individual AWE systems, and how they affect the ABL flow at park level. First, we have a look at the time-averaged characteristics of the ABL flow in Sect. 4.1. Next, we investigate the behaviour of individual AWE systems subject to turbulent wind conditions and how their tracking and power performance are impacted in Sect. 4.2. Last, we discuss the power performance of the complete AWE parks and in particular how wakes impact their efficiency in Sect. 4.3.

To ease the comparison, the trajectories of the AWE systems are parametrized as circular flight path centred around a virtual trajectory center. For the lift-mode system, the diameter of the trajectory is approximately 240 m and its center is located 645 m downstream of the ground station at an altitude of 220 m. Equivalently, for the drag-mode system, the diameter of the trajectory is approximately 200 m and its center is located 610 m downstream of the ground station at an altitude of 190 m.

4.1 Time-averaged ABL flow statistics

4.1.1 Mean ABL flow characteristics

Figure 13 shows time-averaged contours of normalized streamwise velocity deficits and turbulent kinetic energy averaged over one hour of AWE park operation. The wake field develops through the parks as individual wakes add up with the wakes induced by consecutive AWE systems. We observe in the three cases that downstream system rows operate in fully waked conditions. At the last row of the park, the mean velocity deficit, relative to the ABL precursor, reaches about 10% for the lift-mode park (L1), while for the drag-mode parks the velocity deficit increases to about 20% (D1) and up to 30% (D2). In the trail of the annuli swept by the wings, these velocity deficits are further accentuated and can reach up to 20% for the lift-mode AWE systems (L1) and respectively 40% and 50% for the drag-mode AWE systems (D1 and D2). For the drag-mode AWES park with dense layout (D2), the blockage effect of the drag-mode AWE systems also results in an acceleration of the mean flow up to 10% around the park, which cannot be observed for the two AWE parks with moderate layout (L1 and D1).

The mean turbulence intensity TI of the current ABL simulation ranges between 2% and 8% and is about 3% at operation altitude. Hence the power extraction and the wake mixing in the AWE park lead to large increases of TKE levels. The observed TKE levels can reach up the 10 fold of the precursor levels. In particular for lift-mode systems (L1), we observe higher levels of turbulence compared to the same drag-mode configuration (D1), possibly due to the merging effect of individual loop wakes discussed in Sect. 3.2.2. Furthermore, the lift-mode AWE systems sweep over a much larger area than the drag-mode AWE systems. For the latter in layout D1, the lateral extent of the wakes are more limited. Hence, individual columns of drag-mode systems accumulate the effects of their wakes in streamwise corridors, while the wakes spread much farther in the spanwise direction for the lift-mode AWE park (L1). The higher packing density of the second drag-mode AWE park (D2) exhibits the same phenomena as park D1 but with much higher intensity, given the reduced space available for wake recovery.

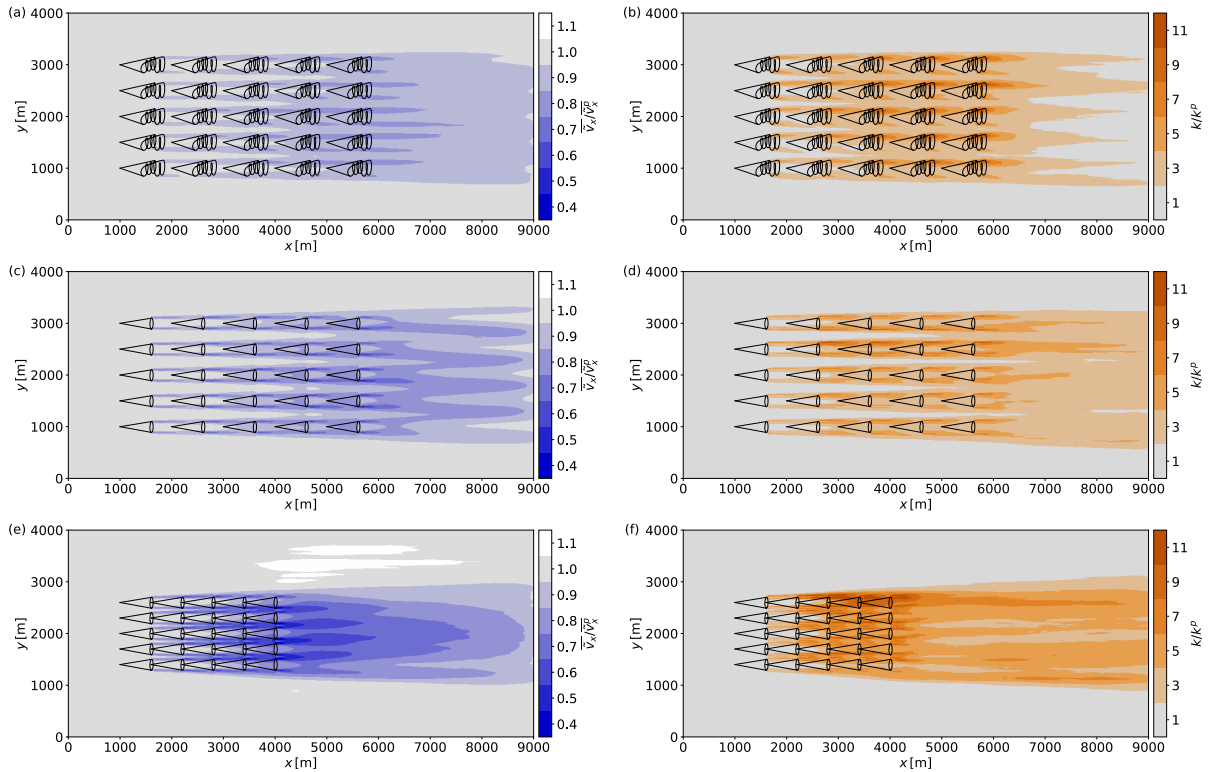


Figure 13. Mean fields of streamwise wind velocity $\overline{v_x}$ and turbulent kinetic energy \overline{k} shown in the horizontal xy -plane at a height $z = 200$ m for the AWE parks L1 (a–b), D1 (c–d) and D2 (e–f). The simulation is averaged over one hour of park operation and normalized by the mean precursor values $\overline{v_x^p}$ and $\overline{k^p}$. The black lines depict the park layout by showing the horizontal footprint of the AWE system trajectories.

4.1.2 Flow characteristics inside the parks

695 We can further deepen the analysis by looking at vertical and horizontal profiles of velocity deficit and turbulent kinetic energy
as shown in Fig. 14. The profiles are shown one diameter upstream of the trajectory center for AWE systems located in the
central column of the parks. For the lift-mode system, the diameter of the trajectory is approximately 240 m and its center is
located 645 m downstream of the ground station at an altitude of 220 m. Equivalently, for the drag-mode system, the diameter
of the trajectory is approximately 200 m and its center is located 610 m downstream of the ground station at an altitude of 190
700 m.

The profiles provide an overview of the local flow distribution experienced by each system in downstream locations of the
AWE column. The profiles confirm the prior observations relative to the downstream development of the wakes through the
park: for the lift-mode AWE park, the wake is much more widespread and therefore induces a weaker velocity deficit. In
contrast, for drag-mode AWE parks, the wake exhibits more localized and stronger velocity deficits, highlighting the annular

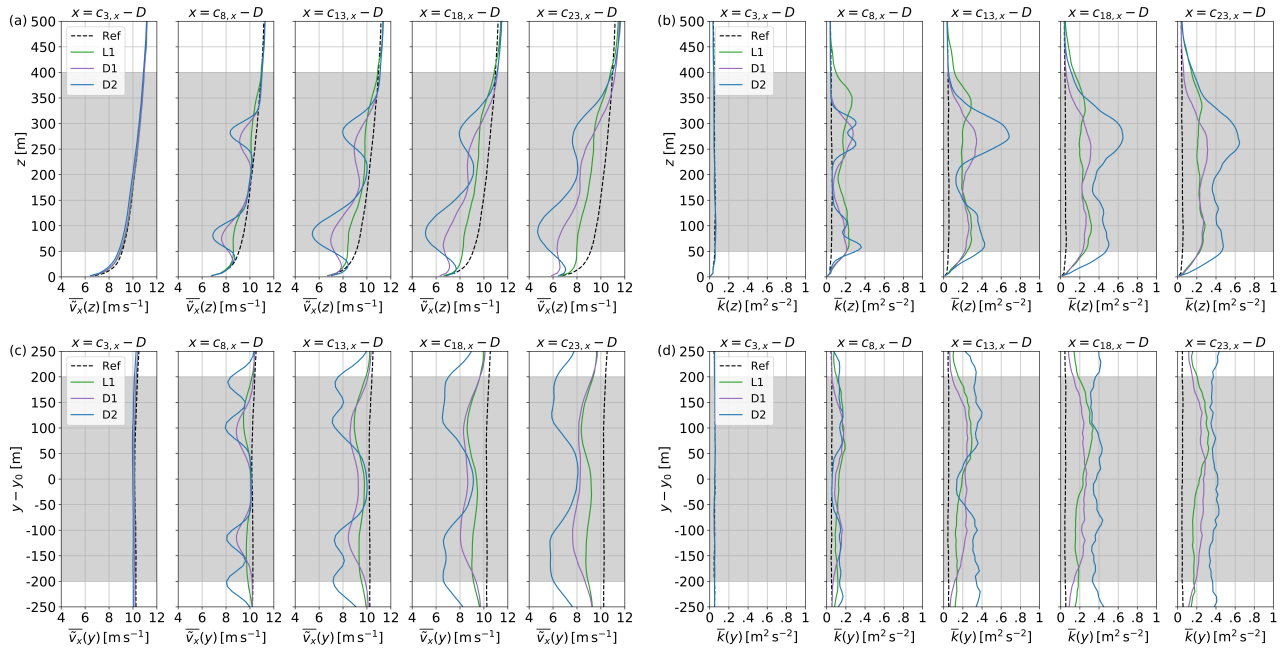


Figure 14. Mean profiles of streamwise wind velocity $\overline{v_x}$ and turbulent kinetic energy \overline{k} through the central park column ($x = 2000$ m) for the AWE parks L1, D1 and D2. The vertical (a–b) and horizontal (c–d) profiles are shown one diameter D upstream of the trajectory center c_i of the 5 AWE systems. The black dashed lines show the precursor reference and the gray-shaded area the operation region of AWE systems.

705 shape of the wake. Each park configuration shows higher velocity deficits at the bottom half of the loops, induced by higher loadings on the wing. In addition, wake recovery in the upper part of the loop is eased by higher turbulence levels.

The wake impacts are much stronger for the drag-mode AWE park (D2) with a higher packing density. The horizontal profiles show that the wake merges with the wakes of neighboring AWES columns as it radius extends laterally the further downstream it progresses. Hence, wakes do not only aggregate as they advect downstream but also merge in the spanwise direction, therefore
 710 resulting in the stronger velocity deficits and higher TKE levels observed for the higher farm power density.

4.2 AWES operation in turbulent boundary layer

AWES systems operate in very different wind conditions depending on the operation mode, the park layout and their own position within the park as seen in the previous section, Sect. 4.1. In this section, we discuss how these parameters affect the operation of the systems, in particular how they adapt their respective trajectories and how accurately the NMPC controller can
 715 track their flight path.

Figure 15 shows the reference wind speed of the trajectories tracked by the AWE systems as directed by the supervision level of the controller. Each reference trajectory is tracked for the duration of respectively one cycle for lift-mode systems (≈ 65 s) and five cycles for drag-mode systems (≈ 50 s) before it is updated by the controller based on the averaged velocity sampled by

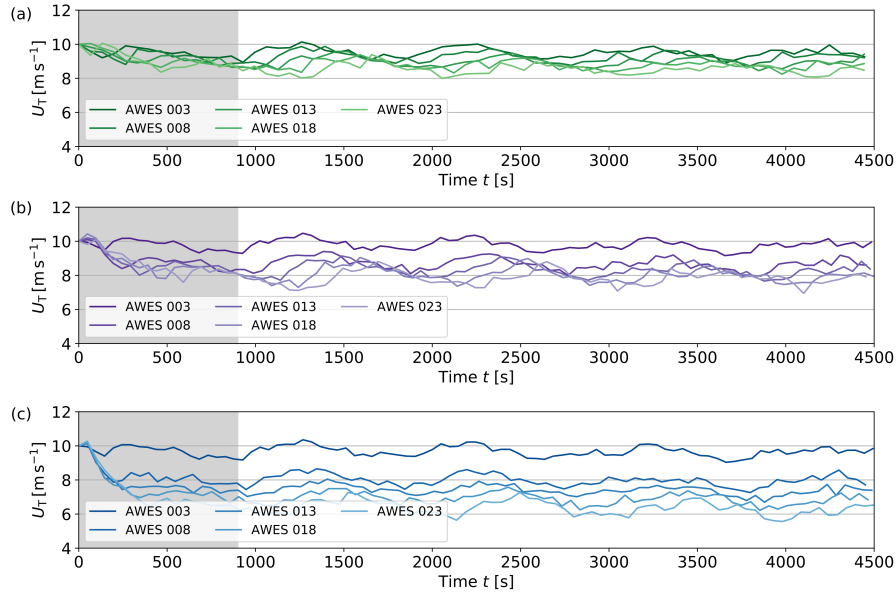


Figure 15. Time series of reference wind speed tracked by the 5 AWE systems of the central park column ($x = 2000$ m) for the AWE parks L1 (a), D1 (b) and D2 (c). The gray-shaded area covers the spin-up phase of the park simulations.

the wind speed estimator over that time period. In particular, we show the tracking behaviour of the five rows of AWE systems
 720 of the central column of the three park configurations.

At the start-up of the operation, each system experiences similar conditions from the unperturbed ABL flow. As systems begin to harvest power and induce their own wakes, upstream wakes travel downstream and start to impact the operation of downstream rows until the complete park operates in fully waked conditions at the end of the spin-up phase at $t = 900$ s. The variations of the tracked value for the front row AWE system (AWES 003) are due to the inherent unsteadiness of the ABL
 725 flow. We observe how these large-scale wind fluctuations experienced at the front row propagate with some delay through the downstream rows of the park. However, the large decreases of tracked speed for the downstream systems are due to the effects of upstream wakes. As discussed above, drag-mode AWE systems experience much stronger wakes and hence track lower wind speeds than lift-mode AWE systems. In particular, a larger decrease is observed from the front row to the second row.

Note that the amplitude of the large-scale variations of the ABL vary from one column to another. Consequently, the different
 730 columns of the parks do not operate similarly and impose a different forcing on the ABL flow field. This effect can explain the asymmetry observed in the time-averaged quantities shown in Fig. 13. In particular, the averaging period of one hour may not be sufficient to entirely smooth out these temporal and spatial variations across the entire AWE farms.

We can further look at the instantaneous streamwise wind speed measured in-flight at the wing as shown in Fig. 16 for two systems located in the front and back rows. Despite the ambient turbulence of the ABL flow, the wind speed monitored by
 735 the front-row systems coincides quite well with the reference wind speed distribution of the tracked trajectories. However for

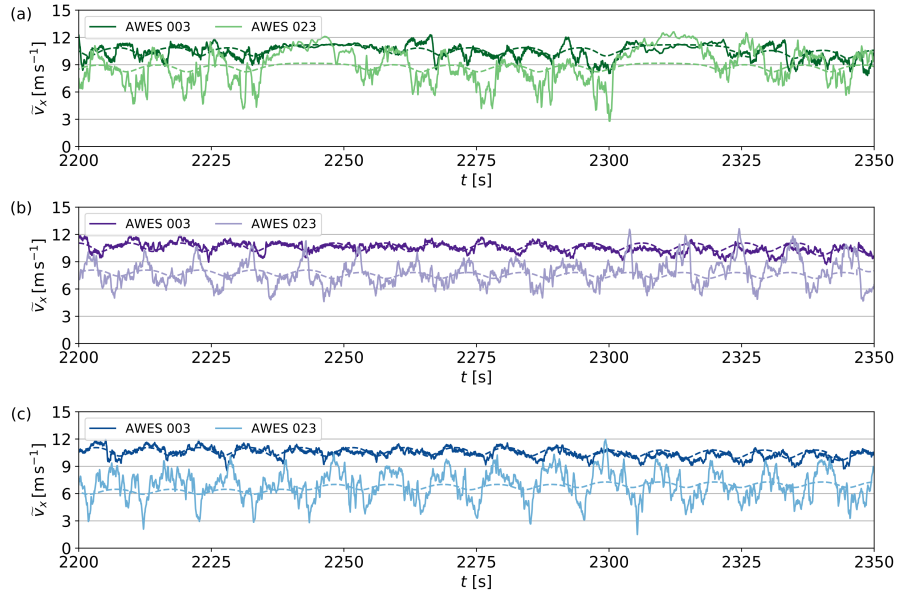


Figure 16. Time series of streamwise wind speed \tilde{v}_x monitored by the front and rear AWE systems of the central park column ($x = 2000$ m) for the AWE parks L1 (a), D1 (b) and D2 (c). The coloured dashed lines show the reference quantities of the tracked trajectories.

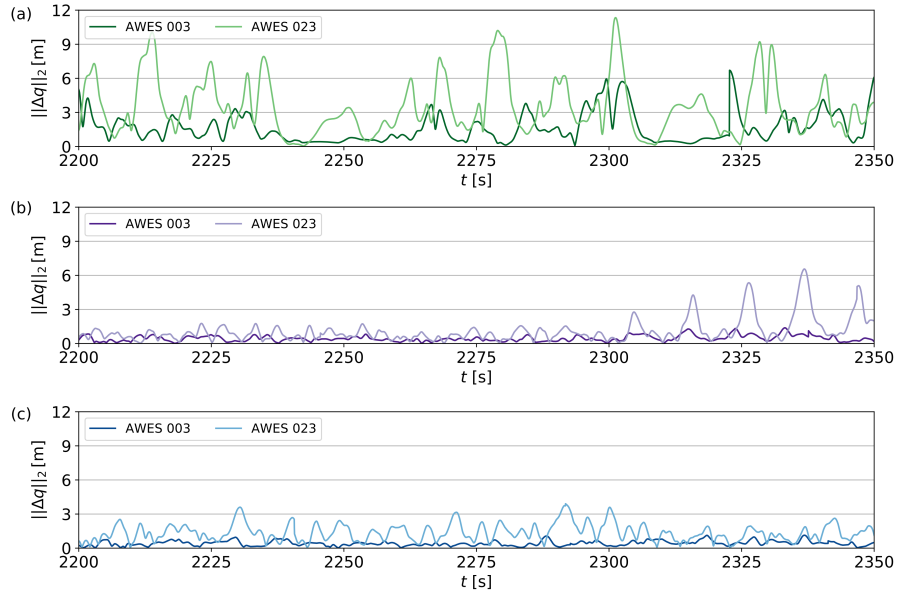


Figure 17. Time series of position offset $\|q - q^r\|_2$ monitored by the front and rear AWE systems of the central park column ($x = 2000$ m) for the AWE parks L1 (a), D1 (b) and D2 (c).

the lift-mode system, we observe additional, sharp fluctuations resulting in abrupt increases and decreases of the monitored streamwise wind speed. These effects are amplified as the system progresses further in the reel-out phase, as seen in the time window $t \in [2200\text{s}, 2350\text{s}]$. This indicates that the wing may still interact with its own wake in some sections of the flight path. In order to ensure a reliable operation, the reel-out speed limitation was lifted off for flight path tracking to allow a better reactivity of the systems to the unsteady wind conditions. Hence, the systems can achieve higher reel-out speeds than the reference.

The strong velocity deficits and the higher levels of TKE observed in the back rows of the parks greatly impact the instantaneous wind speed monitored. We observe a much larger range of fluctuations for AWE systems located in the last row than in the first row. The effects described for the front row lift-mode system are accentuated for the back row system, suggesting the presence of compact wake regions from upstream systems advecting through the park.

The unsteady wind conditions also impact the tracking accuracy of the NMPC controller. Figure 17 shows the position offset of the systems relative to the tracked flight. For the drag-mode systems operating in the front row of parks D1 and D2, the tracking error is almost negligible. This error increases for the systems in the back row as they experience larger wind speed fluctuations. For the lift-mode park L1, we observe larger position tracking error, partly due to the additional degree of freedom related to the reel-out and reel-in of the tether. The highest offsets occur however after the AWE system flies through a low wind speed region. Nevertheless, the error remains marginal compared to the dimensions of the flight path, as it rarely exceeds 12 m. Hence, the NMPC algorithm tends to always react reliably to the wind speed fluctuations and steers the system back onto its reference flight path.

4.3 Power performance at system and park level

The unsteady wind conditions not only affect the tracking behaviour of each AWE system but also impact their performance. Figures 18 and 19 respectively show the tether tension and mechanical power of the front and back row systems in the central column of the parks. For the lift-mode systems, the low-speed regions crossed by the wing generally lead to a drop of the tether tension that requires to be compensated by steering manoeuvres. These tether tension variations negatively impact the amount of generated mechanical power such that we observe power losses of about 10% to 15% relative to the reference power of the tracked trajectories. For the two drag-mode park configurations, the wind fluctuations barely impact the operation of the systems and we observe a good tracking of the power generation profiles. In the back row however, the tracked flight path and the low wind speed available require the on-board turbines to operate as propellers in order to overcome gravity while flying upward. Hence, some drag-mode systems end up also consuming some of the harvested power. Note that the tether tension maxima monitored at each system match the relaxed upper bound used for flight path tracking as discussed in Sect. 2.4.

We further address the power extraction process from the perspective of the complete AWE park, and in particular from the system location in the park. Figure 20 shows the mean power generation of each row relative to the reference power of the tracked trajectories for the three different park configurations. In this way we can quantify the power losses due to local wind speed fluctuations and the steering efforts they cause. For the lift-mode park, every system across each row is only capable to harvest a fraction of the tracked power. While in the front row up to 91% of the tracked power can be harvested, the efficiency

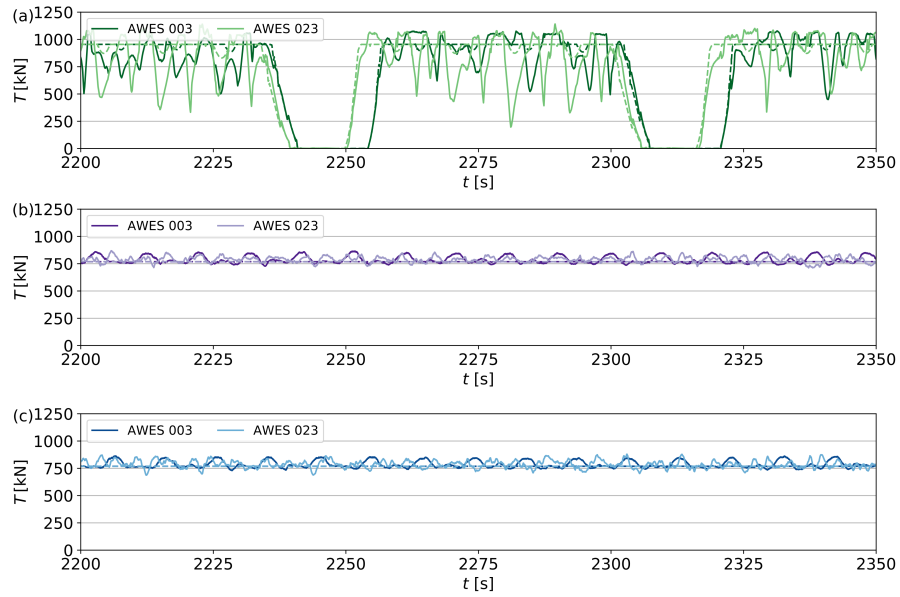


Figure 18. Time series of tether tension T_T monitored by the front and rear AWE systems of the central park column ($x = 2000$ m) for the AWE parks L1 (a), D1 (b) and D2 (c). The coloured dashed lines show the reference quantities of the tracked trajectories.

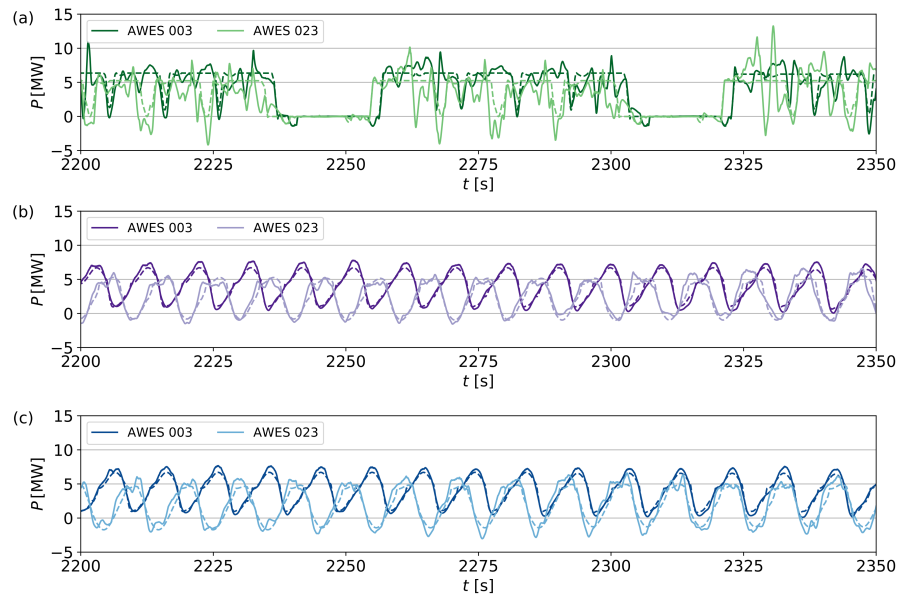


Figure 19. Time series of mechanical power P monitored by the front and rear AWE systems of the central park column ($x = 2000$ m) for the AWE parks L1 (a), D1 (b) and D2 (c). The coloured dashed lines show the reference quantities of the tracked trajectories.

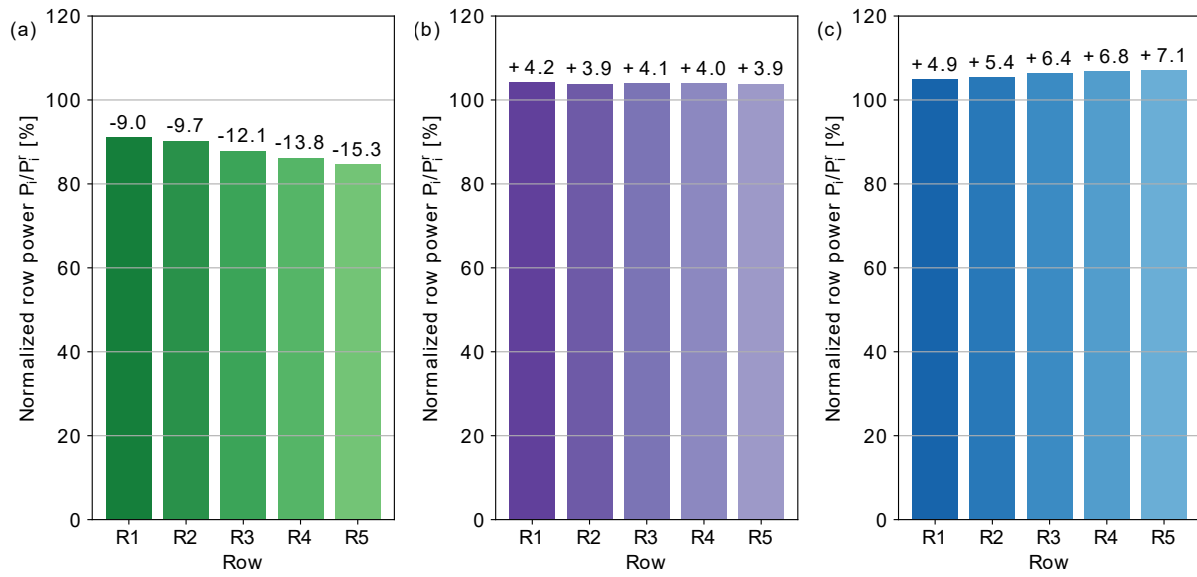


Figure 20. Mean row power averaged over one hour of park operation and normalized by tracked reference power \bar{P}_i/\bar{P}_i^r for the AWE parks L1 (a), D1 (b) and D2 (c).

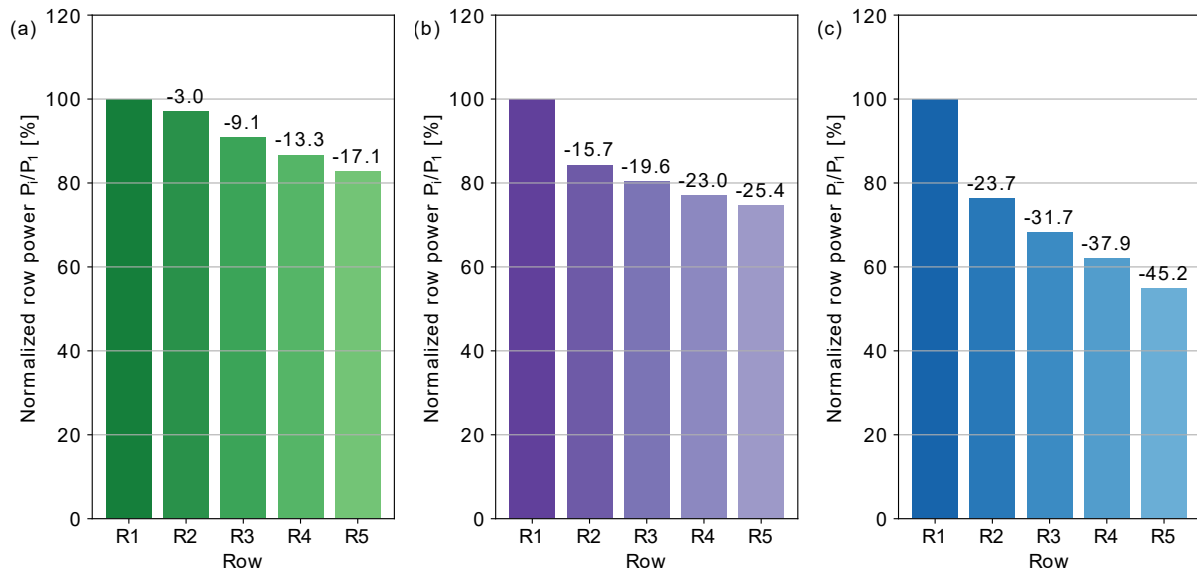


Figure 21. Mean row power averaged over one hour of park operation and normalized by front row value \bar{P}_i/\bar{P}_1 for the AWE parks L1 (a), D1 (b) and D2 (c).

770 of the power tracking decreases gradually for the downstream rows, such that approximately 85% of the tracked power can be harvested in the last row. For the drag-mode AWE parks, individual systems are able to harvest more power from the wind than expected. For the drag-mode park D1, each row harvest on average about 4% more power. With the denser layout (D2), the systems in the front row harvest 5% more power while this increases to up to 7% in the last row. This suggests that the supervision level underestimates the local wind conditions experienced by the systems.

775 Figure 21 shows the mean power generation of each row relative to the front row of the farm. This allows to quantify the wake-induced power losses for the three different park configurations. For the lift-mode AWE park the relative power decrease through the farm, ie. the power deficit between front row and downstream rows reaches up to approximately 17%. For the drag-mode AWE parks, the wake losses are much more important and reach approximately 25% in the last row of AWE park D1 and up to 45% for the AWE park with denser layout D2. While for the lift-mode AWE park the power decrease across the
780 subsequent rows is progressive, for drag-mode AWE parks, the power losses increase abruptly between the first and second row. This drop account for about 62% and 52% of the row losses for the park configurations D1 and D2, respectively.

5 Conclusions

In this study we have investigated the wake interaction and power extraction for large parks of utility-scale AWE systems. Flight path tracking by means of model predictive control (MPC) has proven to be a robust control strategy for both lift- and
785 drag-mode systems when operating in turbulent wind conditions: The path tracking results in position offsets generally up to 12 m, while satisfying the set variable bounds and tracking quite accurately the power profiles, in particular in drag mode. Lift-mode AWE systems encounter however important fluctuations in local wind speeds during operation, which can lead to temporary large decreases of tether tension and significant reductions of instantaneous power. First, we have observed that lift-mode systems can interact with their own wake: During reel-out, the wing can fly (partially) through or in the direct vicinity
790 of the wake induced in the previous power-generating loops. Hence, the interaction with its own wake needs to be considered already during the design phase: When generating optimal reference trajectories, it is crucial to define reeling strategies that avoid these situations and incorporate induction phenomena in the modelling procedure. This is an active topic in current AWE research. Second, these large wind speed fluctuations can be associated to the characteristic wakes induced by lift-mode AWE systems: While the flow forcing is negligible during the retraction phase, the wakes induced during consecutive loops of the
795 power-generation phase tend to merge into a single wake structure. This interaction leads to compact, low-speed flow regions which get advected downstream with the mean flow and negatively impact the operation of downstream systems.

Moreover we showed that for the three investigated configurations, wake effects and wake-induced losses in utility-scale AWE parks are significant. The induced wakes display very characteristic annular shapes, however the strength and the width of the wakes highly depends on the operation mode and the park layout. In terms of park performance, we observed wake-
800 induced performance losses of up to approximately 15% in the last row for lift-mode AWE park. For the two drag-mode AWE parks with moderate and dense farm power densities, the wake-induced power losses increase up to 25% and 45% respectively in the last row of the parks. Hence, the layout of the farm also plays a considerable role in the performance of the

park. However, note that wake losses and tracking losses/gains can not completely be isolated from each other: Improving the tracking behaviour of lift-mode systems by limiting the large tension fluctuations in the tether would result in a stronger axial flow induction, hence leading to larger wake losses and vice versa.

The current predictions formulated in this study can be refined by increasing the resolution of the LES flow domain. With a higher grid resolution, the representation of the individual AWE systems can be enhanced, limiting their forcing effects to the direct vicinity of the wing instead of large sectors. The estimation of the aerodynamic quantities along the wingspan of the aircraft would also benefit from higher resolutions as a larger range of turbulent motions is resolved, hence increasing the modelling accuracy of the wing behaviour. However, increasing the grid resolution is not the only approach to improve the accuracy of the framework. The fully-coupled computational framework integrates numerous building blocks into a single simulation platform with a high level of complexity. The overall fidelity of the simulations can however be improved in the future by increasing the complexity of individual components of the framework and addressing the following known limitations: First, we can improve the modelling of the atmospheric boundary layer. The description of the ABL flow can be enhanced by including Coriolis forces and thermal effects into the LES framework (Allaerts and Meyers, 2015). The inclusion of these effects modify significantly the structure of the flow, in particular capturing the inversion layer separating the turbulent boundary layer from the free atmosphere above. The height of the inversion layer, the strength of wind veer in the boundary layer, or the occurrence of low-level jets, will certainly affect the flight path characteristics of AWE systems, such as optimal heights and tether length. These effects will further impact the controllability and power performance of the systems and hence require further investigations. Second, the complex dynamics of AWE systems can be better characterized by more detailed models. One possible alternative to the point-mass model is the 6DOF rigid-wing model (Malz et al., 2019). This model includes the rotational dynamics of the complete systems, hence removing the need for a states based assumption of the wing orientation and further providing a more accurate prediction of the flight manoeuvres. In addition, this model includes realistic control capabilities by steering the aircraft using the deflection of control surfaces such as ailerons, elevators and rudder. Third, the modelling of the tethered aircraft can further be improved by incorporating unsteady aerodynamics. Fast pitching manoeuvres of the wing and sharp turns of the aircraft can have considerable effects on the local aerodynamic characteristics of the wing sections and hence have a significant influence upon the resulting aerodynamic forces of the system. Additionally, the aero-elastic response of the aircraft to the unsteady loading should be considered in order to prevent fatigue of the structure. Although the rigid-rod assumption performs well for the high-tension power generation phases (Malz et al., 2019), this model lacks to capture the tether dynamics. The incorporation of tether sag (Trevisi et al., 2020) would benefit the completeness of the modelling effort.

In terms of tracking performance, the improved system modelling should help reduce the mismatch between model and virtual plant such that an enhanced NMPC algorithm could accurately track the flight path while considering the integrated lifting-line forces to compute the AWES dynamics. Also, in order to further improve the closed-loop performance of the systems in terms of power output, one can consider applying approximate or exact economic NMPC formulations instead of the pure flight path tracking scheme used in this study.

Finally, the wake profiles show quite large deviations from the logarithmic mean flow distribution assumed by the high-level controller. Therefore in the future, we can implement supervision strategies that take the wake shape into consideration and make use of the inherent flexibility and adaptability of AWE systems: We can further use the wake profiles to generate new optimal flight trajectories in which individual systems adapt the elevation and azimuthal angles of operation to eventually avoid the upstream wakes.

To conclude, this study demonstrates the considerable interaction between large-scale AWE systems and the atmospheric boundary layer for the considered park configurations and motivates further investigations to achieve an efficient operation of utility-scale AWE parks.

845 *Code and data availability.* The SP-Wind flow solver is a proprietary software of KU Leuven while the toolbox `awebox` is openly accessible on Github (awebox, 2021). Time-resolved three-dimensional subsets of the ABL precursor simulations are openly accessible from the **AWESCO Wind Field Datasets** (DOI: 10.5281/zenodo.1418676) (Haas and Meyers, 2019). Virtual flight data of the AWE systems for the three AWES park configurations are presented in Appendix B and are openly accessible from the dataset **Large-eddy simulation of airborne wind energy farms: AWES virtual flight data** (DOI: 10.5281/zenodo.5705563) (Haas and Meyers, 2021).

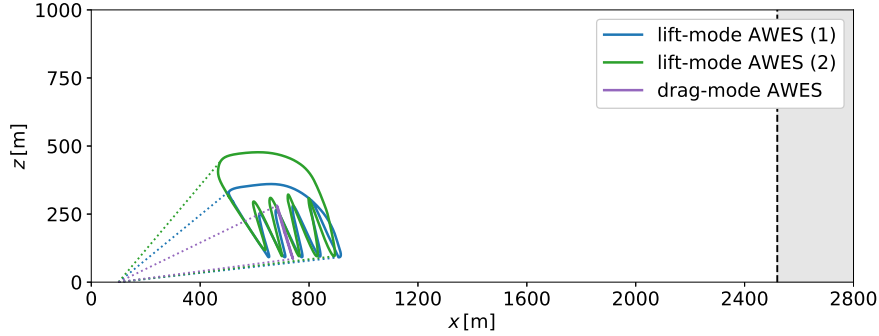


Figure A1. Side view of the computational setup of the single-system simulations used for the analysis of lift- and drag-mode AWE systems.

Table A1. Resolution of the computation domain $L_x \times L_y \times L_z = 2800 \times 1000 \times 1000 [\text{m}^3]$ with fine, medium and coarse grids for the analysis of single AWE systems.

Grid	N_x	N_y	N_z	Δ_x	Δ_y	Δ_z	Δt
Fine	700	250	500	4.0	2.0	2.0	0.10
Medium	448	160	320	6.25	6.25	3.125	0.16
Coarse	280	100	200	10.0	10.0	5.0	0.25

850 Appendix A: Investigation of single-AWES wake characteristics

Ahead of the investigation of utility-scale AWE parks, we have conducted a series of single-AWES analysis in order to assess the computational setup used in this study. In this appendix, we address in particular the tuning of the actuator parameters in Sect. A1, the detailed analysis of wake structure by means of high-resolution simulation in Sect. A2, the grid-dependency of wake characteristics in Sect. A3, and finally the convergence of the supervision level of the controller in Sect. A4.

855 Figure A1 shows the computational setup used in this study of both lift- and drag-mode AWE systems. The domain dimensions are $L_x \times L_y \times L_z = 2800 \times 1000 \times 1000 [\text{m}^3]$. We use three different resolutions to discretize the flow domain as specified in Table A1. The AWE systems operate in a sheared inflow without ambient turbulence parametrized by a logarithmic profile given in Eq. (27), where $U_{\text{ref}} = 10.0 \text{ m/s}$.

A1 Tuning of actuator parameters

860 The dependency of the actuator line and actuator sector methods to their (temporal) parameters is investigated for the simulation of a single drag-mode AWE system. The system operates at a reference trajectory $U_D = U_{\text{ref}} = 10.0 \text{ ms}^{-1}$ and the flow domain is discretized using the finest grid resolution with cell size $\Delta = 4.0 \times 4.0 \times 2.0 \text{ m}^3$. The filter width of the Gaussian filter is uniform in all three spatial directions and is set for all actuator methods to $\Delta_f = 2\Delta_x$ following the recommendations in Troldborg et al. (2010).

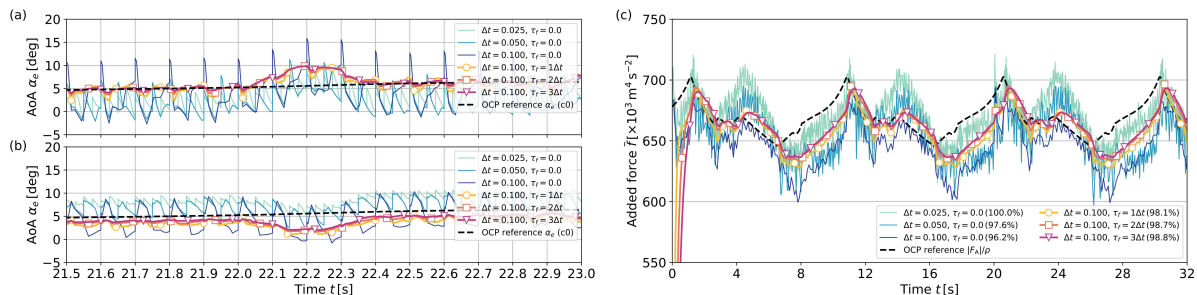


Figure A2. Instantaneous angle-of-attack monitored at the wing tip section on the port (a) and starboard (b) sides. (c) Magnitude of the specific forces \bar{f} added to the flow field at the fourth stage of the LES Runge-Kutta scheme by means of actuator methods for different sets of parameters. Three ALM simulations are performed with different LES time steps and three ASM simulations are performed with three different time filter constants. The black dashed lines show the OCP references.

865 The chosen grid resolution requires a minimal simulation time step $\Delta t = 0.1$ s. Accordingly, we test three ALM simulations with LES time steps of respectively $\Delta t = 0.1$ s, $\Delta t = 0.05$ s and $\Delta t = 0.025$ s and three ASM simulations with time step $\Delta t = 0.1$ s and filter constants $\tau_f = 1\Delta t$, $\tau_f = 2\Delta t$ and $\tau_f = 3\Delta t$, respectively. The states of the AWE system are interpolated from the OCP reference and the local aerodynamic quantities of each wing section are computed using the lifting-line method presented in Sect. 2.2.2.

870 Figure A2 shows time series of the angle-of-attack, measured at the wing tip sections, and of the specific aerodynamics forces added onto the flow. The ALM simulations exhibit large fluctuations of the added forces due to the varying flow conditions experienced by the wing. Within one LES time step, the local flow conditions monitored by individual wing section varies greatly due to the very localized effects of the ALM forces. The ASM simulations, on the other hand, weight the individual force contributions at discrete AWES time steps, hence resulting in smoother force distribution, while introducing a slight time
875 delay, but also smoother variations of angle of attack in time given the low velocity gradients encountered due to the wider smearing of the forces onto the LES domain. The forces of the optimized reference trajectory using the point-mass model are shown for comparison: Over the period of one full periodic cycle, the model mismatch between the forces computed with actuator methods and the reference OCP forces is less than 4%.

Given the high flight speed of the system, the wing navigates through several grid cells during one time step for the simula-
880 tions with $\Delta t = 0.1$ s and $\Delta t = 0.05$ s. Therefore, the ALM requires the smallest time step, $\Delta t = 0.025$, to ensure a smooth transition as the wing sweeps across the flow domain. This results however in a fourfold increase of the computational effort. The ALM simulation with $\Delta t = 0.025$ hence serves as reference simulation. The ASM technique can be applied to simulations with $\Delta t = 0.1$ and allows to approximately reproduce the unsteady forcing of the reference ALM with an error less than 2%. Increasing the value of the time filter constant τ_f tends to reduce the error but also increases the computational cost. Hence, in
885 order to keep a reasonable computational cost and achieve a sufficient accuracy, we perform further AWE simulations with the ASM techniques using $\tau_f = 2\Delta t$.

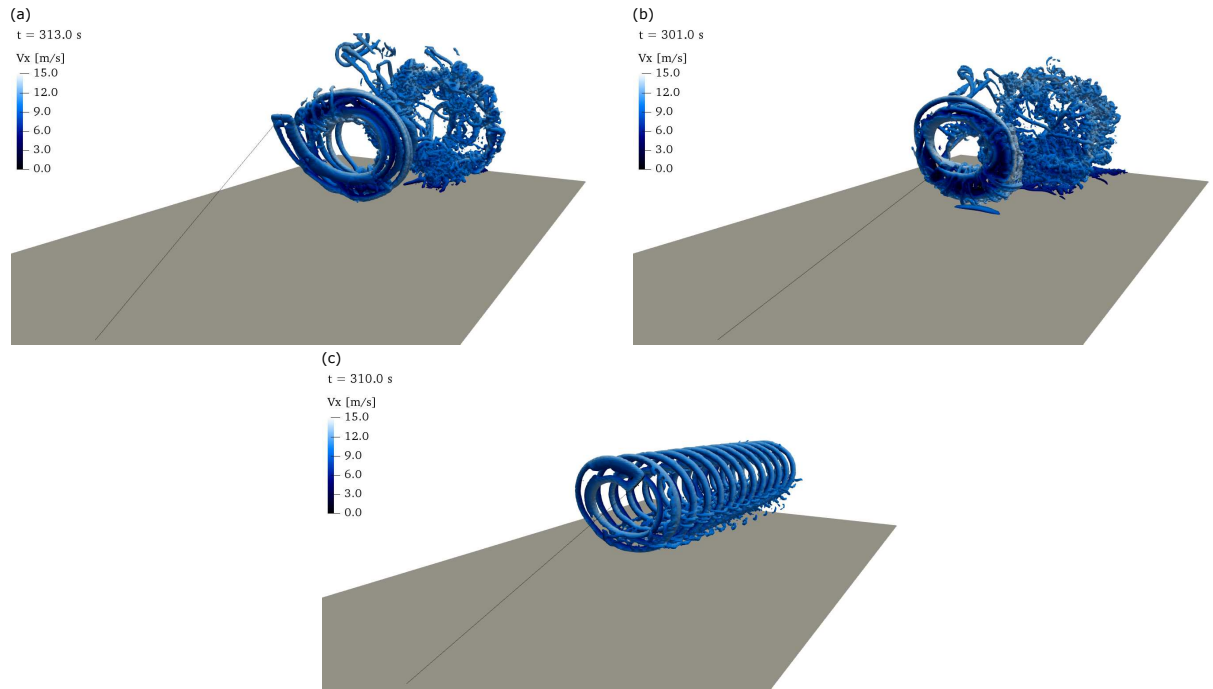


Figure A3. Instantaneous frontal snapshots of the wake field of reference lift- and drag-mode AWE systems operating in an unperturbed logarithmic inflow at a wind speed $U_D = 10 \text{ m s}^{-1}$. Isovolumes of positive Q-criterion, colored by streamwise velocity \tilde{v}_x for (a) lift-mode AWE system with induction-based limitation of reel-out speed at $t = 313 \text{ s}$, (b) lift-mode AWE system with original bounds at $t = 301 \text{ s}$, and (c) drag-mode AWE system at $t = 310 \text{ s}$.

A2 High-resolution simulations of single AWESs

We can extend the previous high-resolution simulations of a single drag-mode AWE systems to lift-mode AWE systems in order to investigate the structure of the wake flow and loads acting onto the wing.

890 Figure A3 shows the structure of the wake flow for each AWE system simulated with ASM on the fine grid by visualizing positive levels of Q-criterion (Jeong and Hussain, 1995). For the drag-mode AWE system, tip vortices emanate continuously from the wing tips and are transported downstream in a coherent manner by the background flow. For the lift-mode AWE systems, the wing tip vortices generated during the individual loops start to interact with each other in the wake and eventually merge into a more significant single structure, which eventually breaks down further downstream due to the effect of mixing.

895 The pumping behaviour of the lift-mode systems is also clearly visible: during the retraction phase, the aircraft takes a different path while being subject to a much smaller wing loading, hence interrupting the wake generation for a short amount of time. The grid resolution and the actuator settings enable to resolve individual flow structures, and provide interesting insights in the complex characteristics of the wake flow of single AWE systems.

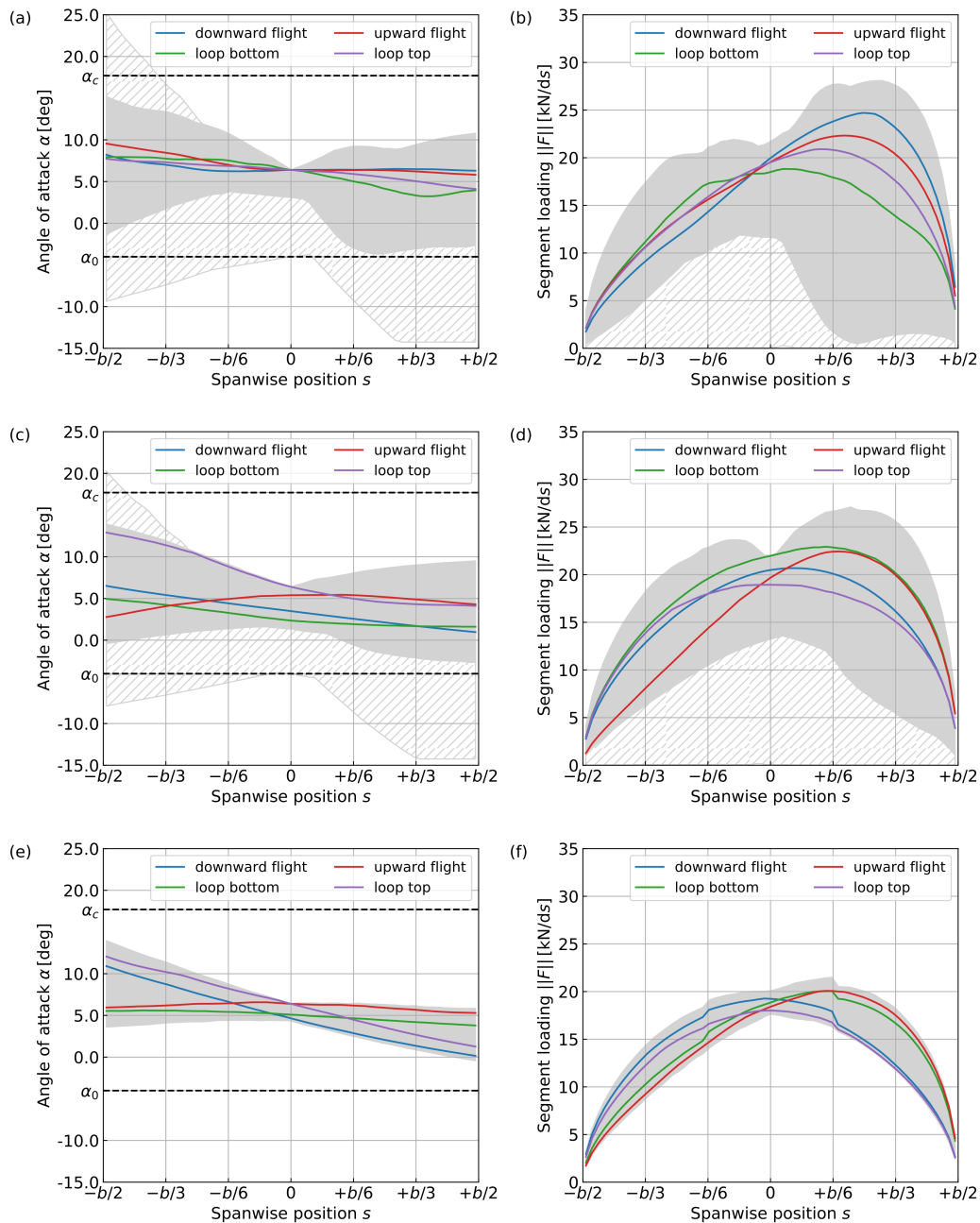


Figure A4. Distributions of angle of attack and wing loading along the wingspan of (a–b) the lift-mode AWE system with original bounds, (c–d) the lift-mode AWE system with induction-based limitation of reel-out speed, and (e–f) the drag-mode AWE system. The coloured lines show the distributions at selected stages of the trajectories. The gray shaded areas show the value range during power generation while the hashed areas only show the reel-in phase.

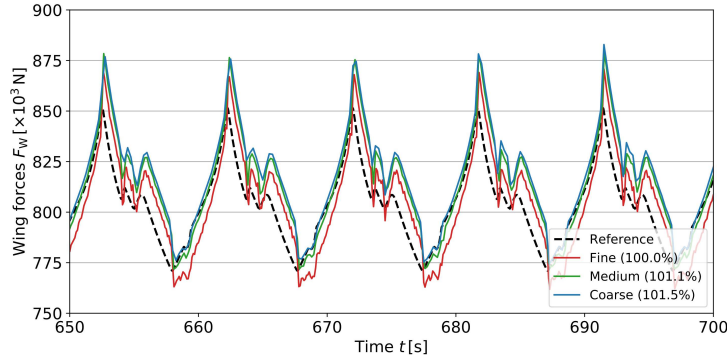


Figure A5. Time series of integrated wing forces acting on the drag-mode AWE system for three different grid resolutions. The black dashed lines show the OCP reference.

Figure A4 shows the spanwise distribution of angle of attack and wing loading for the three different systems. During power
 900 generation, the angle of attack is kept below the critical angle of attack. For the lift-mode AWE systems, the wing tips stall
 briefly during the turn manoeuvre initiating the reel-in phase. This effect is reduced when using the induction-based limitation
 of the reel-out speed and lasts less than 1 s without modifying significantly the total aerodynamic force acting on the wing. The
 force distribution along the wingspan is not elliptically distributed, as opposed to the assumptions of the point-mass model: The
 starboard side of the wing, the wing half flying at the outer side of the flight path, experiences a stronger wing loading than the
 905 port side due to the wing angular velocity, in particular during upward flight. For the drag-mode AWE system, the additional
 loading of the on-board turbines modifies only slightly the spanwise load distribution of the wing, in particular during the
 downward path of the loop.

A3 Analysis of grid dependency

Next, we perform the simulation of the single drag-mode AWES and assess the time-averaged flow quantities using the
 910 three grid resolutions specified in Table A1. In this grid analysis, the ratio of filter width to grid size is kept constant, hence
 $\Delta_f/\Delta_x = 2$. The simulation with the fine grid, which captures explicitly the individual tip vortices during the reel-out phase
 of lift-mode AWE systems, is considered the reference simulation.

Figure A5 shows time series of the aerodynamic wing forces integrated over its wingspan acting on the drag-mode AWE
 system for the three grid resolutions. The decrease in grid resolution comes with a simultaneous increase of the simulation time
 915 step, hence drastically reducing the computational expense of the simulations. This comes however at the cost that the larger
 spatial filtering and temporal smoothing result in a much wider sector, representing the wing more as blunt body in the LES
 domain. The widespread of the added forces in turn reduces the accuracy of the local aerodynamic quantities of each wing
 section compared to the reference simulation. Nevertheless, the integrated forces overestimate the reference by less than 2%

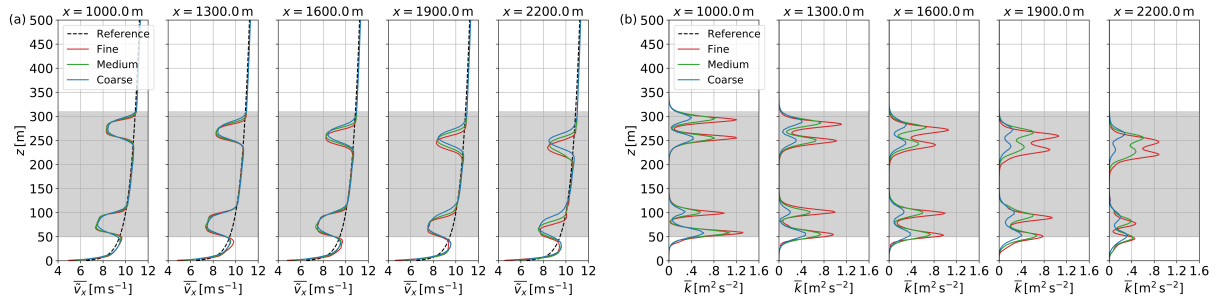


Figure A6. Time-averaged vertical profiles of streamwise wind velocity $\overline{v_x}$ (a) and turbulent kinetic energy \overline{k} (b) at several locations downstream in the wake of the AWE system for three different grid resolutions. The black dashed lines show the inflow velocity profiles and the gray-shaded area represent the operation region of AWE systems.

such that lower grid resolution can still sufficiently capture the resulting aerodynamic forces in order to accurately compute the
 920 AWES dynamics.

Figure A6 shows time-averaged profiles of axial flow velocity and turbulent kinetic energy at different locations in the wake of the drag-mode AWE system for three different grid resolution. The velocity profiles show that all resolutions can capture the general annular shape of the wake and its strength up to 1200 m behind the system. This good agreement allows us to use the coarse grid resolution for the AWE park simulations, where the downstream spacing between two rows of AWE systems
 925 does not exceed 1000 m, and which would be too computationally expensive to perform on the finer resolutions. In terms of resolved turbulent kinetic energy, the medium and coarse grid cannot capture the same levels of turbulence as the fine grid. This is however less crucial given that in the fully turbulent ABL simulations, ambient turbulence triggers wake breakdown and turbulent mixing earlier than in the turbulence-free, sheared inflow investigated here. While for the coarser resolution it cannot be assured that lift-mode AWE systems, even with the induction-based reel-out speed limitation, won't interact with
 930 their own wakes, this effect will be weakened given that the force smearing also reduces the strength of the tip vortices.

A4 Convergence of supervision level

Finally we can also verify the convergence of the supervision level of the controller and assess the different reel-out strategies employed for the lift-mode systems. Figure A7 shows the tracking profiles of the three AWE systems by visualizing the time-averaged wind speed values sampled by the controller and the associated reference velocity of the tracked trajectories. All
 935 systems show good convergence towards an asymptotic value between 9 m/s and 10 m/s. As discussed in Sect. 3.2.2, lift-mode AWE systems may interact with their own wakes, therefore we have used two different reel-out strategies. Figure A7 shows that the induction-based reel-out strategy used by lift-mode system (1) allows to track higher wind speed references, showing that the wing experiences less interaction with its wake. Therefore, this strategy also allows to operate the system along trajectories generating more power, and hence increases the performance of the AWE park.

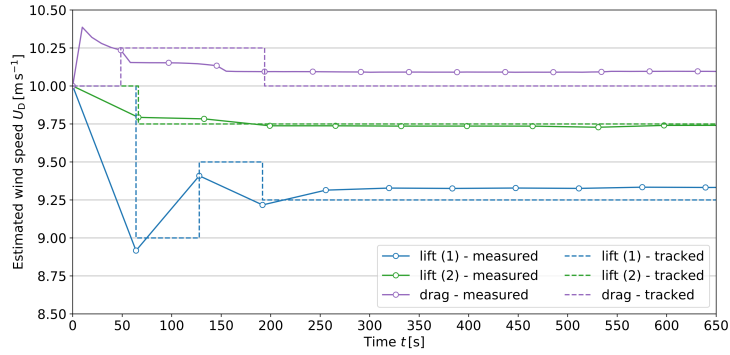


Figure A7. Convergence of the controller supervision level for the three types of AWE systems investigated. The markers display the time-averaged wind speed value sampled during one (lift mode) and respectively five (drag mode) periodic cycles and the dashed lines show the associated reference wind speed of the tracked trajectories in increments of 0.25 m/s.

940 Appendix B: Data accessibility

The virtual flight data of each individual AWE system, including all states and controls, are monitored for the different AWE park simulations. The monitored flight data, the tracking scheme of each AWE system, and the tracked reference trajectories of the AWE systems, are openly available on the research data repository Zenodo from the dataset **Large-eddy simulations of airborne wind energy farms: AWES virtual flight data** (DOI: 10.5281/zenodo.5705563). The different files are organized as Python dictionaries and are stored as pickle objects. Python 3 scripts are provided to handle the files and visualize the data.

The reference trajectories are optimized for the lift- and drag-mode AWE systems presented in Sect. 3.2.1 for the wind speed range $U_{\text{ref}} \in [5.0, 12.0]$ with increment of 0.25 m s^{-1} . The total size of the trajectory files is approximately 158 MB. The trajectories are stored in the following files:

- drag_mode_awes_opt_trajectories.pkl: Drag-mode AWES.
- 950 - lift_mode_awes_opt_trajectories.pkl: Lift-mode AWES with original reel-out strategy.
- lift_mode_awes_ind_trajectories.pkl: Lift-mode AWES with induction-based reel-out strategy.

The states, controls and other quantities can be visualized over a periodic cycle, as shown for lift-mode AWE systems in Figures B1 and B2 and for drag-mode AWE systems in Figures B3 and B4, using the Python script:

- visualize_reference_trajectories.py

955 The instantaneous in-flight values of states, controls and additional metrics are monitored and can be compared to their reference values in order to investigate in details the tracking behaviour of each individual AWE system. The available data covers one hour of operation of the fully developed AWES farms ($t \in [900\text{s}, 4500\text{s}]$). For the 25 AWE systems operating in each farm, the monitored flight data is stored as individual pickle object referenced from 001 to 025, according to the position

of the system in the farm. The total size of the flight data files is approximately 8.5 GB (3 parks \times 25 AWES \times \approx 113 MB). The
960 virtual flight data is stored in the following files (Set XXX to the index of the system):

- `lift_mode_farm_layout1_awes_XXX.pkl`: Lift-mode AWES park L1.
- `drag_mode_farm_layout1_awes_XXX.pkl`: Drag-mode AWES park D1.
- `drag_mode_farm_layout2_awes_XXX.pkl`: Drag-mode AWES park D2.

The record of tracked references is also organized as Python dictionary and is stored as pickle object for the three park
965 configurations of the study. The size of the tracking record files is about 1.4 MB and the files are stored as:

- `lift_mode_farm_layout1_tracking_scheme.pkl`: Lift-mode AWES park L1.
- `drag_mode_farm_layout1_tracking_scheme.pkl`: Drag-mode AWES park D1.
- `drag_mode_farm_layout2_tracking_scheme.pkl`: Drag-mode AWES park D2.

Each monitored quantity can be compared to its reference for a given time horizon, as shown for lift-mode AWE systems in
970 Figures B5 and B6 and for drag-mode AWE systems in Figures B7 and B8, using the Python script:

- `visualize_virtual_flight_data.py`

Author contributions. TH and JM jointly set up the concept and objectives of the current work, partially based on a research collaboration
plan previously devised by JM and MD. The PhD work of TH was supervised by JM, the PhD work of JDS by MD. TH performed code
implementations in the LES code SP-Wind and carried out the AWES park simulations. TH generated the reference AWES trajectories
975 using the `awebox` toolbox with support from JDS. JDS implemented the NMPC capability in the `awebox` toolbox and assisted TH for the
coupling with SP-Wind. TH performed the data analysis and data visualization. TH wrote the manuscript with major contributions from JM.
JDS, JM and MD revised the manuscript.

Competing interests. The authors declare that they have no conflict of interest.

Acknowledgements. The authors acknowledge support from the European Union's Horizon 2020 research and innovation programme under
980 the Marie Skłodowska-Curie grant agreements No 642682 and No 953348, and from DFG via the Projects No 277012063 and No 424107692.
The computational resources and services in this work were provided by the VSC (Flemish Supercomputer Center), funded by the Research
Foundation Flanders (FWO) and the Flemish Government department EWI.

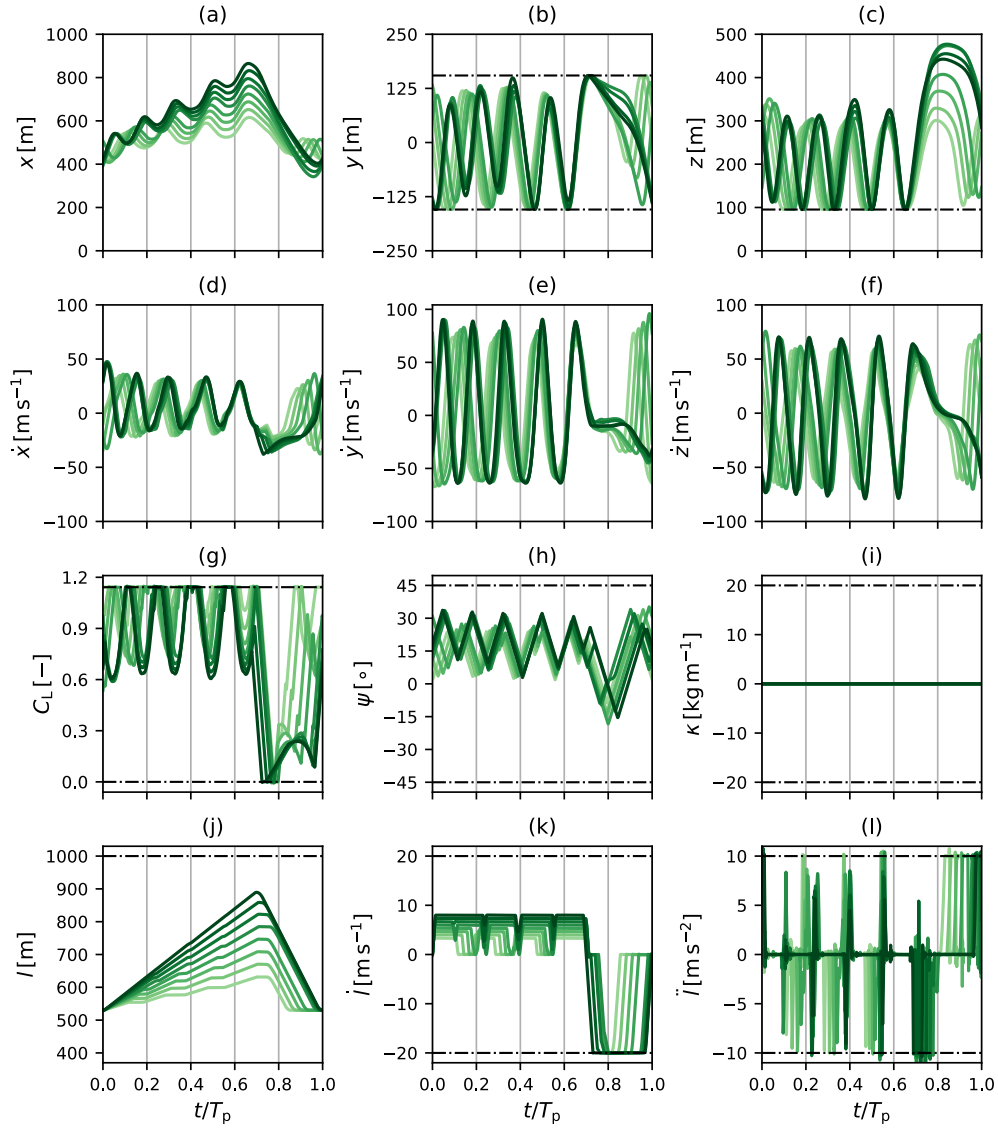


Figure B1. Time series of the states normalized over one period T_p for large-scale lift-mode AWE system (2) optimized for the wind speed range $U_D = [5.0, 12.0]$. The position \mathbf{q} and velocity $\dot{\mathbf{q}}$ are respectively shown in the sub-figures (a–) and (d–f). The wing lift coefficient C_L , roll angle Ψ and on-board turbine thrust coefficient κ are shown in the sub-figures (g–i). The tether variables l , \dot{l} and \ddot{l} , representing the length, speed and acceleration of the tether are shown in the sub-figures (j–l). The color scheme is identical to Fig. 3 and the black dashed lines represent the eventual constraints applied to the variables in POCP (33).

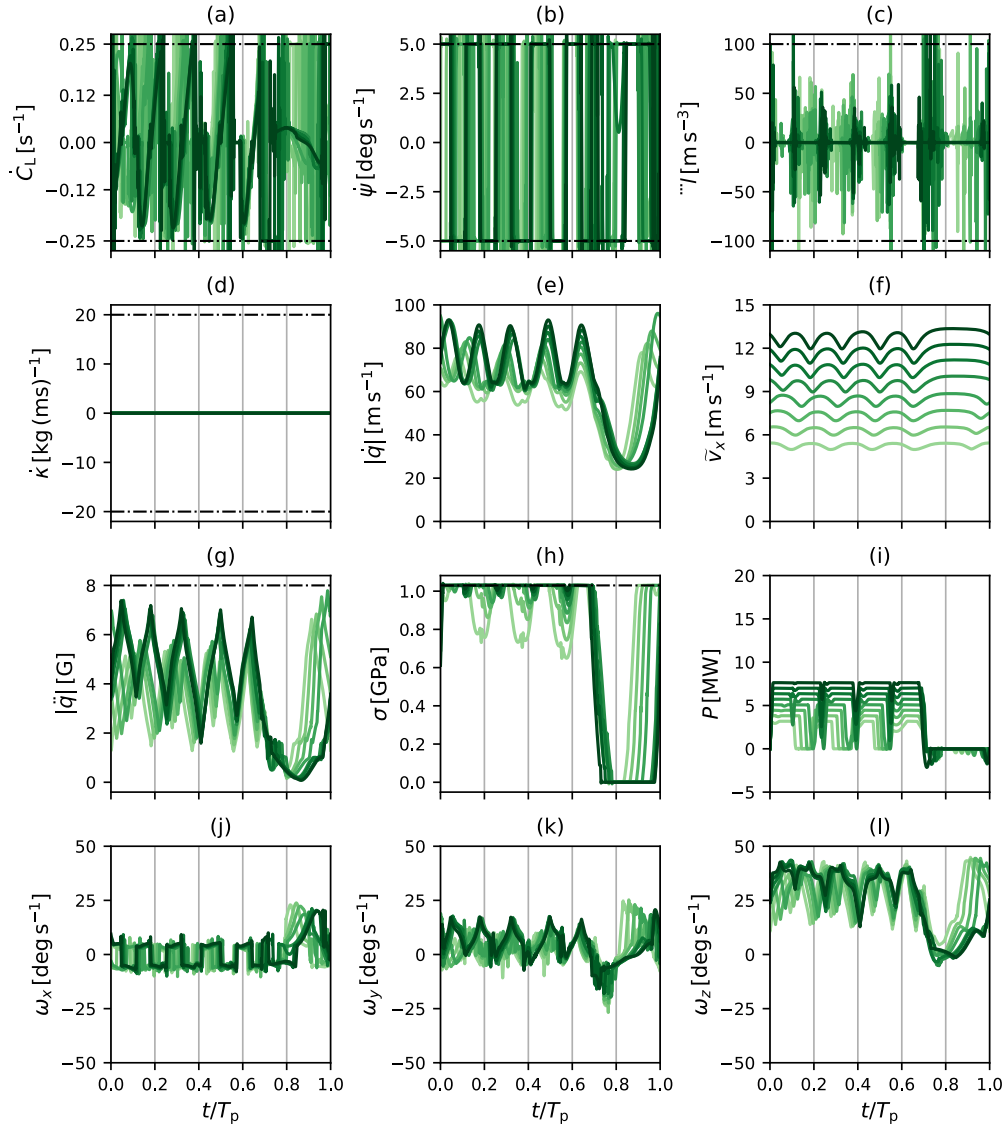


Figure B2. Time series of the controls and additional quantities normalized over one period T_p for large-scale lift-mode AWE system (2) optimized for the wind speed range $U_D = [5.0, 12.0]$. The control variables, ie. the time derivatives of lift coefficient \dot{C}_L , roll angle $\dot{\psi}$ and thrust coefficient κ , and the tether jerk $\ddot{\kappa}$ are shown in sub-figures (a–d). The magnitude of the flight speed $|\dot{q}|$ and the streamwise wind speed U_x are shown in sub-figures (e) and (f). The magnitude of acceleration $|\ddot{q}|$, the tether stress σ and the instantaneous power P are respectively shown in sub-figures (h–i). The components of the angular velocity ω are shown in sub-figures (j–l). The color scheme is identical to Fig. 3 and the black dashed lines represent the eventual constraints applied to the variables in POCP (33).

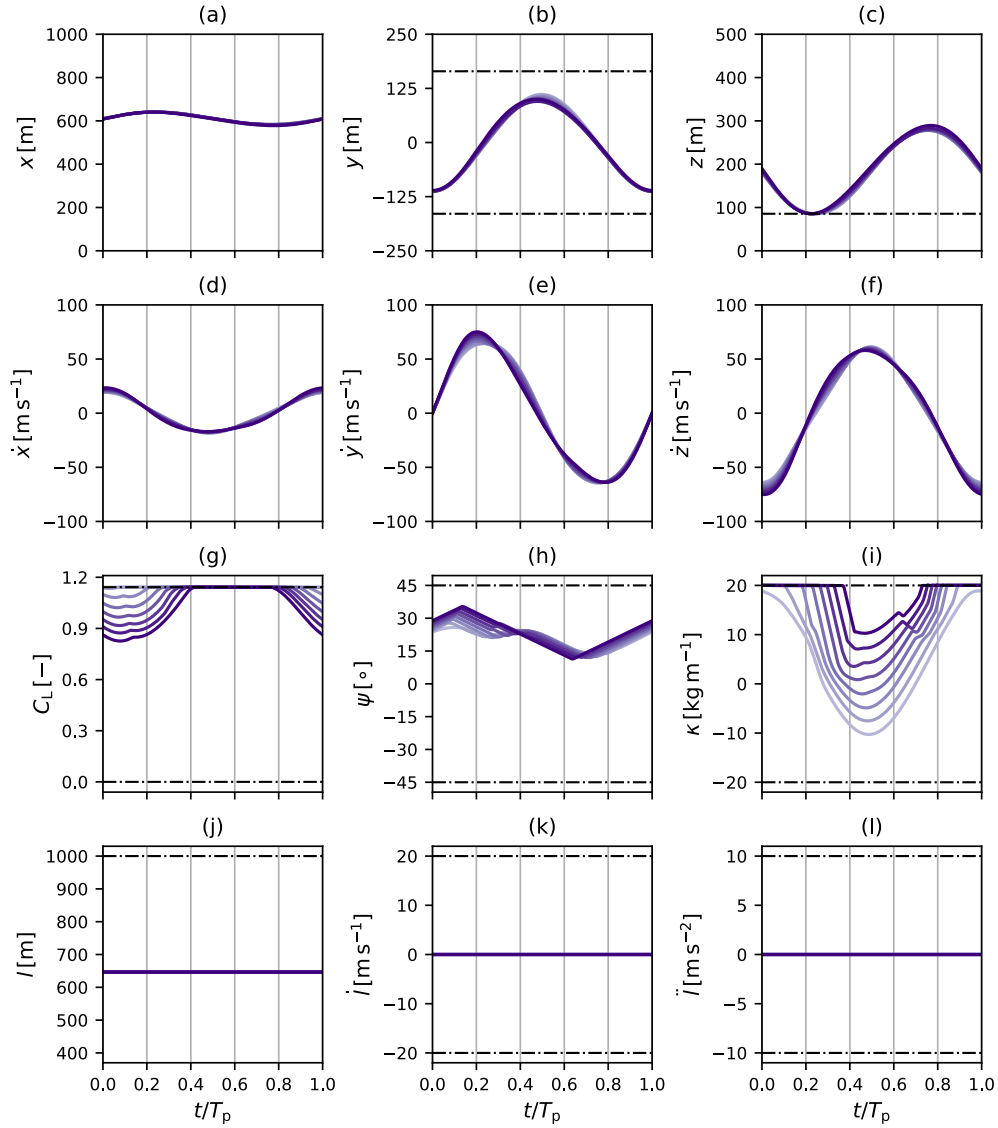


Figure B3. Time series of the states normalized over one period T_p for large-scale drag-mode AWE system optimized for the wind speed range $U_D = [5.0, 12.0]$. The position \mathbf{q} and velocity $\dot{\mathbf{q}}$ are respectively shown in the sub-figures (a–c) and (d–f). The wing lift coefficient C_L , roll angle Ψ and on-board turbine thrust coefficient κ are shown in the sub-figures (g–i). The tether variables l , \dot{l} and \ddot{l} , representing the length, speed and acceleration of the tether are shown in the sub-figures (j–l). The color scheme is identical to Fig. 3 and the black dashed lines represent the eventual constraints applied to the variables in POCP (33).

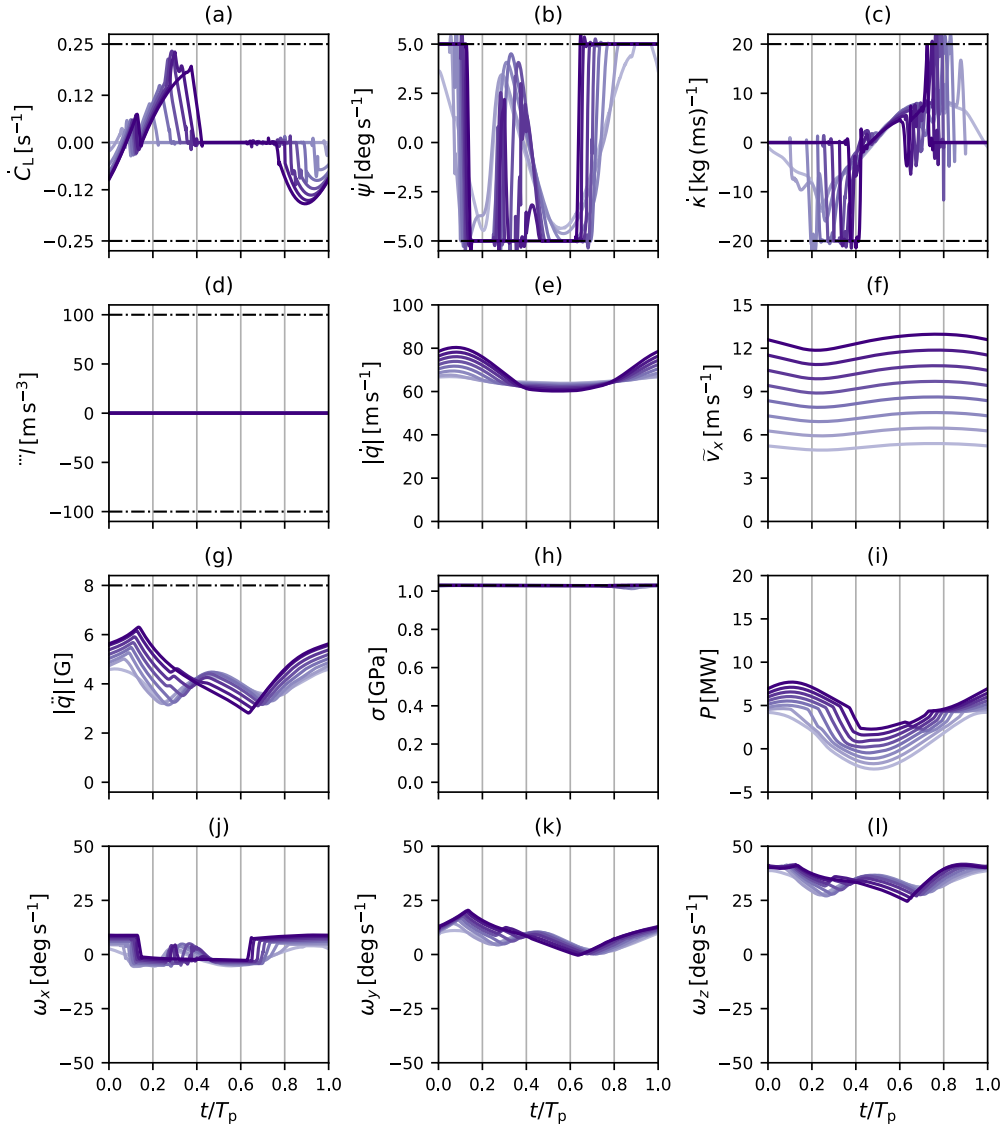


Figure B4. Time series of the controls and additional quantities normalized over one period T_p for large-scale drag-mode AWE system optimized for the wind speed range $U_D = [5.0, 12.0]$. The control variables, ie. the time derivatives of lift coefficient \dot{C}_L , roll angle $\dot{\Psi}$ and thrust coefficient κ , and the tether jerk \ddot{l} are shown in sub-figures (a–d). The magnitude of the flight speed $|\dot{q}|$ and the streamwise wind speed U_x are shown in sub-figures (e) and (f). The magnitude of acceleration $|\ddot{q}|$, the tether stress σ and the instantaneous power P are respectively shown in sub-figures (h–i). The components of the angular velocity ω are shown in sub-figures (j–l). The color scheme is identical to Fig. 3 and the black dashed lines represent the eventual constraints applied to the variables in POCP (33).

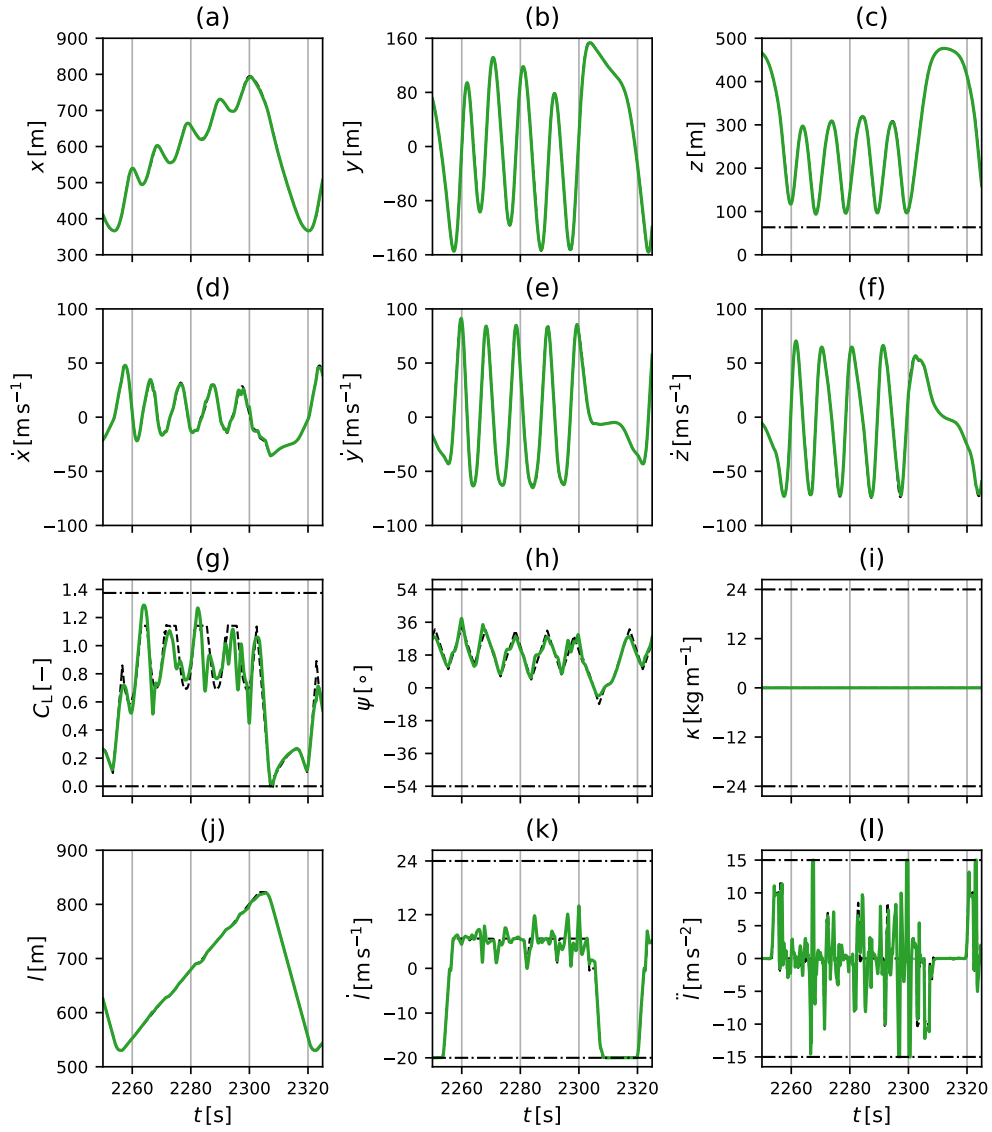


Figure B5. Instantaneous states measured at the point-mass of the lift-mode AWE system 003 (park L1) compared to their reference values. The position \mathbf{q} and velocity $\dot{\mathbf{q}}$ are respectively shown in the sub-figures (a–c) and (d–f). The wing lift coefficient C_L , roll angle Ψ and on-board turbine thrust coefficient κ are shown in the sub-figures (g–i). The tether variables l , \dot{l} and \ddot{l} , representing the length, speed and acceleration of the tether are shown in the sub-figures (j–l). The black dashed and dash-dotted lines respectively represent the variable references and the eventual constraints applied to the variables in NMPC (36).

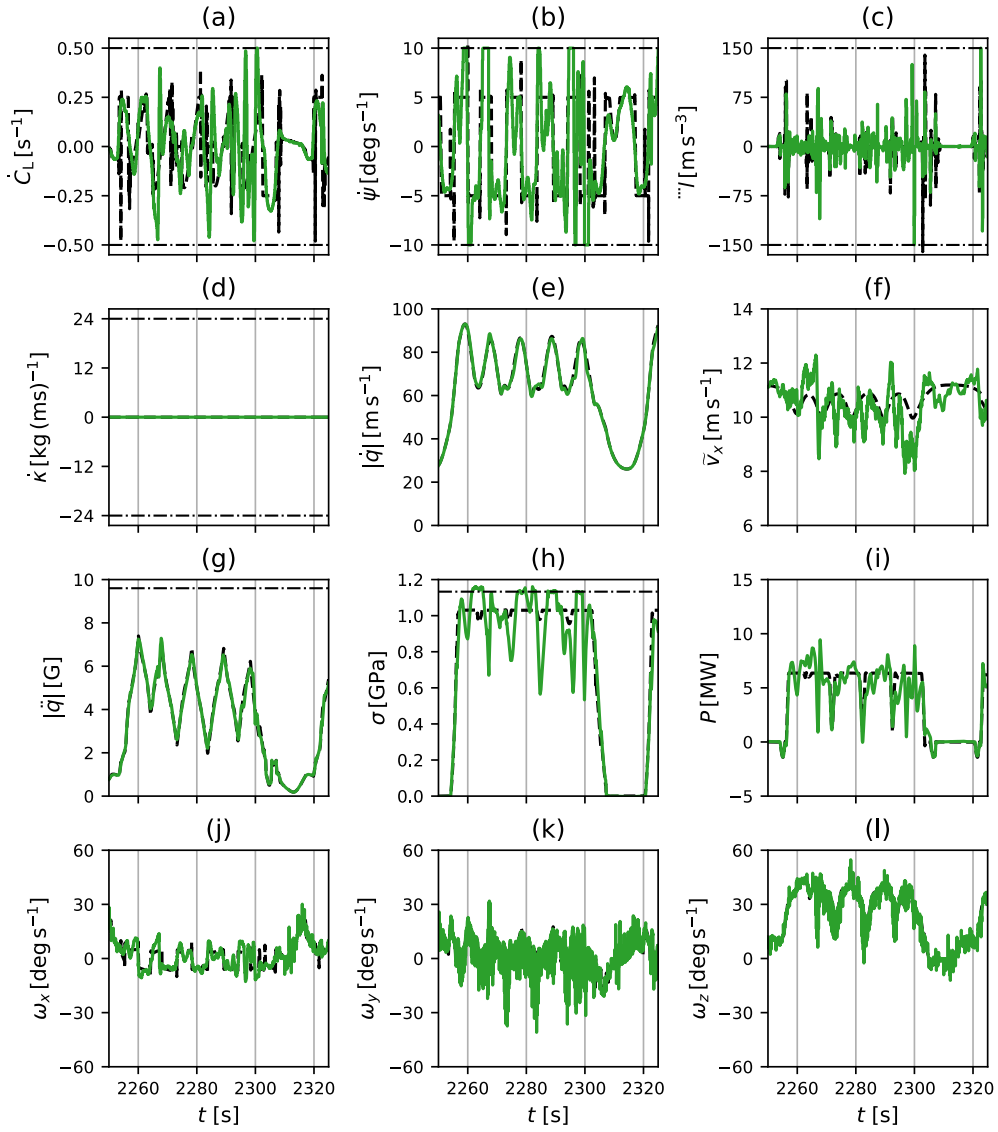


Figure B6. Instantaneous controls and additional quantities measured at the point-mass of the lift-mode AWE system 003 (park L1) compared to their reference values. The control variables, ie. the time derivatives of lift coefficient \dot{C}_L , roll angle $\dot{\Psi}$ and thrust coefficient $\dot{\kappa}$, and the tether jerk \ddot{l} are shown in sub-figures (a–d). The magnitude of the flight speed $|\dot{q}|$ and the streamwise wind speed \tilde{v}_x are shown in sub-figures (e) and (f). The magnitude of acceleration $|\ddot{q}|$, the tether stress σ and the instantaneous power P are respectively shown in sub-figures (h–i). The components of the angular velocity ω are shown in sub-figures (j–l). The black dashed and dash-dotted lines respectively represent the variable references and the eventual constraints applied to the variables in NMPC (36).

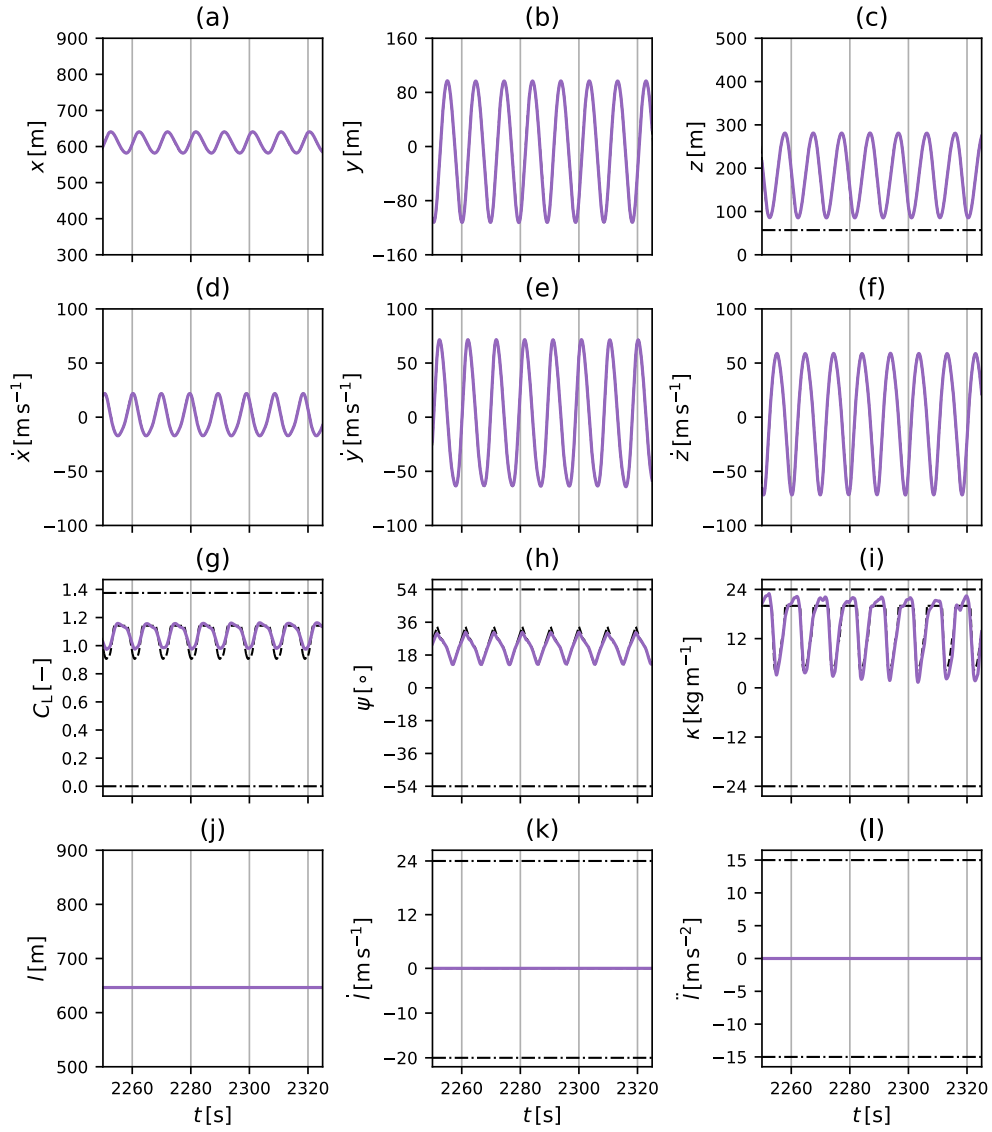


Figure B7. Instantaneous states measured at the point-mass of the drag-mode AWE system 003 (park D1) compared to their reference values. The position \mathbf{q} and velocity $\dot{\mathbf{q}}$ are respectively shown in the sub-figures (a-c) and (d-f). The wing lift coefficient C_L , roll angle Ψ and on-board turbine thrust coefficient κ are shown in the sub-figures (g-i). The tether variables l , \dot{l} and \ddot{l} , representing the length, speed and acceleration of the tether are shown in the sub-figures (j-l). The black dashed and dash-dotted lines respectively represent the variable references and the eventual constraints applied to the variables in NMPC (36).

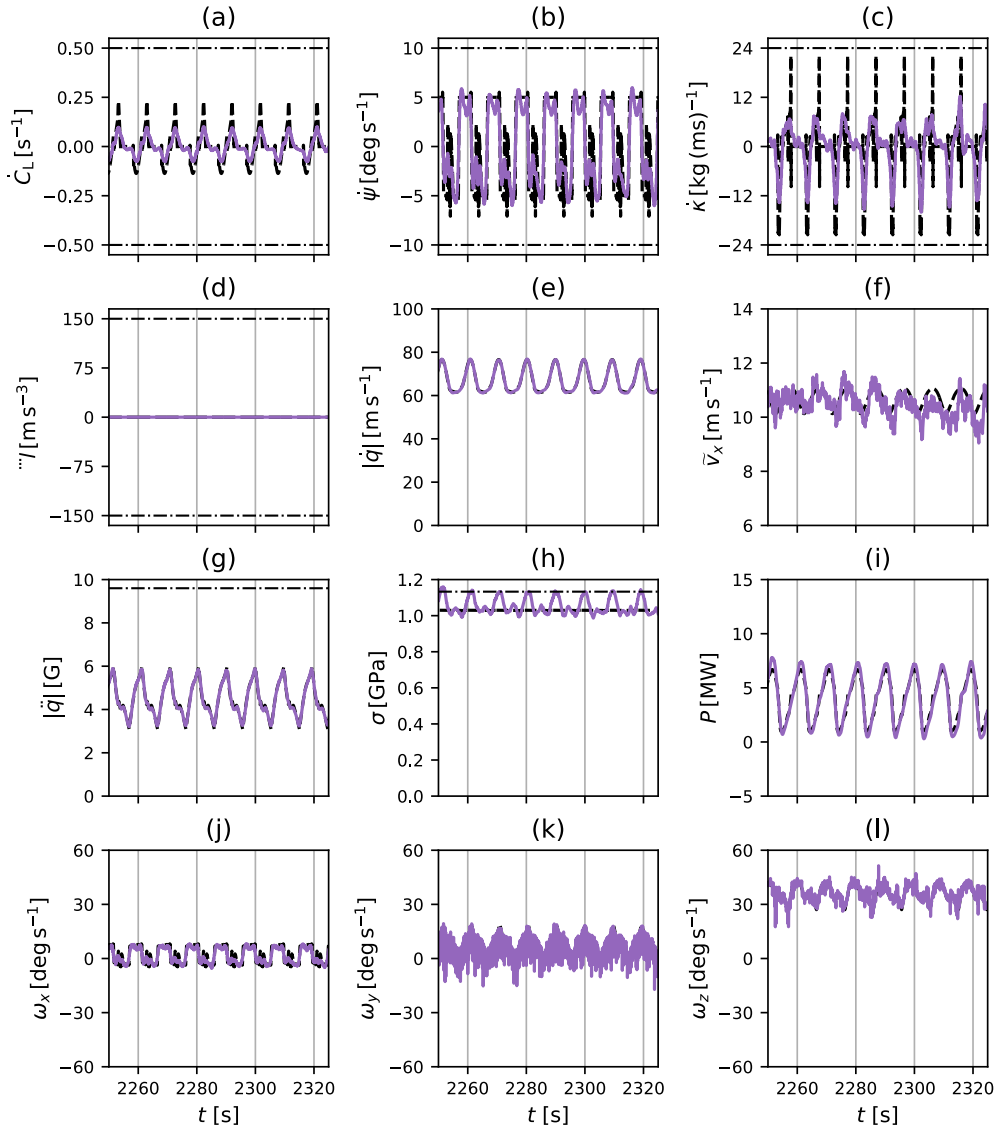


Figure B8. Instantaneous controls and additional quantities measured at the point-mass of the drag-mode AWE system 003 (park D1) compared to their reference values. The control variables, ie. the time derivatives of lift coefficient \dot{C}_L , roll angle $\dot{\Psi}$ and thrust coefficient $\dot{\kappa}$, and the tether jerk $\ddot{\tau}$ are shown in sub-figures (a–d). The magnitude of the flight speed $|\dot{q}|$ and the streamwise wind speed \tilde{v}_x are shown in sub-figures (e) and (f). The magnitude of acceleration $|\ddot{q}|$, the tether stress σ and the instantaneous power P are respectively shown in sub-figures (h–i). The components of the angular velocity ω are shown in sub-figures (j–l). The black dashed and dash-dotted lines respectively represent the variable references and the eventual constraints applied to the variables in NMPC (36).

References

- Alemi Ardakani, H. and Bridges, T. J.: Review of the 3-2-1 Euler Angles: a yaw–pitch–roll sequence, Tech. rep., 2010.
- 985 Allaerts, D. and Meyers, J.: Large eddy simulation of a large wind-turbine array in a conventionally neutral atmospheric boundary layer, *Physics of Fluids*, 27, <https://doi.org/10.1063/1.4922339>, 2015.
- Allaerts, D. and Meyers, J.: Boundary-layer development and gravity waves in conventionally neutral wind farms, *Journal of Fluid Mechanics*, 814, 95–130, 2017.
- Anderson, J. D.: *Fundamentals of Aerodynamics*, McGraw-Hill, 2010.
- 990 Andersson, J. A. E., Gillis, J., Horn, G., B, J., Rawlings, and Diehl, M.: CasADi: a software framework for nonlinear optimization and optimal control, *Mathematical Programming Computation*, 2018.
- Archer, C. L.: An Introduction to Meteorology for Airborne Wind Energy, in: *Airborne Wind Energy*, edited by Ahrens, U., Diehl, M., and Schmehl, R., pp. 81–94, Springer-Verlag Berlin Heidelberg, 2013.
- Argatov, I. and Silvennoinen, R.: Efficiency of Traction Power Conversion Based on Crosswind Motion, in: *Airborne Wind Energy*, edited
995 by Ahrens, U., Diehl, M., and Schmehl, R., pp. 65–79, Springer-Verlag Berlin Heidelberg, https://doi.org/10.1007/978-3-642-39965-7_4, 2013.
- awebox: awebox: Modelling and optimal control of single- and multiple-kite systems for airborne wind energy., <https://github.com/awebox>, 2021.
- Barthelmie, R. J., Pryor, S. C., Frandsen, S. T., Hansen, K. S., Schepers, J. G., Rados, K., Schlez, W., Neubert, A., Jensen, L. E., and
1000 Neckelmann, S.: Quantifying the Impact of Wind Turbine Wakes on Power Output at Offshore Wind Farms, *Journal of Atmospheric and Oceanic Technology*, 27, 1302 – 1317, <https://doi.org/10.1175/2010JTECHA1398.1>, 2010.
- Bauer, F., Kennel, R. M., Hackl, C. M., Campagnolo, F., Patt, M., and Schmehl, R.: Drag power kite with very high lift coefficient, *Renewable Energy*, 118, 290–305, <https://doi.org/10.1016/j.renene.2017.10.073>, 2018.
- Bulder, B., Bedon, G., and Bot, E.: Optimal wind farm power density analysis for future offshore wind farms, Tech. rep., 2018.
- 1005 Calaf, M., Meneveau, C., and Meyers, J.: Large eddy simulation study of fully developed wind-turbine array boundary layers, *Physics of Fluids*, 22, 1–16, <https://doi.org/10.1063/1.862466>, 2010.
- Cherubini, A., Papini, A., Vertechy, R., and Fontana, M.: Airborne Wind Energy Systems: A review of the technologies, *Renewable and Sustainable Energy Reviews*, 51, 1461 – 1476, <https://doi.org/https://doi.org/10.1016/j.rser.2015.07.053>, 2015.
- De Lellis, M., Reginatto, R., Saraiva, R., and Trofino, A.: The Betz limit applied to Airborne Wind Energy, *Renewable Energy*, 127, 32 – 40,
1010 <https://doi.org/https://doi.org/10.1016/j.renene.2018.04.034>, 2018.
- De Schutter, J., Bronnenmeyer, T., Paelinck, R., Diehl, M., and Leuthold, R.: Optimal control of stacked multi-kite systems for utility-scale airborne wind energy, <https://doi.org/10.1109/CDC40024.2019.9030026>, 2019.
- Diehl, M.: Airborne wind energy: Basic concepts and physical foundations, in: *Airborne Wind Energy*, edited by Ahrens, U., Diehl, M., and Schmehl, R., pp. 3–22, Springer-Verlag Berlin Heidelberg, 2013.
- 1015 Dykes, K.: Optimization of Wind Farm Design for Objectives Beyond LCOE, vol. 1618, IOP Publishing, <https://doi.org/10.1088/1742-6596/1618/4/042039>, 2020.
- Echeverri, P., Fricke, T., Homsy, G., and Tucker, N.: The Energy Kite: Selected Results from the Design, Development, and Testing of Makani’s Airborne Wind Turbines, Part I of III, Tech. rep., 2020.

- 1020 Gaunaa, M., Forsting, A. M., and Trevisi, F.: An engineering model for the induction of crosswind kite power systems, *Journal of Physics: Conference Series*, 1618, 032 010, <https://doi.org/10.1088/1742-6596/1618/3/032010>, 2020.
- Gohl, F. and Luchsinger, R. H.: Simulation Based Wing Design for Kite Power, in: *Airborne Wind Energy*, edited by Ahrens, U., Diehl, M., and Schmehl, R., pp. 325–338, Springer-Verlag Berlin Heidelberg, 2013.
- Gros, S. and Diehl, M.: Modeling of airborne wind energy systems in natural coordinates, in: *Airborne Wind Energy*, edited by Ahrens, U., Diehl, M., and Schmehl, R., pp. 181–203, Springer-Verlag Berlin Heidelberg, 2013.
- 1025 Gros, S. and Zanon, M.: Numerical Optimal Control With Periodicity Constraints in the Presence of Invariants, *IEEE Transactions on Automatic Control*, PP, 1–1, <https://doi.org/10.1109/TAC.2017.2772039>, 2017.
- Gros, S., Zanon, M., and Diehl, M.: Control of Airborne Wind Energy systems based on Nonlinear Model Predictive Control and Moving Horizon Estimation, in: *2013 European Control Conference (ECC)*, pp. 1017–1022, <https://doi.org/10.23919/ECC.2013.6669713>, 2013.
- Haas, T. and Meyers, J.: Comparison study between wind turbine and power kite wakes, *Journal of Physics: Conference Series*, 854, 012 019, 1030 <https://doi.org/10.1088/1742-6596/854/1/012019>, 2017.
- Haas, T. and Meyers, J.: AWESCO Wind Field Datasets, <https://doi.org/10.5281/zenodo.1418676>, 2019.
- Haas, T. and Meyers, J.: Large-eddy simulation of airborne wind energy farms: AWES virtual flight data, <https://doi.org/10.5281/zenodo.5705563>, 2021.
- Haas, T., De Schutter, J., Diehl, M., and Meyers, J.: Wake characteristics of pumping mode airborne wind energy systems, *Journal of Physics: Conference Series*, 1256, 012 016, <https://doi.org/10.1088/1742-6596/1256/1/012016>, 2019b.
- 1035 Harham, C.: Response to the federal aviation authority, Tech. rep., Makani Power, <http://www.energykitesystems.net/FAA/FAAfromMakani.pdf>, 2012.
- Horn, G., Gros, S., and Diehl, M.: Numerical trajectory optimization for airborne wind energy systems described by high fidelity aircraft models, in: *Airborne Wind Energy*, edited by Ahrens, U., Diehl, M., and Schmehl, R., pp. 205–218, Springer-Verlag Berlin Heidelberg, 1040 2013.
- Houska, B.: Robustness and Stability Optimization of Open-Loop Controlled Power Generating Kites, Ph.D. thesis, Ruprecht-Karls-Universität Heidelberg, 2007.
- HSL: A collection of Fortran codes for large scale scientific computation., <http://www.hsl.rl.ac.uk>, <http://www.hsl.rl.ac.uk>, 2011.
- Jenkins, N., Burton, A., Sharpe, D., and Bossanyi, E.: *Wind Energy Handbook*, Wiley, 2001.
- 1045 Jeong, J. and Hussain, F.: On the identification of a vortex, *Journal of Fluid Mechanics*, 285, 69 – 94, <https://doi.org/10.1017/S0022112095000462>, 1995.
- Jimenez, A., Crespo, A., Migoya, E., and Garcia, J.: Advances in large-eddy simulation of a wind turbine wake, *Journal of Physics: Conference Series*, 75, 012 041, 2007.
- Kaufman-Martin, S., Naclerio, N., May, P., and Luzzatto-Fegiz, P.: An entrainment-based model for annular wakes, with applications to 1050 airborne wind energy, *Wind Energy*, <https://doi.org/https://doi.org/10.1002/we.2679>, 2021.
- Kheiri, M., Bourgault, F., Saberi Nasrabad, V., and Victor, S.: On the aerodynamic performance of crosswind kite power systems, *Journal of Wind Engineering and Industrial Aerodynamics*, 181, 1 – 13, <https://doi.org/https://doi.org/10.1016/j.jweia.2018.08.006>, 2018.
- Kruijff, M. and Ruitkamp, R.: A Roadmap Towards Airborne Wind Energy in the Utility Sector, in: *Airborne Wind Energy: Advances in Technology Development and Research*, edited by Schmehl, R., pp. 643–662, Springer Singapore, 2018.
- 1055 Leuthold, R., Gros, S., and Diehl, M.: Induction in Optimal Control of Multiple-Kite Airborne Wind Energy Systems, in: *Proceedings of 20th IFAC World Congress*, Toulouse, France, 2017.

- Leuthold, R., De Schutter, J., Malz, E., Licitra, G., Gros, S., and Diehl, M.: Operational Regions of a Multi-Kite AWE System, pp. 52–57, <https://doi.org/10.23919/ECC.2018.8550199>, 2018.
- 1060 Leuthold, R., Crawford, C., Gros, S., and Diehl, M.: Engineering Wake Induction Model For Axisymmetric Multi-Kite Systems, *Journal of Physics: Conference Series*, 1256, 012 009, <https://doi.org/10.1088/1742-6596/1256/1/012009>, 2019.
- Licitra, G., Sieberling, S., Engelen, S., Williams, P., Ruiterkamp, R., and Diehl, M.: Optimal control for minimizing power consumption during holding patterns for airborne wind energy pumping system, pp. 1574–1579, <https://doi.org/10.1109/ECC.2016.7810515>, 2016.
- Licitra, G., Williams, P., Gillis, J., Ghandchi, S., Sieberling, S., Ruiterkamp, R., and Diehl, M.: Aerodynamic Parameter Identification for an Airborne Wind Energy Pumping System, *IFAC-PapersOnLine*, 50, 11 951 – 11 958, <https://doi.org/https://doi.org/10.1016/j.ifacol.2017.08.1038>, 20th IFAC World Congress, 2017.
- 1065 Licitra, G., Koenemann, J., Bürger, A., Williams, P., Ruiterkamp, R., and Diehl, M.: Performance assessment of a rigid wing Airborne Wind Energy pumping system, *Energy*, 173, 569 – 585, <https://doi.org/https://doi.org/10.1016/j.energy.2019.02.064>, 2019.
- Loyd, M. L.: Crosswind Kite Power, *Journal of Energy*, 4, 106–111, <https://doi.org/10.2514/3.48021>, 1980.
- Malz, E., Zanon, M., and Gros, S.: A Quantification of the Performance Loss of Power Averaging in Airborne Wind Energy Farms, <https://doi.org/10.23919/ECC.2018.8550357>, 2018.
- 1070 Malz, E., Koenemann, J., Sieberling, S., and Gros, S.: A reference model for airborne wind energy systems for optimization and control, *Renewable Energy*, 140, 1004 – 1011, <https://doi.org/https://doi.org/10.1016/j.renene.2019.03.111>, 2019.
- Martinez-Tossas, L. A., Churchfield, M. J., Yilmaz, A. E., Sarlak, H., Johnson, P. L., Sorensen, J. N., Meyers, J., and Meneveau, C.: Comparison of four large-eddy simulation research codes and effects of model coefficient and inflow turbulence in actuator-line-based wind turbine modeling, *Journal Of Renewable And Sustainable Energy*, 10, 2018.
- 1075 Mason, P. J. and Thomson, D. J.: Stochastic backscatter in large-eddy simulations of boundary layers, *Journal of Fluid Mechanics*, 242, 51–78, <https://doi.org/10.1017/S0022112092002271>, 1992.
- Munters, W., Meneveau, C., and Meyers, J.: Turbulent Inflow Precursor Method with Time-Varying Direction for Large-Eddy Simulations and Applications to Wind Farms, *Boundary-Layer Meteorology*, 159, 305–328, <https://doi.org/10.1007/s10546-016-0127-z>, 2016.
- 1080 Pope, S. B.: *Turbulent Flows*, Cambridge University Press, <https://doi.org/10.1017/CBO9780511840531>, 2000.
- Porte-Agel, F., Bastankhah, M., and Shamsoddin, S.: Wind-turbine and wind-farm flows : a review., *Boundary-layer meteorology.*, 174, 1–59, <http://dro.dur.ac.uk/29141/>, 2020.
- Rapp, S., Schmehl, R., Oland, E., and Haas, T.: Cascaded Pumping Cycle Control for Rigid Wing Airborne Wind Energy Systems, *Journal of Guidance, Control, and Dynamics*, 42, 2456–2473, <https://doi.org/10.2514/1.G004246>, 2019.
- 1085 Read, R.: Kite Networks for Harvesting Wind Energy, in: *Airborne Wind Energy: Advances in Technology Development and Research*, edited by Schmehl, R., pp. 515–517, Springer Singapore, 2018.
- Roque, L. A., Paiva, L. T., Fernandes, M. C., Fontes, D. B., and Fontes, F. A.: Layout optimization of an airborne wind energy farm for maximum power generation, *Energy Reports*, 6, 165–171, <https://doi.org/https://doi.org/10.1016/j.egyr.2019.08.037>, the 6th International Conference on Energy and Environment Research - Energy and environment: challenges towards circular economy, 2020.
- 1090 Schelbergen, M. and Schmehl, R.: Validation of the quasi-steady performance model for pumping airborne wind energy systems, *Journal of Physics Conference Series*, 1618, 32 003, <https://doi.org/10.1088/1742-6596/1618/3/032003>, 2020.
- Sorensen, J. N. and Shen, W. Z.: Numerical Modeling of Wind Turbine Wakes, *Journal of Fluids Engineering*, 124, 393, <https://doi.org/10.1115/1.1471361>, 2002.

- 1095 Sternberg, J., Goit, J., Gros, S., Meyers, J., and Diehl, M.: Robust and stable periodic flight of power generating kite systems in a turbulent wind flow field, *IFAC Proceedings Volumes (IFAC-PapersOnline)*, 45, 140–145, <https://doi.org/10.3182/20120913-4-IT-4027.00009>, 2012.
- Stevens, R. J. and Meneveau, C.: Flow Structure and Turbulence in Wind Farms, *Annual Review of Fluid Mechanics*, 49, 311–339, <https://doi.org/10.1146/annurev-fluid-010816-060206>, 2017.
- 1100 Storey, R. C., Norris, S. E., and Cater, J. E.: An actuator sector method for efficient transient wind turbine simulation, *Wind Energy*, 18, 699–711, <https://doi.org/10.1002/we.1722>, 2015.
- Trevisi, F., Gaunaa, M., and McWilliam, M.: The Influence of Tether Sag on Airborne Wind Energy Generation, *Journal of Physics: Conference Series*, 1618, 032 006, <https://doi.org/10.1088/1742-6596/1618/3/032006>, 2020.
- Troen, I. and Lundtang Petersen, E.: *European Wind Atlas*, Tech. rep., 1989.
- Troldborg, N., Sorensen, J. N., and Mikkelsen, R.: Numerical simulations of wake characteristics of a wind turbine in uniform inflow, *Wind Energy*, 13, 86–99, <https://doi.org/10.1002/we.345>, 2010.
- 1105 Vitsas, A. and Meyers, J.: Multiscale aeroelastic simulations of large wind farms in the atmospheric boundary layer, *Journal of Physics: Conference Series*, 753, <https://doi.org/10.1088/1742-6596/753/8/082020>, 2016.
- Wächter, A.: *An Interior Point Algorithm for Large-Scale Nonlinear Optimization with Applications in Process Engineering*, Ph.D. thesis, Carnegie Mellon University, 2002.
- 1110 XFLR5: XFLR5: XFLR5 is an analysis tool for airfoils, wings and planes, <https://sourceforge.net/projects/xflr5/>, 2021.
- XFOIL: XFOIL: Subsonic Airfoil Development System, <https://web.mit.edu/drela/Public/web/xfoil/>, 2021.
- Zanon, M.: *Efficient Nonlinear Model Predictive Control Formulations for Economic Objectives with Aerospace and Automotive Applications*, 2015.
- Zanon, M., Gros, S., Andersson, J., and Diehl, M.: Airborne Wind Energy Based on Dual Airfoils, *Control Systems Technology*, *IEEE Transactions on*, 21, 1215–1222, <https://doi.org/10.1109/TCST.2013.2257781>, 2013a.
- 1115 Zanon, M., Gros, S., and Diehl, M.: Model predictive control of rigid-airfoil airborne wind energy systems, in: *Airborne Wind Energy*, edited by Ahrens, U., Diehl, M., and Schmehl, R., pp. 219–234, Springer-Verlag Berlin Heidelberg, 2013b.